Master's thesis in physical oceanography

Permeability of young sea ice from microtomographic images

Author:
Juliane Büttner

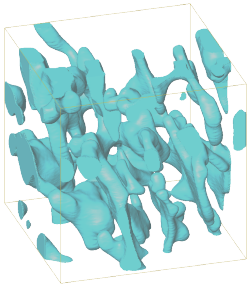

Supervisors:
Sönke Maus
Peter Haugan
Mats Granskog

Tromsø, February 2011

Geophysical Institute
University in Bergen


UNIVERSITAS
BERGENSIS


NORSK·POLARINSTITUTT

Abstract

The permeability of sea ice controls the transport of substances through the ice and thereby its surface properties as well as the exchange of heat, salt and gas between ice, ocean and atmosphere. More observations and understanding are necessary to properly implement the impact of permeability on sea ice melt and growth in models.
This study employs and evaluates a microscopical approach to determine permeability. We combine structure-preserving field sampling with non-destructive synchrotron-based microtomography (SXRT) and lattice Boltzmann modelling (LBM) of fluid flow.
Samples of young sea ice from Kongsfjorden, Svalbard, were centrifuged at their respective *in situ* temperatures before SXRT was performed at temperatures below -40°C, resulting in 3-dimensional images 1.2x1.2x1.7cm^3 in size with a resolution of 11.84μm. From these images microstructural characteristics of sea ice were derived and fluid flow through the samples was modelled with LBM at 22 and 35μm resolution to obtain directional values of permeability for all three directions.
Our method is limited to small sample sizes due to constraints with respect to computer memory and imaging. Therefore it might not be appropriate for all types of ice. With increasing computer memory and parallelization the applicability of this method will increase. Its major advantage over conventional permeability measurements is that it produces a 3-dimensional representation of the pore space which allows for the derivation of microstructural quantities and for modelling processes such as fluid flow or radiative transfer.
Quantities derived from the microstructure were different porosities, a critical length scale, minor and major ellipse axis lengths, pore volume to surface ratio, two-point correlation length, pore radius and area distributions as well as measures of hydraulic and electrical tortuosity. Their intercorrelations and porosity dependence varied with ice type.
Our data suggested a percolation transition at a porosity of about 7% for columnar ice both vertically and horizontally parallel to the plates. Permeability of columnar ice exhibited a horizontal anisotropy of 0.21 between flow parallel and perpendicular to the columns. No difference was found between horizontal flow parallel to the plates and vertical flow. This finding is relevant for field techniques of measuring sea ice permeability that strongly depend on the anisotropy factor. Furthermore, correlations between the permeability of columnar ice and porosities as well as several length scales indicated a strong dependence on effective porosity (the connected pore space) and the length scales describing pore necks and the smallest dimension of the pores. Power law regressions on porosities and length scales predicted permeability more accurately than common models derived from studies of sandstone permeability.

Sammendrag

Havisens permeabilitet kontrollerer transporten av stoffer gjennom isen og dermed dens overflateegenskaper samt utveksling av varme, salt og gass mellom is, hav og atmosfære. Flere observasjoner og mer kunnskap er nødvendig for å integrere permeabilitetens effekt på isvekst og smelting i modeller.
Denne studien anvender og evaluerer en mikroskopisk tilnærming for å bestemme permeabilitet av havis. Vi kombinerer strukturbevarende prøvetaking med ikke-destruktiv synkrotron-basert røntgenmikrotomografi (SXRT) og gitter Boltzmann modellering (LBM) av væskestrømning.
Prøver av ung havis fra Kongsfjorden, Svalbard, ble sentrifugert ved sine *in situ* temperaturer før SXRT ble gjennomført ved temperaturer under -40°C, resulterende i 1.2x1.2x1.7cm^3 store 3D bilder med en oppløsning på 11.84μm. Disse bildene ble brukt til å finne mikrostrukturkarakteristikker og modellere væskestrømning gjennom prøvene med LBM på 22 og 35μm oppløsning for å beregne permeabiliteter i alle tre retninger.
Metoden vår er begrenset til små prøvestørrelser på grunn av begrensninger i dataminne og bildeteknikk og er derfor ikke like velegnet for alle istyper. Med økende dataminne og parallelisering vil bruksområdet til denne metoden vokse. Dens største fordel overfor konvesjonelle permeablitetsmålinger er at den produserer en 3D representasjon av porerommet i isen som tillater beregning av mikrostrukturmål og modellering av for eksempel væskestrøming eller strålingsoverføring.
Størrelser beregnet utifra miktrostrukturen var forskjellige porøsiteter, en kritisk lengdeskala, store og små akselengder av ellipser, forhold mellom porevolum og -overflate, to-punktskorrelasjonslengde, poreradius- og arealfordelinger så vel som mål av både hydraulisk og elektrisk tortuositet. Interkorrelasjonene og porøsitetsavhengigheten varierte med istype.
Våre data foreslår en perkolasjonsovergang ved ca. 7 % porøsitet for søyle-is (columnar) parallel til lagene. Permeabilitetene av søyle-is oppviste en horisontal anisotropi på 0.21 mellom strømning parallel og loddrett på lagene. Ingen anisotropi ble funnet mellom horisontal strømning parallel til lagene og vertikal strømning. Dette resultatet er relevant for feltmålinger av havispermeabilitet som er avhengige av anisotropifaktoren. Dessuten tyder undersøkelsen av korrelasjonen av permeabiliteten for søyle-is med porositetene og lengdeskalaene på en sterk avhengighet av effektiv porøsitet (forbundet porerom) og de lengdeskalaene som beskriver porehals og den korteste dimensjonen av porene. Regresjoner med potensfunksjoner av permeabilitet med porøsiteter og lengdeskalaer forutsa permeabiliteten bedre enn vanlige modeller fra studier av sandsteinpermeabiliteter.

Acknowledgements

A lot has happened since I got involved with this project two years ago and it has been a pleasure to learn about scientific work and its ups and downs.
I would like to express my gratitude to my supervisors Sönke Maus, who got me involved in this interesting project and always had time to discuss questions, and Peter Haugan and Mats Granskog, who gave valuable comments and support and made it possible for me to write this thesis for the University in Bergen at the Norwegian Polar Institute in Tromsø.
Field work was financed by the Arctic Field Grant from the Svalbard Science Forum and was carried out at the Marine Lab in Ny Ålesund. Thanks to Susann Müller, Eivind Høstmark Borge and Anssi Vähätalo for their field work assistance and to Thomas Huthwelker and everyone involved in the microtomography of the ice samples.
Without the support of Frieder Enzmann and the servers at Institute of Geosciences at the Johannes Gutenberg University in Mainz and the hospitality during my two visits to Mainz, this thesis could have never been what it is and I am deeply grateful for all the time and energy he invested in this project. The use of the software GeoDict was possible through an evaluation license and a cooperation between the Institute of Geosciences at the Johannes Gutenberg University in Mainz and the ITWM.
Also thanks to Sebastian Gerland and others at the Norwegian Polar Institute, who made my stay here instructive and enjoyable, the Studienstiftung des deutschen Volkes for a scholarship saving me from having to work, my sister Ulrike for comments on scientific writing and Eivind for proofreading.
I would like to thank my parents for their support throughout my studies and Eivind and Johanna for making coming home the best part of the day.

Contents

List of Figures

List of Tables

Nomenclature

Abbreviations

CI Confidence interval, page 41

2D two-dimensional, page 19

3D three-dimensional, page 5

LBM Lattice Boltzmann method, page 2

MIP Mercury intrusion porosimetry, page 9

MRI Magnetic resonance imaging, page 5

SXRT Synchrotron-based x-ray microtomography, page 18

TOMCAT Tomography beamline of the Swiss Light Source synchrotron, page 18

X-ray CT X-ray computed tomography, page 5

Greek

α Shape parameter in gamma distribution, *dimensionless*, page 32

β Shape constant, *dimensionless*, page 8

η Dynamic viscosity, Pas, page 3

μ Mean in lognormal distribution, *dimensionless*, page 32

ν Kinematic viscosity, m^2s^{-1}, page 37

ϕ Porosity, *dimensionless*, page 3

ϕ_{eff} Effective porosity, *dimensionless*, page 30

ϕ_{im} Imaged porosity, *dimensionless*, page 6

ϕ_t Total porosity, *dimensionless*, page 7

ρ Fluid density, kgm^{-3}, page 3

σ Standard deviation in lognormal distribution, *dimensionless*, page 32

σ_0 Conductivity of the liquid, Sm^{-1}, page 8

σ_p Conductivity of a porous medium saturated with a liquid, Sm^{-1}, page 8

τ_e Electrical tortuosity, *dimensionless*, page 11

τ_g Geometrical tortuosity, *dimensionless*, page 11

τ_h Hydraulic tortuosity, *dimensionless*, page 8

θ Scale parameter in gamma distribution, same unit as x, page 32

Roman

$\bar{k}$ Permeability tensor, m^2, page 3

$\vec{v}$ Volume flux per unit area, ms^{-1}, page 3

A Cross-sectional area, m^2, page 7

a Regression factor, m^2, page 71

b Regression exponent tortuosity, *dimensionless*, page 71

c Kozeny constant, *dimensionless*, page 8

c_e Factor from equivalent channel model, *dimensionless*, page 8

c_k Factor from Katz and Thompson model, *dimensionless*, page 10

d typical length scale, m, page 3

e Regression exponent porosity, *dimensionless*, page 71

e_c Critical exponent, *dimensionless*, page 10

F Formation factor, *dimensionless*, page 8

g Gravitational acceleration, ms^{-2}, page 4

l_c Critical length scale, *dimensionless*, page 10

l_{maj} Average major axis length of ellipses fitted to the pores, m, page 32

l_{min} Average minor axis length of ellipses fitted to the pores, m, page 32

l_{tp} Scale from the two-point correlation function, m, page 32

m Exponent in Archie's law, *dimensionless*, page 11

n Reciprocal scaling factor, *dimensionless*, page 64

$n_{x/y/z}$ Number of observations, *dimensionless*, page 70

p Pressure, Pa, page 3

R Pore radius, m, page 7

r Correlation coefficient, *dimensionless*, page 6

r^2 Ratio of variance explained by a model to total variance, *dimensionless*, page 41

R_e Equivalent channel radius, m, page 8

Re Reynolds number, *dimensionless*, page 3

s Specific surface area, m^{-1}, page 8

S_2 Isotropic two-point correlation function, *dimensionless*, page 33

V Volume, m^3, page 7

v_f Fluid velocity, ms^{-1}, page 3

1 Introduction

Sea ice constitutes the boundary layer between ocean and atmosphere in high latitude seas and is thus considered a major element of the climate system (Thomas and Dieckmann, 2010). It regulates heat, momentum, and gas exchange between ocean and atmosphere and has a much higher albedo than open water, thereby insulating the warm ocean from the cold atmosphere. It is consequently of great importance to know the thickness, extent and properties of sea ice and to understand the associated growth and transformation processes down to the microscopic scale. Sea ice is a multi-component, multi-phase material consisting of ice crystals (solid), salt water (fluid), solid salts and air (Petrich and Eicken, 2010). As the salt dissolved in the ocean water cannot be integrated into the crystal structure during ice formation, it is either rejected into the underlying water layers or accumulated in water which becomes trapped in pockets or channels in the ice. This highly concentrated salt water is called brine and features salinity values ranging from 35 to 200 psu depending on temperature. The brine channels can form an interconnected system extending through the entire ice layer and therefore allow fluids to move up or downward through the ice cover. The potential extent of the transport of fluids through the ice can be characterized by the permeability of the ice. This study focuses on the variability of sea ice permeability, its interdependencies with other ice characteristics, and methodologies for its quantification.
The permeability of sea ice is relevant to numerous physical and biological processes, such as the vertical heat flux (Petrich and Eicken, 2010), the formation of melt ponds (Eicken et al., 2004), the exchange of CO_2 and other gases (Semiletov et al., 2004), sediment transport and release (Freitag, 1999), and the transport and distribution of both nutrients and flora and fauna in and under the ice (Cota et al., 1987; Fritsen et al., 1994).
The heat flux between ocean and atmosphere strongly depends on sea ice thickness. Two ice growth processes are related to the permeability, namely the formation of superimposed ice and of snow ice. If freshwater forms on the surface as a result of melting snow or ice and cannot run off due to low permeability, it may refreeze and form so-called superimposed ice (Kawamura et al., 2006). The second type - snow ice - forms when accumulated snow depresses the ice surface and the permeability is large enough for sea water to percolate upward through the ice and soak through the snow and freeze. This process has been reported to be important for the overall ice mass balance especially in the Antarctic (Maksym and Jeffries, 2000). The internal brine motion through convection or advection can also contribute several percent to the heat flux through the ice (Pringle et al., 2007; Lytle and Ackley, 1996). Convection is controlled by the permeability and known to lead to the desalination of the ice (Notz and Worster, 2008) and the densification of the water below the ice. In turn, convection changes the microstructure and thus the permeability of sea ice by introducing brine characterized by a level of salinity that is not in equilibrium with the *in situ* ice temperature.
The depth of melt ponds on the ice surface has also been reported to vary significantly with the permeability of the sea ice (Eicken et al., 2004). The albedo of melt ponds is much lower than that of ice or snow. By controlling the existence of melt ponds, permeability hence affects the integral albedo of the polar regions, which is known to be involved in a feedback process of global relevance (Covey et al., 1991). Remote sensing is also influenced by the permeability through its control of the amount of liquid found on the sea ice surface

(Thomas and Dieckmann, 2010).
In addition to the heat, salt, and melt water budget, sea ice permeability influences the CO_2 budget (Semiletov et al., 2004). Gas exchange between ocean and atmosphere can be facilitated or inhibited by open brine channels or impermeable layers of e.g. superimposed ice, respectively.
In the past, sea ice permeability has been determined by the following methods: the bail test in the field (e.g. Freitag (1999); Kawamura et al. (2006)), permeameter measurements on artificial or natural sea ice (e.g., Saeki et al. (1986); Okawa et al. (2003)) and tracer studies (Freitag, 1999). To date no research has been done on the relationship between the permeability of sea ice and microstructural parameters other than the porosity and two dimensional pore size distributions (Freitag, 1999).
The present work presents small-scale approach allowing for both microstructural analysis and permeability calculations. First, the microstructure of sea ice samples was imaged by non-destructive synchrotron x-ray computer tomography at higher resolutions than reported by Kawamura (1988) and Pringle et al. (2009). Thereafter, fluid flow through the structures was modelled with a numerical technique called lattice Boltzmann method (LBM). LBM has previously been used to determine the permeability of other porous media such as sandstone (Fredrich et al., 2006; Arns et al., 2004) and firn (Freitag et al., 2002; Courville et al., 2010), but has never been applied to sea ice. The purpose of this work is i) to evaluate the method described above and its applicability to sea ice, and ii) to study the relationship of permeability and microstructural parameters such as porosity, length scales, and tortuosity.
The following section presents detailed information about permeability in general, permeability measurements on sea ice, and different ideal and empirical models, followed by the identification of the indiviual study objectives. An extensive methodological section comprises the methodology of sample taking, imaging, and preparation, including the comparison of three image segmentation methods, as well as descriptions of microstructural analysis and the LBM model. The result section presents results from both LBM and microstructural analysis. Finally, the study results and the applied methods are discussed, before the last section highlights the conclusions that were drawn.

2 Background information

2.1 Definition of permeability

Permeability is a macroscopic characteristic of porous media describing the ability to transmit fluids. Henry Darcy discovered an empiric law (Darcy, 1856), later called Darcy's law, which relates the flux of a fluid through a porous medium to the pressure gradient with a proportionality constant consisting of the dynamic viscosity of the fluid and the permeability of the medium. In three dimensions it can be written like this:

$$\vec{v} = -\frac{\bar{k}}{\eta}\vec{\nabla}p \tag{2.1}$$

where $\vec{v}$ refers to the volume flux per unit area $\left[\frac{m}{s}\right]$, η to the dynamic viscosity $\left[\frac{kg}{ms}\right]$, and p to the pressure $\left[\frac{kg}{ms^2}\right]$. The unit of permeability is m^2 and in three dimensions the permeability $\bar{k}$ is a tensor realized by a symmetric, positive definite 3x3 matrix, which becomes a scalar for isotropic media. For sea ice one often studies the vertical permeability (k_{zz} of the tensor in the cartesian coordinate system). The volume flux $\vec{v}$ is related to the actual velocity of the fluid in the pores $\vec{v_f}$ through the porosity ϕ, defined as the ratio of the pore volume to the total volume, as in

$$\vec{v_f} = \frac{\vec{v}}{\phi}. \tag{2.2}$$

Darcy's law can be derived from the Navier-Stokes equations for fluid flow when averaging over a small volume (Sahimi, 1993). The assumptions made are stationary flow, incompressibility and a Reynolds number much smaller than 1, i.e. laminar flow. The Reynolds number (Reynolds, 1883) $Re = \frac{\rho v_f d}{\eta}$ is a similarity parameter for fluid flows and physically the ratio between inertial and viscous forces. Here ρ is the density of the fluid and d a typical length scale (e.g. pore diameter).

2.2 Sea ice structure and formation

Sea ice is a multiphase, multi-component system of pure ice, brine, solid salts and air. During freezing of sea water brine builds up between ice crystals. The crystals, that initially are oriented randomly, have a preferred growth direction, the basal plane. In quiescent conditions crystals with this growth direction oriented vertically, i.e. parallel to the temperature gradient, will grow faster and after a few centimeters of growth (the transition zone) most crystals will have this orientation. This process is known as geometric selection. Due to this and constitutional supercooling (Weeks and Ackley, 1986) the water-ice interface of sea ice has a lamellar structure and brine pockets have a vertically elongated shape, hence the name columnar ice. The details of this structure depend on both under-ice current, growth rate and seawater salinity. A typical distance between two brine layers is 0.3-0.5mm. In this work the coordinate system has been chosen such that for columnar ice the y-direction is parallel to the layers and the x-direction is perpendicular to the layers

(section 5.4ff).
In non-quiescent conditions ice crystals will be kept in suspension in the surface ocean until the slush layer becomes thick enough to reduce mixing. The thus formed layer will then freeze as a so called granular ice layer under which columnar ice can form. Granular ice is characterized by rounded crystals with random crystal orientations. Another ice growth process is the formation of snow ice. Snow ice is formed when the snow load depresses the ice surface under the water surface and sea water percolates upwards into the snow and refreezes. It also has a granular texture, which can only be distinguished from granular ice of different origin through its $\delta^{18}O$ content (Lange et al., 1990).
Ice of a different structure forms when fresh meltwater on the surface cannot run off and refreezes to superimposed ice (Kawamura et al., 2006) which is essentially freshwater ice without brine channels. In general the sea ice layer is made up of a combination of these different textures.
As the ice temperature changes, so does the microstructure. The brine and the ice are ideally in equilibrium meaning that the salt content of the brine is such that the freezing point of the brine is equal to the surrounding ice temperature. When the ice is warmed, internal melt takes place, the brine is diluted and the pores grow. For more information about sea ice structure and formation refer to Petrich and Eicken (2010) and Weeks and Ackley (1986).

2.3 Approaches to finding sea ice permeability and studying sea ice microstructure

Permeability measurements

A much used measuring technique to find sea ice permeability is the bail test on sack holes (e.g. Freitag and Eicken (2003)). A hole is drilled into the ice to a certain depth and the rate of the water rising in the hole to equilibrium is measured. The hole is usually sealed laterally to avoid fluid penetrating from the sides. This method is based on Darcy's law (equation 2.1). The pressure gradient is given by $\nabla p = g\rho\Delta H/\Delta L$ with the gravitational acceleration g, the fluid density ρ, the water level difference ΔH between two points at distance ΔL from one another. Assuming that only the ice of thickness L directly under the bore hole affects the water level this gives an exponential function for the hydraulic head $h(t)$, which is the difference between the water level at time t and asymptotic water level h_0 (sea level) $h(t) = h_0 e^{-k\frac{g\rho t}{\eta L}}$. Presuming lateral impermeability water level measurements give the vertical permeability. However, sea ice has been found to have a lateral permeability other than zero (Freitag (1999), typically one order less than vertical) and a correction factor was found by numerical modelling by Freitag (1999) to be proportional to the ice thickness under the hole L. The largest uncertainties in deriving the vertical permeabilities from such measurements are thus the lateral permeability, the lateral sealing of the hole and microstructure change through percolation of warmer brine through the ice (Freitag, 1999).
One can also measure permeability in the laboratory in a direct application of Darcy's law. Ice cores, often centrifuged, are set into an apparatus, called a permeameter, in which a specific pressure can be applied to a measuring fluid and its flux determined. Typical

measuring fluids are kerosene or n-Dekan (samples not centrifuged: Saeki et al. (1986), samples centrifuged: Freitag (1999)). It is possible to measure both lateral and vertical permeabilities with this method. Uncertainties are related to microstructure change during sampling as well as size effects (length of core).
The permeability of sea ice can also be derived from tracer studies of meltwater flow (Freitag, 1999; Freitag and Eicken, 2003). When dye is injected into the water of blind bore holes or meltwater ponds, the dye concentration in holes at some distance to the injection hole can be used to derive a vertically integrated lateral permeability using Darcy's law (equation 2.1), when the hydraulic head and/or wind stress over the pond are known. Uncertainties are related to the estimation of the driving forces and the decay rate of the dye (e.g. fluorescein, sulforhodamine (Freitag and Eicken, 2003)).

Microstructure imaging

In order to derive relationships between the permeability and mictrostructural properties such as the porosity one needs microstructure imaging techniques. There are three common types for sea ice:

- thin sections
- filling the pore space to make a cast
- tomography

The first method is to study traditional thin sections as e.g. Perovich and Gow (1996) - this introduces stereological problems and does not allow for a three-dimensional (3D) reconstruction of the pore space. Resolutions are on the order of 0.03mm within the 1mm thick sections. One possibility to attain a three-dimensional reconstruction is to make a cast of the pores as done by Weissenberger et al. (1992). After centrifuging at *in situ* temperatures sea ice samples were filled with water-soluble, low-viscosity resin which was polymerized under UV radiation. The ice was sublimated and the casts coated in gold and studied under an electron microscope. This yielded a resolution from $< 5\mu m$ to >30mm. However, this method is destructive and laborious.
Non-destructive 3D imaging is now possible at sufficient resolutions with both x-ray computed tomography (X-ray CT, Kawamura (1988); Pringle et al. (2009)) and magnetic resonance imaging (MRI, Edelstein and Schulson (1991); Eicken et al. (2000)). MRI discriminates between liquid- and solid-phase hydrogen atoms in an external magnetic field and has resolutions comparable to thin section analysis and sample sizes on the order of $(10cm)^3$. X-ray CT is based on the contrast of x-ray absorption coefficients for ice, air and brine and can produce images with resolutions one or more orders higher at sample sizes on the order of a few cm^3. In order to increase the contrast in x-ray CT one can either centrifuge the samples, so as to remove the brine or insert a chemical into the brine. The latter has been done by Pringle et al. (2009) (with a resolution of $41.5\mu m$) who grew ice crystals out of a solution containing CsCl, which restricts this method to artificial sea ice. Using highly intense and collimated synchrotron x-ray one can further increase the resolution. Because better resolution usually coincides with smaller samples, one has to find a balance between sample size and resolution.

2.4 Previous data

Vertical Permeabilities

Sea ice permeabilities take a large range of values. Following Freitag (1999) sea ice can be classified as effectively impermeable at permeabilities smaller than $5 \times 10^{-14} m^2$, highly permeable at permeabilities larger than $10^{-10} m^2$ and medium permeable in between.
The range of values of sea ice permeability from literature I am aware of is 10^{-16} to $10^{-7} m^2$. Both extremes were measured by Freitag (1999) who made the most extensive measurements. The results from the different studies are summarized in table 2.1.

Table 2.1: Overview over results from the literature

Source	Method	Ice	Vertical permeability in m^2
Saito and Ono (1978)	lab	artificial	10^{-13} to 10^{-12}
Ono and Kasai (1985)	lab	artificial	10^{-15} to 10^{-11}
Saeki et al. (1986)	lab	artificial	10^{-13} to 10^{-11}
Okada et al. (1999)	lab	artificial mushy zone	10^{-12} to 10^{-10}
Freitag (1999)	bail	natural summer	10^{-11} to 10^{-7}
Freitag (1999)	lab	natural summer and artificial	10^{-16} to 10^{-8}
Okawa et al. (2003)	lab	artificial mixture with frazil etc	10^{-9} to 10^{-10}
Eicken unpublished [1]	bail	natural summer	10^{-12} to 10^{-9}
Kawamura et al. (2006)	bail and lab	natural winter and artificial	10^{-11} to 10^{-10}

Empirical approximations

Freitag (1999) derived relationships between vertical permeability and a porosity, which corresponds to our imaged porosity, ϕ (see porosity definitions section 4.2) with correlation coefficients r from permeameter measurements of artificial young ice:

$$\begin{aligned} \text{For new ice: } k &= 10^{-19}(\frac{\phi_{im}}{1000})^{3.9};\ r = 0.86 \\ \text{For first-and multi-year ice: } k &= 10^{-14}(\frac{\phi_{im}}{1000})^{1.6};\ r = 0.87 \end{aligned} \tag{2.3}$$

Eicken et al. (2004) used the bail test method (no details published) and derived a relationship between the total porosity ϕ_t and the permeability k for first-year congelation sea ice with the correlation coefficients r:

$$\begin{aligned} k &= 4.708 \times 10^{-14} e^{0.07690\ 10^{-3}\phi_t} m^2 \text{ for } \phi_t \leq 0.096;\ r = 0.74 \\ k &= 3.738 \times 10^{-11} e^{0.007265\ 10^{-3}\phi_t} m^2 \text{ for } \phi_t \geq 0.096;\ r = 0.32 \end{aligned} \tag{2.4}$$

[1] shown in Thomas and Dieckmann (2010), may be data used in Eicken et al. (2004)

Lateral permeabilities

From tracer studies lateral permeabilities between 10^{-13} and 10^{-11} with a mean of $10^{-12}m^2$ were found in a ridged area (Freitag, 1999). In the laboratory Freitag (1999) found most anisotropic behaviour in columnar ice with the lateral permeability being up to two orders of magnitude lower than vertical (order $10^{-12}m^2$). Granular ice displayed only one order difference. Columnar ice had an additional horizontal anisotropy.

2.5 Models and analytical permeability relations

As one seldom knows the microstructure of sea ice in detail, one would like to find relations between the permeability and quantities that are more easily measured or modelled like pore size statistics and porosity. It is useful to make models and study the permeabilities of simpler geometries like uniform channels. In the following we introduce several types of models and theories which are to investigated:

- capillary models,
- Katz and Thompson model,
- percolation theory,
- a flow model.

Capillary models

The unconnected pipe model (Freitag, 1999) describes the pore structure as a set of unconnected vertical pipes of radius R_i. In one pipe the volume flow rate is given by Hagen-Poiseuille's law:

$$V = \frac{\pi R_i^4}{8\eta}\frac{\Delta p}{\Delta L}. \tag{2.5}$$

With the volume flux from a one-dimensional version of equation 2.1 being $v = \frac{V}{A}$ with A being the cross-sectional area of the pipe, the permeability becomes

$$k_i = \frac{R_i^2}{8} \tag{2.6}$$

The permeability of a set of unconnected pipes of this type is equal to the sum of the pipe permeabilities weighted with their portion of the volume.

$$k = \sum_i \frac{A_i}{A} k_i \tag{2.7}$$

The porosity is expressed as $\phi = \sum_i \frac{A_i}{A}$.
In order to use this formula to calculate the permeability from pore size frequency distributions one can rewrite it to:

$$k = \sum_j \frac{A_{R_j}}{A_p} \phi k_j = \phi \sum_j \frac{A_{R_j}}{A_p} \frac{R_j^2}{8} \tag{2.8}$$

where A_{R_j} refers to the collected area of all pipes with a radius R_j, k_j their permeability and A_p the total area of all pipes. Applying this model to sea ice overestimates the permeability due to interconnectivity (Freitag, 1999).
For the case where all pipes have the same diameter R, this becomes

$$k = \phi \frac{R^2}{8}. \tag{2.9}$$

Torquato (2002) derived a general formula for steady-state fluid flow in a hyperspherical pore of dimension D and radius R, where D=1 corresponds to flow between layers and D=2 the above mentioned flow in a pipe: $k = \phi \frac{R^2}{D(D+2)}$, where R is half the length of the slot or the radius of the pipe. Torquato (2002) also rewrote the relationship for cylinders of arbitrary shape resulting in Kozeny's equation:

$$k = \frac{\phi^3}{cs^2} \tag{2.10}$$

with s the specific surface (i.e. surface area per unit volume) and c the Kozeny constant ($c = 2$ for circular pipes and $c = 3$ for layers). Empirically $c = 5$ works well for many media (Torquato, 2002).
Kozeny's equation has been modified by separating the Kozeny constant into a shape constant β and the hydraulic tortuosity τ_h (for discussion of tortuosities see section 2.6). This produced one of many forms of the Kozeny-Carman relation (Carman, 1956):

$$k = \frac{\phi^3}{\beta \tau_h^2 s^2} \tag{2.11}$$

The Kozeny-Carman relation assumes microscopic homogeneity and a narrow pore size distribution (Freitag, 1999). For wider pore size distributions this relation tends to underestimate the real permeability (Clennell, 1997).
The equivalent channel model (Paterson, 1983) has the same form. The hydraulic tortuosity is replaced by the formation factor $F = \sigma_p/\sigma_0 = \tau_e^2/\phi$ where σ_p is the conductivity of the solid saturated with a liquid of the conductivity σ_0 (see section 2.6):

$$k = c_e \frac{R_e^2}{F} \text{ with } R_e = \frac{\phi}{s} \tag{2.12}$$

The range of values of the factor c_e (1/2 to 1/3) stems again from ideal geometries like pipes and layers. The most critical part of this model is the concept of the hydraulic radius (Paterson, 1983). It is most suitable for media with low porosities (Freitag, 1999).
This model can also be used in conjunction with porosities, specific surface areas and a

characteristic pore size estimated from two-point correlation functions (Blair et al., 1996; Berryman and Blair, 1987).
For all relations including the specific surface area s one has to keep in mind the roughness of the surface (Carrier, 2003; Berryman and Blair, 1987) as increasing the resolution of the surface will in general lead to a larger measured surface and hence a smaller modelled permeability even though the fluid might just pass by the irregularities. Both Kozeny and Kozeny-Carman relation and the equivalent channel model have been applied for different types of natural and simulated sandstones (Arns et al., 2005; Berryman and Blair, 1986; Blair et al., 1996). Only the Kozeny-Carman relation in its form relating the permeability to the grain size d_g ($k = \frac{\phi^3 d_g^2}{180(1-\phi^2)}$, Bear (1988)) has been applied for sea ice (Maksym and Jeffries, 2000). For sea ice one would expect only capillary models including a tortuosity and an adaptable shape factor to give reasonable results. In this way one could include information about the very variable microstructure of granular and columnar ice. Also one should work with porosity dependent length scales or specific surface areas.

Capillary rise When talking about capillary models, one should touch upon capillary forces. A wetting fluid will rise inside a pore above the level of zero pressure due to an upward force produces by the attraction of the fluid molecules (brine) to the solid wall (ice). This process is called capillary rise. Its height depends on the contact angle between liquid and solid and the surface tension of the liquid and the pore shape (Coleou et al., 1999). It does not affect pressure driven flow and hence the permeability as such, but might affect the distribution of brine in the ice. For a water air surface at 0°C the surface tension is $\gamma = 75.64\ 10^{-3} N/m$. For a wetting fluid in a cylindrical pore of radius R the height of the capillary rise is $h_c = \frac{2\gamma}{\rho g R}$. For a sea water density $1027 kg/m^3$ and pore scales of $0.1mm$ and $1mm$ found in sea ice capillary rise would be between 1 and $15cm$. The process of capillary rise has been discussed and modelled for snow (Coleou et al., 1999; Geldsetzer et al., 2009). From $\delta^{18}O$ and salinity measurements in the lowest snow layer Toyota et al. (2007) concluded that seawater percolation was much more important than capillary rise of brine in wetting the snow.

Katz and Thompson model

Katz and Thompson (1986) arrived at a relationship of the same form as equation 2.12 from percolation considerations assuming a broad distribution of pore sizes. They argued that the transport is controlled by the smallest pore of a set of the largest pores that percolates through the medium. This pore of size l_c can be found through mercury intrusion porosimetry (MIP, Moro and Böhni (2002)). In MIP mercury is pressed into a sample of a porous medium. The relationship between applied pressure and adsorbed volume is related to the diameter of the pores which are reached (depending on the pore shape). The pressure (or diameter) at which there is a strong increase in adsorbed volume (inflection point of the cumulative curve) represents the critical pressure or diameter l_c. The Katz and Thompson model became:

$$k = c_k \frac{l_c^2}{F} \tag{2.13}$$

Here c_k is a constant which for locally cylindrical geometry is proposed to be $c_k = 1/226$. This factor has later been shown to be 2 to 4 times larger and dependent on anisotropy (Le Doussal, 1989). The Katz and Thompson model has previously been used for sandstone (Arns et al., 2005) but not for sea ice. As the factor c_k has shown variations within about one order of magnitude for a broad range of shapes (Schwartz et al., 1993), we would expect this model to perform for sea ice as well as for other media. Both percolation effects and connectivity are included in this model through l_c and F, respectively.

Percolation theory

Percolation theory (Golden et al., 2007; Torquato, 2002; Pringle et al., 2009) describes behaviour of random materials dominated by the connectedness of one phase. One models the system by for instance a network of points on a lattice connected by bonds. Each bond has a probability to be open (P) or closed ($1 - P$), independently from each other (i.e. „Bernoulli“ percolation). The question is if there is an open path from top to bottom of the system. With increasing P longer open paths exist. For a certain critical probability P_c, also called the percolation threshold, and for all probabilities $P > P_c$ infinite paths exist. This threshold can be found explicitly for some geometries, e.g. for a square lattice in two dimensions $P_c = \frac{1}{2}$. For a cubic lattice $P_c \approx 0.25$. Below the percolation threshold there is no flow all the way through the system and above the threshold it increases with P until the maximum is reached at $P = 1$.
Near the critical point you find the critical phase where properties such as the percolation probability (which is the probability that a bond belongs to a infinite cluster) or the permeability can be described by power-law scaling. For the permeability this becomes:

$$k = c_p(P - P_c)^{e_c} \text{ for } P \to P_c^+ \text{ and } |P - P_c| \ll 1 \tag{2.14}$$

with the permeability critical exponent e_c and a scaling factor c_p. One believes that e_c is universal for lattices, only dependent on the dimension. In three dimensions $e_c \approx 2$ with a rigorous bound ≤ 2 (Golden et al., 2007). For the continuum e_c can vary, but when using a lattice with a lognormal probability density of bond conductances (reflecting the lognormal distribution of sea ice pore sizes found by Perovich and Gow (1996)) e_c is found to be approximately 2 nevertheless (Golden et al., 2007). From data from Ono and Kasai (1985) Golden et al. (1998) estimated the permeability critical exponent of sea ice to be $e_c \approx 2.5$.
That sea ice has been found to be effectively impermeable for porosities below 5% and above increasing rapidly (Cox and Weeks, 1975; Weeks and Ackley, 1986) indicates that the theory of a percolation threshold can be applicable here. The probability of an open bond is there given by the porosity (Torquato, 2002). At a salinity of 5 ppt the critical porosity of 5% corresponds to a temperature of about -5°C, which is why Golden et al. (1998) called the critical behaviour the „law of fives“. The critical porosity depends on the actual structure and granular ice would likely have a higher critical porosity (Golden et al., 1998).
Pringle et al. (2009) combined percolation theory with 3D imaging with x-ray computed tomography and derived the critical exponents for the actual microstructure of single sea ice crystals evolving between -18 and -3°C. They used finite size scaling (Torquato, 2002)

for the percolation probability at several porosities and found critical porosities of 4.5% in the vertical, 9% in the horizontal parallel to brine layers and 14% in the horizontal perpendicular to brine layers.

Flow model

A computational fluid dynamics model has been used to model sea ice growth to derive relationships between permeability, effective and total porosity for growing first year sea ice by Petrich et al. (2006). They based their theory on data on the desalination of artificial sea ice by Cox and Weeks (1975) and used a Monte Carlo percolation model to derive a relationship between effective and total porosity. Their analysis resulted in the following expression for the vertical permeability assuming in- and outflow in a half circle and an anisotropy of one order to the horizontal:

$$\begin{aligned} k = 7 \times 10^{-10}(\phi_t - 0.054)^{1.2} m^2 \text{ for } \phi_t > 0.054 \\ k \leq 7 \times 10^{-13} m^2 \text{ for } \phi_t \leq 0.054 \\ k \to \infty \text{ for } \phi_t \to 1 \end{aligned} \tag{2.15}$$

with a critical porosity of 0.054.

2.6 Tortuosities

One factor that appears in many permeability approximations is the tortuosity, which describes the sinuosity and interconnectedness of the pore space (Clennell, 1997). However, there are many different definitions of tortuosity - Clennell (1997) give a good overview and discussion for isotropic and homogeneous media. In the context of this work I want to mention the geometrical, hydraulic and electrical tortuosity as defined by Clennell (1997). The geometrical tortuosity τ_g is the ratio of the shortest path within the pore space between two points l_{eg} and the euclidean distance l between them. The tortuosity of the whole pore space is an average value. This tortuosity is not commonly used in permeability relations. The hydraulic tortuosity τ_h is related to the length of fluid flow path l_{eh}, which can be longer than the distance in τ_g since the fluid path is smoother (see figure 2.1). This figure illustrates also that the hydraulic tortuosity is influenced by changes in pore diameter. In the case of a wide pore size distribution there is likely also a wide range of tortuosities and applying one factor of tortuosity might not suffice.

The eletrical tortuosity τ_e is related to the formation factor introduced in section 2.5 $F = \sigma_0/\sigma_p$ with the conductivities σ of the solid saturated with a liquid of conductivity σ_0. It has been found that the formation factor is related to the porosity in the following way $F = X_e/\phi$. The factor X_e has been related to some effective electrical path length l_e by Cornell and Katz (1953) leading to the electrical tortuosity $\tau_e = l_e/l = \sqrt{F\phi}$. Like the hydraulic tortuosity this tortuosity is affected by changes in pore diameter (Clennell, 1997).

Archie's law relates the formation factor for rocks to the porosity like $F = \phi^{-m}$. The factor m has been found to lie between 1.3 and 3.0 and is related to the relation between throat and pore body area. The relationships between these tortuosities are only partly

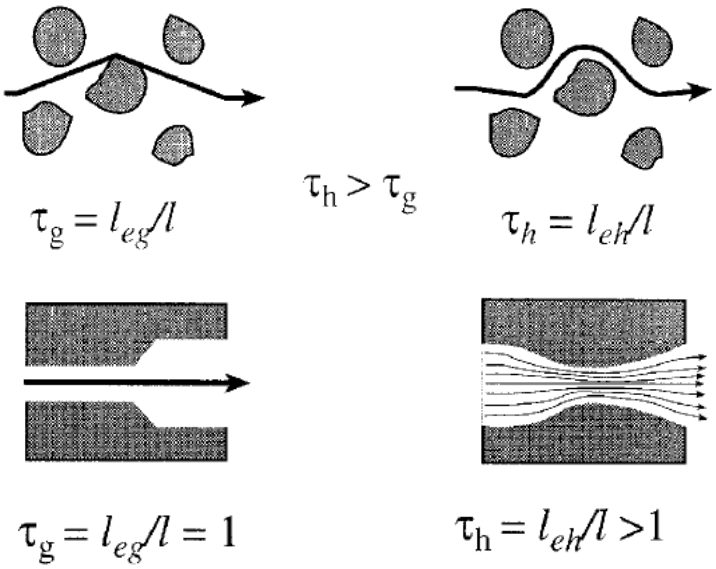

Figure 2.1: The difference between geometrical τ_g and hydraulic τ_h tortuosity, adapted from Clennell (1997); l euclidean distance between two points, l_{eg} shortest path within the pore space between two points, l_{eh} length of the fluid flow path within the pore space between two points

established. The hydraulic tortuosity is only equal to the electrical if the pore space is used in the same way for eletrical and hydraulic transport. However, this has been shown to not generally be true (Clennell, 1997).

3 Objectives

The following open issues related to sea ice permeability that were introduced in the previous section will be addressed in this thesis:

- Many common models and methods for permeability determination from other geosciences have not been tested for sea ice microstructure which has very different characteristics than for example sandstones. This refers to some of the capillary models, as well as using the formation factor and mercury intrusion porosimetry to predict the permeability.
- Lateral permeabilities and the related anisotropy have only been studied by Freitag (1999) even though this factor is vital to correct all bail test measurements for lateral inflow and of importance for melt ponds.
- There are no quantitative studies relating the permeability to microstructure parameters other than porosities.
- To date fluid flow through the pores of sea ice has never been modelled. The only other publication about flow through sea ice from a microscopical perspective is Pringle et al. (2009) where a percolation approach is taken.

The objective of this thesis is to both develop and evaluate a method of microstructure analysis and flow modelling and study the permeability in all three directions of young sea ice with respect to its microstructure. The assessment of the applicability of this method and its limitations will be valuable for further studies of sea ice permeability. New insight into the permeability dependency on the microstructure will improve future models of e.g. snow ice formation, melt pond development and biological activity in the ice.

4 Methods

4.1 Sampling and segmentation

Data for this project is a set of cores of young sea ice with a reconstructable temperature history taken in March 2009 close to Ny Ålesund on Svalbard. These cores were centrifuged at *in situ* temperatures removing free brine to increase the contrast between brine channels and ice in the x-ray microtomography. After some storage at -80°C the samples were transported to Switzerland for synchrotron-based x-ray microtomography (SXRT). The resulting 3-dimensional images of the sea ice samples were then segmented, i.e. channel and ice voxels (volume element, 3D pixel) defined, by three different methods in order to find out which one is most adequate. In the first method each layer is segmented separately by thresholding with an objective algorithm using Matlab®, in the second the same algorithm is applied in three dimensions in Matlab® and in the third the whole sample is segmented at once in Amira® with a subjective threshold. In order to compare the segmentation methods simple microstructure analysis was performed. In the following these steps preparing the data for lattice Boltzmann modelling will be explained further.

Sample taking and preparation

During field work we were met by favorable ice conditions in Kongsfjorden so that ice cores could be taken at about the same place about 500m from the Ny Ålesund harbour on 10., 11. and 13.3.2009 (stations 1, 2 and 4, respectively). Ice cores were also obtained from the inner part of Kongsfjorden on snow mobile excursions and from a laboratory ice tank experiment carried out in the Marine Laboratory in Ny Ålesund. A scene from sampling on Kongsfjorden in shown in figure 4.2. All in all approximately 80 samples from 6 natural and 5 laboratory cores were prepared for microstructure imaging. However, this thesis deals only with samples from the cores from stations 1, 2 and 4. Meteorological conditions (figure 4.1) and hydrographic measurements indicate that the ice from these stations most likely started forming 2 to 3 weeks prior to sampling and grew slowly due to upwelling Atlantic Water to a thickness of 13-14cm (Maus et al., 2011). Information on these samples is presented in table 4.1. The temperatures were calculated assuming a linear temperature gradient between the snow ice interface and the ice water interface. The temperature and bulk salinity profile from station 2 (consisting of samples 2c1, 2a2, 2a3 and 2a4) are shown in figure 4.3. The bulk salinity decreased with depth. Maus et al. (2011) showed also the profiles of bulk salinity for stations 1 and 4, taken one day before and two days after station 2, which have lower salinities in the top layers and higher at the bottom. It is not possible to say whether these differences are related to horizontal variations of salinities in the ice or to change in air temperature over time.

The sampling procedure was as follows:

- Take at least 2 ice cores (7.25 cm diameter coring device (Mark III, Kovacs Entrerprise)), measure the temperature profile, cut them into samples of about 3cm thickness.
- Keep the samples of one core at their approximate *in situ* temperatures in a plastic beaker on their way to the centrifuge. We estimate that the storage temperatures were

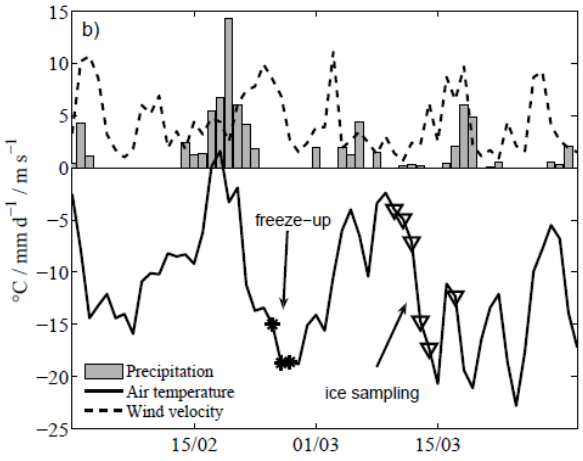

Figure 4.1: Meteorological conditions (air temperature, wind velocity and precipitation) in Ny Ålesund during approximate freeze-up and sampling, reprinted from Maus et al. (2011)

within $\pm 0.5K$ of the *in situ* temperatures except for sample 1b1, which was stored $1.4K$ too cold. This step was accomplished by two different methods depending on the distance to the laboratory. Either - for short distances - the ice cores were transported in small styrofoam boxes to temperature-controlled freezers (WAECO Coolfreeze T56) that were kept at the respective temperatures in the lab or - for long distances - the freezers were taken along on snow mobile sledges and powered by the snow mobile engines or an aggregate to transport the samples back to the laboratory. The temperatures the freezers were set to were estimated from the surface temperature and a linear temperature profile.

- Centrifuge those samples at the respective approximate *in situ* temperatures at 300 revolutions per minute for circa 15 minutes (refrigerated Centrifuge Sarstedt LC 1K) which corresponds to 10xg.
- Freeze the centrifuged samples to -80°C.
- Cut out 2x2cm cylinders and melt the rest and measure its conductivity at room temperature (WTW Cond340i).
- Store on dry ice or in a -80°C freezer until SXRT measurements could be taken.
- Weigh the collected brine from drainage and centrifuging and measure its conductivity at room temperature (WTW Cond340i).
- Melt the other core as a bulk core and measure its conductivity at room temperature.

During the whole process the natural orientation of the ice samples was maintained. The result of cooling the centrifuged samples to -80°C was that the dissolved salt in the brine that was not removed (either because it was in closed brine pockets or because the centrifugation was ineffective) precipitated as crystals and could therefore easily be distinguished from ice and the now air-filled brine channels in the CT images.

Table 4.1: Description of the 7 samples, ice thickness for all samples 14cm, snow thickness 4-5cm; sample size is the size used in the LBM model, some samples were cut in the vertical for homogeneity

Name	Date 2009	Depth [cm]	*in situ* T [°C]	Bulk salinity [psu]	Ice type	Number of cells	Sample size [voxel, 35μm]
1a3l	10.03.	8.0	-1.9	5.6	columnar	7	367x385x200
1b1	10.03.	1.9	-2.2	7.5	mixed	12	330x366x491
2a2	11.03.	4.7	-2.0	7.0	columnar	12	317x370x491
2a3	11.03.	7.9	-1.9	6.8	columnar	12	367x324x228
2a4	11.03.	11.3	-1.8	5.0	columnar	7	386x351x310
2c1	11.03.	1.5	-2.1	9.2	granular	12	371x374x491
4c1	13.03.	1.95	-3.0	7.7	mixed	12	338x341x491

In addition biochemical analysis of brine and ice was done and included chlorophyll, DOC (dissolved organic carbon), DOM (dissolved organic matter) and ion measurements (Maus et al., 2011).

Figure 4.2: During sampling on Kongsfjorden

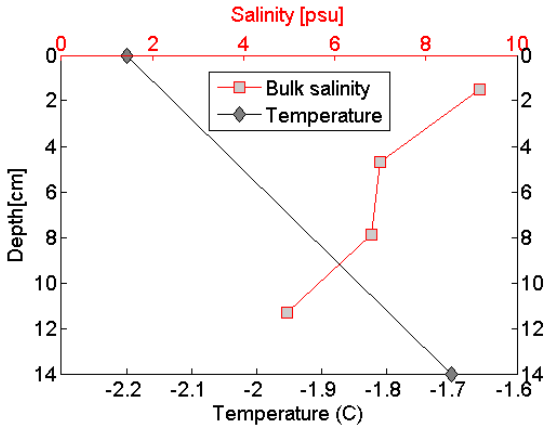

Figure 4.3: Vertical profiles of temperature and salinity

Synchrotron-based x-ray microtomography

Synchrotron-based x-ray microtomography (SXRT) was conducted on a specially constructed cooling stage at the tomography beamline (TOMCAT) of the Swiss Light Source synchrotron at the Paul Scherrer Institute in Villigen, Switzerland in April 2009. The TOMCAT gets photons from a 2.9 Tesla superbending magnet with a critical energy of 11.1 keV. The energy used for the experiments can be selected with a Double Crystal Multilayer Monochromator within a range from 6 to 45 keV. Our images were taken at 13keV. Informations on the experimental conditions are summarized in 4.2 and the set-up shown in 4.4. The cooling stage was developed by the University in Mainz and the Swiss Light Source synchrotron and ensured that the ice temperature did not exceed -40°C by cooling the sample holder with a Cryojet - a stream of cold nitrogen gas (Kersten et al., 2006). It was not possible to take images of the whole samples, so images were taken in four overlapping stacks of 0.4cm height, which took in total about 30 minutes during which it was possible to keep the samples below -40°C. During rotation around a vertical axis 1016 projections were taken and 2x2 binned resulting in a voxel size of $11.84\mu m$. Afterwards the 3D structure was reconstructed. The resulting data for one sample consist of four stacks of 366 cross-sectional slices of 1532x1532 pixels size stored as unsigned 8bit TIFF files. The four stacks belonging to one sample overlapped by 5 slices and were set together where possible without rotation to produce images of 1532x1532x1449 voxel size (ca. 1.8x1.8x1.7cm^3). Subsequently the image was filtered with a 3D median filter with a kernel size of 3x3x3 in order to remove noise while preserving edges. This was done with the Amira® software.

Table 4.2: Experimental conditions at TOMCAT

Beam energy	Magnification	Numerical aperture	Field of view [mm^2]	Pixel size [μm^2]	exposure time	number of projections
13keV	1.25	0.06	ca.21x21	5.92x5.92	100ms	1016

Segmentation and cropping

Segmentation is a vital step in the preparation of 3D images to further analysis. For most applications one does not need an image with values of a 256 gray scale (figure 4.6(a)) but an image were each voxel is classified as ice or air (figure 4.6(e)). There is also a possibility to define salt, but this was not necessary for the permeability calculations and more difficult since the salt peak in the histogram was overlapping with the ice peak (4.6(d)).
Two major categories of thresholding are local and global thresholding. In global thresholding one single gray scale value is chosen for the whole image as a threshold for the two classes to be defined. In local thresholding only a certain region of voxels around the voxel to be classified is taken into account when computing a threshold (Sezgin and Sankur, 2004). Local methods give superior segmentation results and can avoid some image artefacts (e.g. beam hardening and high-frequency noise, Iassonov et al. (2009)), but require more computational power. We assumed our data of good enough quality to use global

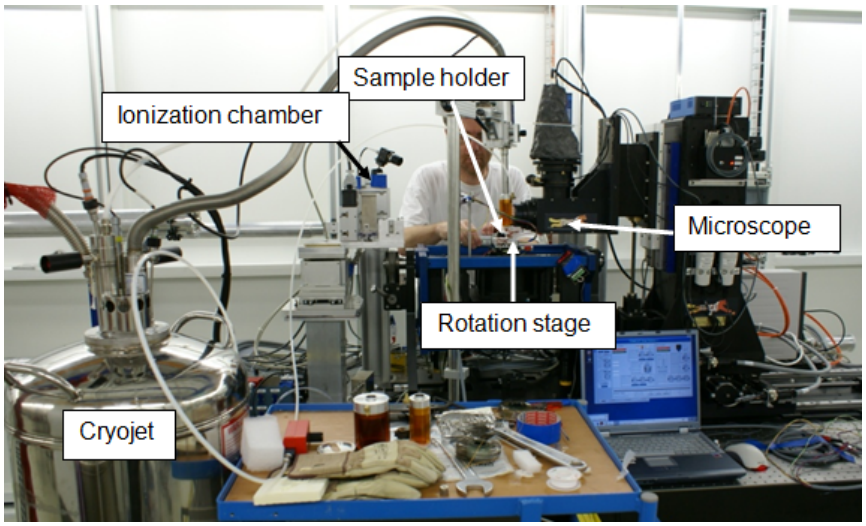

Figure 4.4: The experiment setup at TOMCAT, picture by Sönke Maus

thresholding without large errors. Our images did show ring artefacts, which fortunately were not very prominent. Slicewise processing in 2D - i.e. thresholding each horizontal section separately - which we tested as one of our methods is known to have major drawbacks as it disregards many neighbouring voxels, introduces directional bias and might not include enough information to represent both voxel classes (Iassonov et al. (2009); Elliot and Heck (2007), see figure 4.5). Another problem associated with using thresholding algorithms on our data is that there were actually 3 classes - ice, air and salt. The salt peak which was overlapping with the ice peak distorted the histogram, affecting algorithms assuming two normal distributions. This could be avoided by manually setting the threshold through visual inspection. This however has the disadvantage of subjectivity.

The three methods we compared as the first part of this work are all of the type global

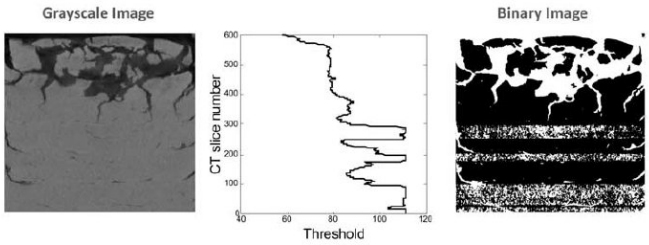

Figure 4.5: Illustration of possible problem with automated 2D slicewise processing from Iassonov and Tuller (2009)

thresholding - two of them setting the threshold automatically using the Software Matlab® (one in 2D (slicewise), referred to as method A, and one in 3D, referred to as method B), and one setting the threshold manually using the Software Amira® in 3D (referred to as method C).

Automatic segmentation - Method A and B First the ring on the images resulting from the plastic tube that was used to hold the ice in place (figure 4.6(a)) was removed in

order to get a correct histogram only containing ice and air pixels and in order to be able to define the total ice-and-air domain. This was done by choosing the radius and centre on one slice and removing everything outside of this circle (figure 4.6(c)).
Subsequently, the actual segmentation took place. The threshold between air and ice was set using the algorithm by Otsu (Otsu, 1979), implemented in Matlab as *graythresh* (Program functions are in the following referred to in italics). This algorithm finds the intensity value that minimizes the variance within the classes and maximizes the variance between the classes. Otsu's method has been shown to perform well and consistently by Iassonov et al. (2009). Sezgin and Sankur (2004) also found quite good results for this widely used algorithm under the condition that there are about equally many pixels in the two classes (here air and ice). In spite of porosities on the order of 10% this was the case for our data, because of the air surrounding the ice sample in the images. The threshold was then used to produce a binary image of air and ice - in method A in 2D, slicewise and in method B in 3D, i.e. globally.
Subsequent processing was done in the same way in both method A and B: Regions of connected pixels of ice were labelled in each slice (*bwlabel*) and their properties (*regionprops*) used to define the ice sample and find the smallest convex polygon that contained the ice sample in that slice. The intersect of all these polygons with 50 pixels removed from all edges (*bwdist*) was then used as the base of the cylinder that was cut out. Removing edge pixels was done to reduce the number of pixels of surrounding air being classified as pore by the convex polygon (see regions indicated by arrows in figure 4.6(c)). The result of this step was a convex polygonal cylinder containing a binary image of ice and air with defined exterior around (figure 4.6(e)).

Manual segmentation - Method C In order to be able to compare the result of the manual with the automatic segmentation the same convex polygonal cylinder was selected from the filtered data. Then the threshold was set using the thresholding tool in the segmentation editor of Amira® checking the quality of the segmentation visually for different horizontal and vertical sections. This is a subjective method. Its advantages are that one can easily identify problem zones and that salt could also be classified which is not possible with the type of automatic segmentation we chose.

Microstructure analysis Before further analysis regions of connected air voxels smaller than 5 voxels were removed, assuming that they are products of wrong classification during segmentation due to noise in the images. It is also possible that they are small air pores, but either way do these regions not contribute to the permeability. Connectivity was defined in 4 directions for two dimensions and in 6 directions for three dimensions - i.e. diagonally neighbouring pixels are not considered connected. The samples showing with elliptic pores with the major axes having a preferred direction (*regionprops*), i.e. the columnar samples, were turned so that the preferred direction (the layers) was parallel to the y coordinate.
In order to compare the three segmentation methods A, B and C a number of basic quantities were derived from the binary images:

- Porosity ϕ

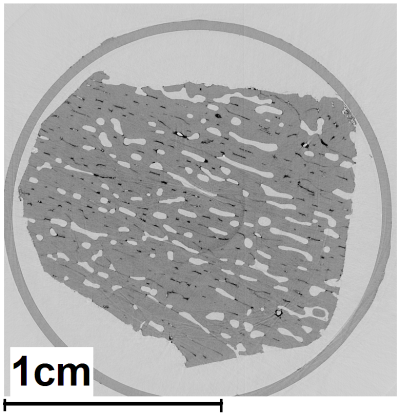

(a) Original image

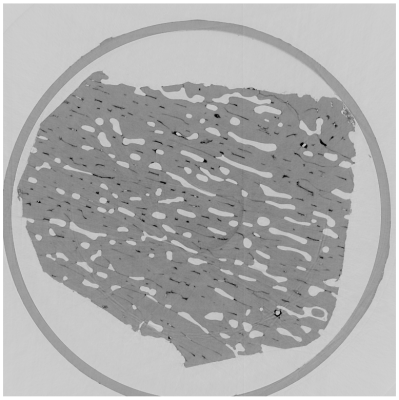

(b) After median filter

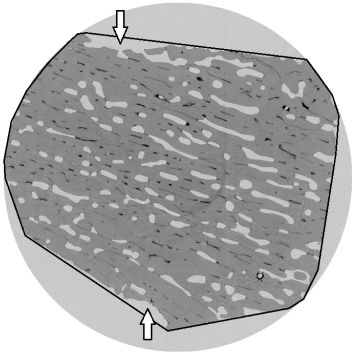

(c) After removal of ring

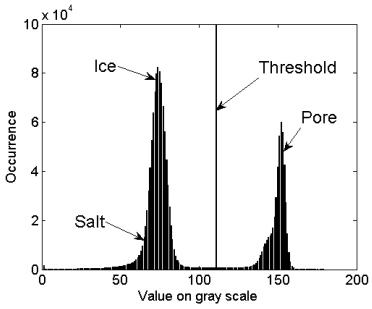

(d) Histogram

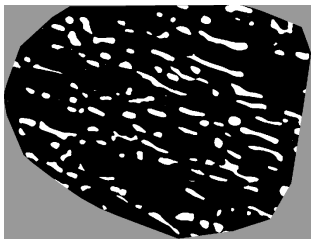

(e) Final result

Figure 4.6: Example of segmentation process (Method A/B) for sample 2a2, slice 200: (a), (b), (c): air appearing light gray, ice dark gray, salt very dark, colours have been changed a little to make the difference between salt and ice visible in the print version; (c) including a sketch of the smallest convex polygon containing the ice sample and arrows indicating the regions where exterior is defined as pore before removing 50 edge pixels, (d) histogram of the image in (c) with the threshold marked as a vertical line, (e) final result: pores appearing white, ice black and surroundings gray;

- Pore surface to volume ratio (specific surface area s divided by ϕ)
- Open porosity fraction (fraction of the pore volume that is connected from top to bottom in a sample)

The pore volume was computed by counting the pore voxels. The pore surface however required some more attention. The fastest estimation of the surface is given by counting edge voxels. This however is an underestimation of the surface, as the surface of a pore can be given by multiple faces of a voxel. Another method is to count all the faces that make up the interface. This would overestimate the actual surface because of the steplike structure that the natural interface does not have. Also, the surface would depend on the orientation of the image. For the segmentation comparison the surface was taken as the number of edge voxels times the area of a voxel. In the later sections the surface area was calculated by the software GeoDict (ITWM (2009)). The open porosity fraction was found by labelling connected regions of pores (*bwlabel*) and testing whether or not the regions touch the top and bottom layers of the sample.

Comparison of segmentation methods In the following the three segmentation methods are compared for the three samples 2a2, 2a3 and 2c1, of which a horizontal section is illustrated in figure 4.7. Sample 2c1 was taken close to the surface and shows a granular structure, as can be expected for frazil or snow ice. The two columnar samples 2a2 and 2a3 were from the medium and bottom layer of the ice, respectively. To attain a larger variation of porosities, the segmentation was done separately for 4 stacks of 366 slices in each sample. In figure 4.8(a) the threshold value of the 8-bit grayscale set by each method is displayed. For method C one stack from each sample was segmented repeatedly with the maximum and minimum of threshold that looked correct - this is shown by the black errorbars. The range of these thresholds was less or equal to 6. In figures 4.8(b)-(d) these error bars are not shown because they are too small. For method A the mean of the thresholds of all slices is shown in red together with the range of threshold values found in the stacks. Maximum variation within method A was found in stack 4 of sample 2a3 with a range of 5. Also presented in figure 4.8 are porosity, s/ϕ and open porosity fraction. Porosities found were between 3.6% and 14.8%, pore surface to volume ratios between 0.57 and $1.49\times10^4 m^{-1}$ and open porosity fractions between 0 and 95.9%. Figure 4.9 presents the deviation of threshold of methods A and C from method B divided by the air-ice-contrast (distance between the peaks in the histogram - this is very similar in all samples and was taken to be 78) and the relative deviations of methods A and C from method B for porosity, pore surface to volume ratio and open porosity fraction. Method B was chosen for reference because it was expected to be the most accurate one, as discussed above. With maximum deviations on the order of 6% for the threshold, 3% for the porosity and 4% for the pore surface to volume ratio and up to 10% for the open porosity fraction (this high number being an exception) the three methods gave very similar results. For the three cases where the threshold was the same in method B and C (2a2-3 and 2a3-4 and 2c1-1) all other quantities were not the same. This is because a mistake was made in the Matlab segmentation, leading to a slighly increased porosity. This mistake was fixed in all samples to be analyzed further, but because it does not change the outcome of this

comparison of segmentation methods, it was not corrected here.

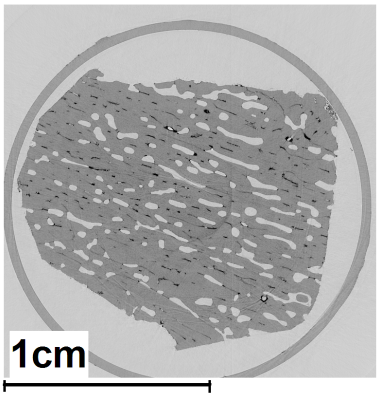

(a) 2a2

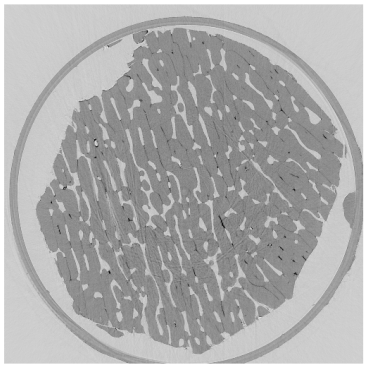

(b) 2a3

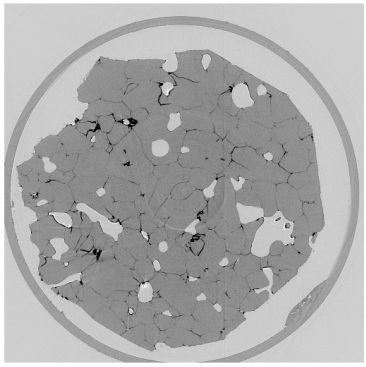

(c) 2c1

Figure 4.7: Slice 200 of each of the three samples used for comparing the methods, the colours have been changed a little to make the difference between salt and ice visible in the print version

The high value of 10% for the deviation of the open porosity fraction might be a consequence of one or more narrow channels closing at a higher threshold value. This illustrates that the open porosity fraction can be quite sensitive to relatively small changes in the threshold value. The sensitivity to the threshold value was studied by applying method C with 7 different threshold values (from 107 to 113) on stack 2 of sample 2a3. The results are shown in figure 4.10. For porosity and pore surface to volume ratio there was a perfectly linear relation ($r^2 = 1$) with the slopes $\frac{\Delta\phi}{\Delta T} = -6.34 \times 10^{-4}$ and $\frac{\Delta(s/\phi)}{\Delta T} = 46.50 m^{-1}$ with ϕ,s and T referring to porosity, specific surface area and threshold respectively. The open porosity fraction showed discontinuities rather than a linear trend, as it is sensitive to channels that open or close with varying thresholds.

With the similarity of the three methods in mind we chose method B - Matlab with the 3D threshold - as the most adequate for our purpose. The reasons were:

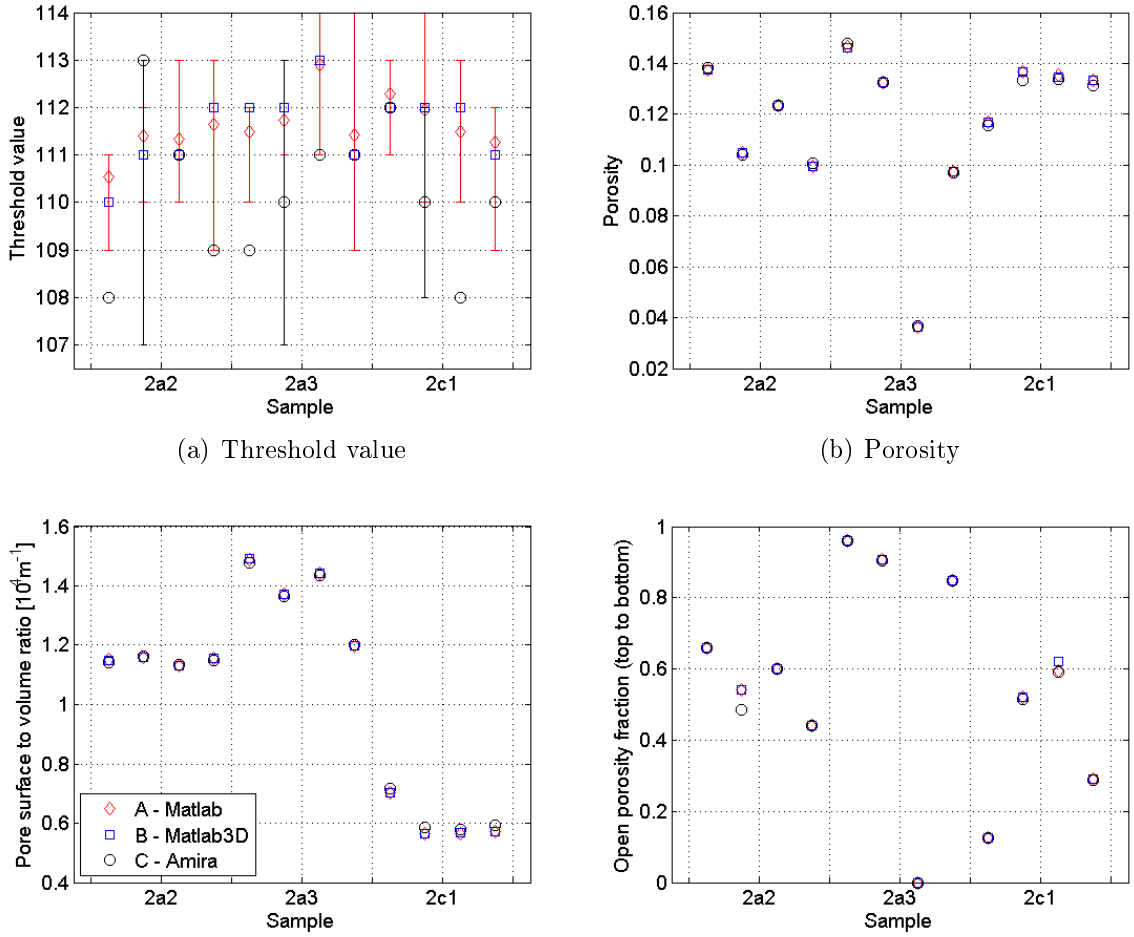

(a) Threshold value

(b) Porosity

(c) Pore surface to volume ratio

(d) open porosity fraction

Figure 4.8: Comparison of the three segmentation methods, absolute: Threshold value, porosity, pore surface to volume ratio and open porosity fraction for methods A, B and C for 3 samples with 4 stacks each. For method A all thresholds lie within the red error bar with the diamond marking the mean. Method C has been applied several times to find the extremes of possible thresholds which are demarked by the black error bar. The legend is valid for all graphs in this figure.

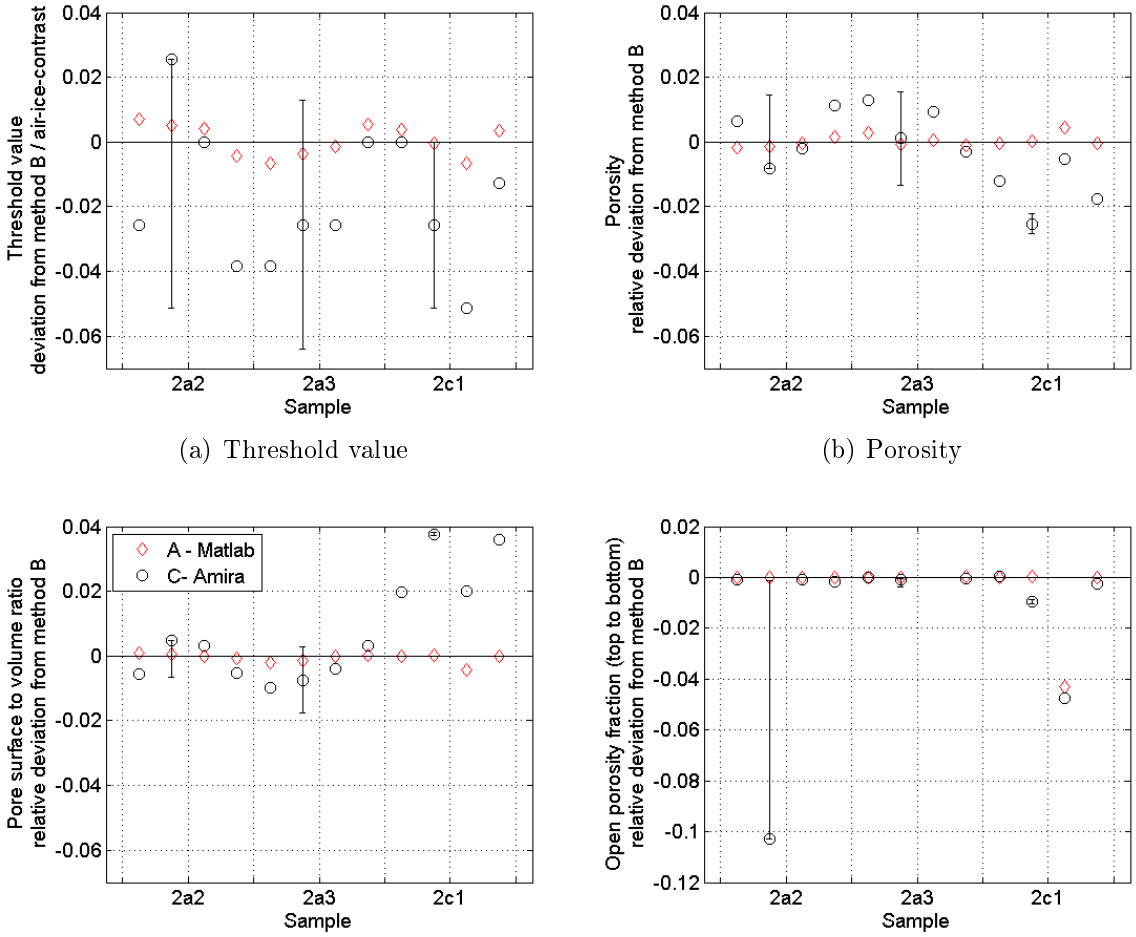

(a) Threshold value

(b) Porosity

(c) Pore surface to volume ratio

(d) Open porosity fraction

Figure 4.9: Comparison of the three segmentation methods, relative: Relative deviations of methods A and C from method B for the threshold value (relative to the air-ice contrast), porosity, pore surface to volume ratio and open porosity fraction for 3 samples with 4 stacks each. Note the different scale for the open porosity fraction. The black error bars show the results from the alternative thresholds for method C. The legend is valid for all graphs in this figure.

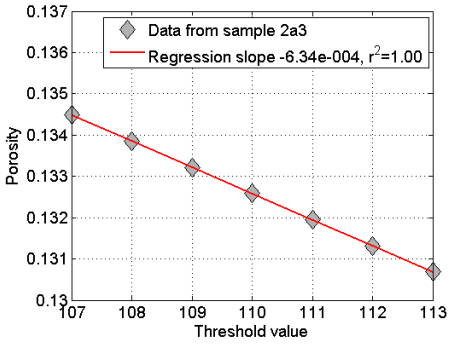

(a) Porosity vs threshold

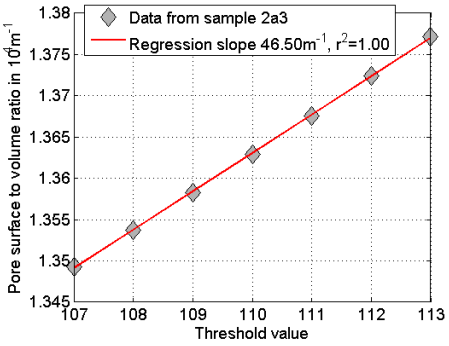

(b) Pore surface to volume ratio vs threshold

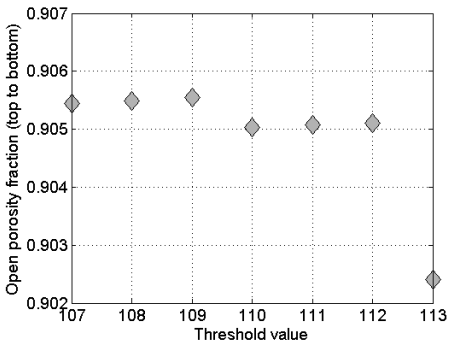

(c) Open porosity fraction vs threshold

Figure 4.10: Sensitivity of porosity, pore surface to volume ratio and open porosity fraction to threshold

- Objectivity: The threshold is set from the histogram following Otsu's algorithm. This is reproducible and not dependent on the person. Having tried manual thresholding, we found it difficult to chose a threshold in our images within a range of at least 5 (see figure 8(a)), and a difference of 5 can have an effect of 10% variation for the open porosity fraction. Salt segmentation is not possible using this method, because ice and salt peaks overlap in the histogram, but for permeability measurements this is not necessary.

- 3D threshold: Setting the threshold based on the whole stack uses more of the available information than a slicewise segmentation.

- Using as much of the sample as possible: in Matlab it is easy to select a large cylinder with a polygonal base as the total volume. Through this, one can use the most of the core and avoid the problem of pores near the boundaries being defined as exterior.

- Reproducibility: As many students and universities have Matlab available this method is reproducible.

From the comparison we conclude an uncertainty of less than $\pm 5\%$ for the threshold value, porosity and pore surface to volume ratio. The uncertainty of the open porosity fraction was larger, because of its dependency on the occurance of narrow channels. This could be tested for each sample by studying the connectivity again after removing channels smaller than a certain diameter.
Furthermore the same three samples 2a2, 2a3 and 2c1 were used to study the internal variability of porosity and pore surface to volume ratio. Figure 4.11 shows vertical variability, i.e. porosity and pore surface to volume ratio for each slice as well as for stacks and the whole sample, while figure 4.12 shows horizontal variability, i.e. porosities and surface to volume ratio were computed for four 4 sectors of each stack. The variations in porosity within a sample in the vertical were quite large (up to 0.15 within a stack), while surface to volume ratios vary less relatively in the vertical, with ranges of less than $0.5 \times 10^4 m^{-1}$. In the horizontal the variation was usually less (as expected with larger object size), with all stacks but one showing sector porosities within a range of about 0.05 and pore volume to surface ratios with all but two stacks within a range of $0.3 \times 10^4 m^{-1}$. Average relative deviations from the value for the whole sample were for the porosity in the vertical 29%, in the horizontal 25% and for the pore surface to volume ratio respectively 8 and 10%. As to the relationship between porosity and pore surface to volume ratio, figure 4.13 shows scatter plots for the slices of the three samples. There was a significant negative correlation between porosity and specific surface area of $r = -0.60$ and $r = -0.70$ for samples 2a2 and 2c1 respectively, while sample 2a3 did not have a significant correlation.

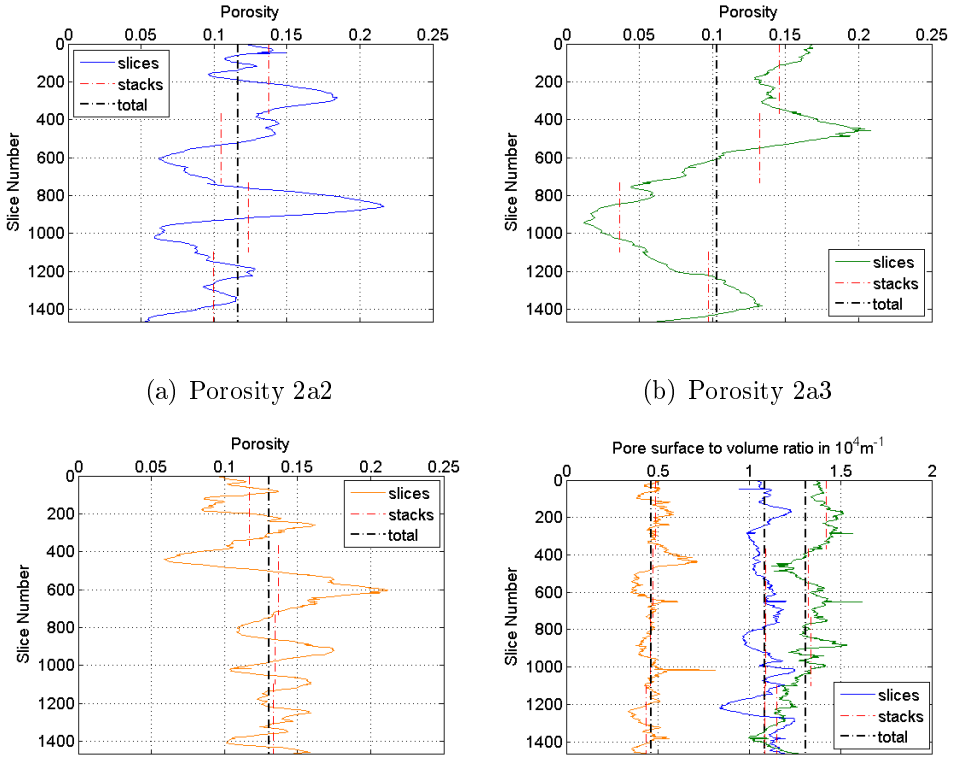

(a) Porosity 2a2 (b) Porosity 2a3

(c) Porosity 2c1 (d) Pore surface to volume ratio - all

Figure 4.11: Depth (slice number) vs porosity/pore surface to volume ratio for 3 samples - values for each slice, for stacks of 366 slices each and for the whole sample (total)

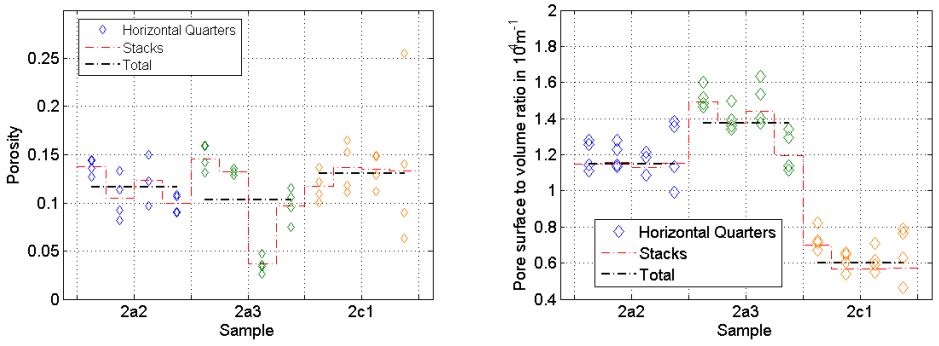

(a) Porosity (b) Pore surface to volume ratio

Figure 4.12: Porosity and pore surface to volume ratio for quarters of the 4 stacks of 3 samples, values for quarters of the stacks of 366 slices, for the stacks and for the whole sample (total)

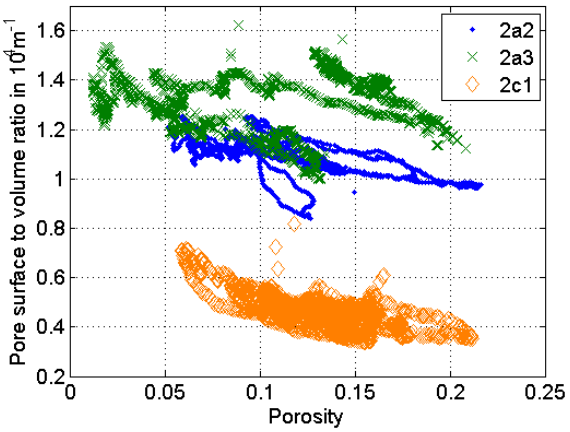

Figure 4.13: Scatter plot of pore surface to volume ratio vs porosity of the slices

4.2 Microstructure analysis

This section describes the microstructural features we used to characterize the ice and their derivation. This includes porosities, pore size distributions, length scales and tortuosities. Porosities describe the pore volume and to some extent its connectivity. Pore size distributions reflect all pores while the characteristic length scales summarize the information on pore sizes to one quantity. Tortuosities describe the sinuosity of the pore space.

Porosities

In order to give a good description of the samples, the porosity found in the SXRT images, the so-called imaged porosity, is not sufficient. We introduce two additional porosities, the effective and the total porosity, which are defined in the following and sketched in figure 4.14.

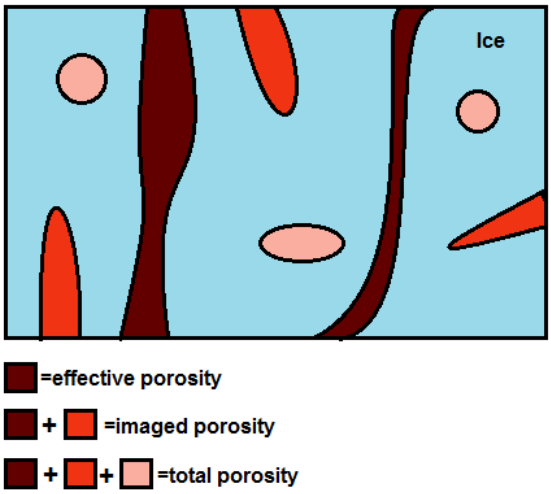

Figure 4.14: Schematic of the three porosities - effective, imaged and total

Imaged porosity ϕ_{im} This is the porosity found in the images after segmentation by voxel counts. Ideally there should not be isolated pores within the samples except for air bubbles.

Effective porosity ϕ_{eff} This is the part of the pore space that connects the two sides of the sample in the direction considered. It depends on the direction.

Total porosity ϕ_t This is the total porosity the ice had before centrifuging. It was found by combining the imaged porosity with a factor taking the residual salt into account. We assumed that the brine salinity was originally in equilibrium with the sample temperature $S_{be}(T)$, but that before and during centrifuging some pieces of fresh ice broke off and diluted the centrifuged brine to its salinity $S_b < S_{be}$. With the measured diluted mass of the brine m_b and the original mass of the brine $m_{be} = m_b \frac{S_b}{S_{be}}$ and the mass of the broken off ice $m_{bi} = m_b e(\frac{S_{be}}{S_b} - 1)$ the porosities of the removable brine

ϕ_b and the residual ice ϕ_i and their sum ϕ_t were calculated as follows:

$$\phi_b = \frac{V_b}{V_t} = \frac{m_{be}}{\rho(S_{be})} \left(\frac{m_{be}}{\rho(S_{be})} + \frac{m_i}{\rho(T, S_i)} + \frac{m_{bi}}{\rho_{bi}} \right)^{-1} \tag{4.1}$$

$$\phi_i = \frac{V_r}{V_t} = \frac{V_r}{V_i} \frac{V_i}{V_t} = \phi(T, S_i)(1 - \phi_b) \tag{4.2}$$

$$\phi_t = \frac{V_b + V_r}{V_t} = \phi_b + \phi_i = \phi_b(1 + \frac{\phi_i}{\phi_b}) \tag{4.3}$$

V refers to volume, S to salinity, m to mass, ρ to density and the indeces b,i,r, and t to removable brine, ice, residual brine in the ice and total, respectively and be and bi to brine before dilution and the fresh ice that diluted the brine. Liquidus density $\rho(S_{be})$, ice density $\rho(T, S_i)$ and ice porosity $\phi(T, S_i)$ are functions of temperature and salinity from Maus (2007) after Cox and Weeks (1983). Pure ice density is $\rho_{bi} = 917 \frac{kg}{m^3}$. The total porosity was thus derived from the imaged porosity of a sample by $\phi_t = (1 + \frac{\phi_i}{\phi_b})\phi_{im}$.
The dilution assumption was verified by comparing the removable brine porosities ϕ_b to the imaged porosities of the samples. Using a t-test it was verified that they do not come from distributions with significantly different means ($p = 0.29$). The mean of the removable brine porosities in the field was 0.103, while the mean of the imaged porosities was 0.086.

Pore size distributions

In order to fully describe the pore space, we obtained both 3D pore radius and 2D pore area distributions.
The pore radius distribution was found using the software GeoDict (ITWM, 2009) with two methods - a mercury intrusion porosimetry (MIP) simulation and a geometric method. Both describe the minor axis of ellipsoidal pores and give volume fractions for each radius. As mentioned in section 2.5 in MIP mercury is pressed into the samples. The relationship between applied pressure and adsorbed volume is related to the radius of the pores which are reached by the mercury. The thus derived pore size distribution does not include all pores but only the ones connected to the boundaries. Problems with MIP are the assumptions made about cylindrical pore geometry and the bottleneck effect when deriving pore size distributions. This effect describes the fact that large pores behind small necks are classified as small pores. This leads to an overestimation of the amount of small pores and an underestimation of large pores (Moro and Böhni, 2002). MIP is simulated in GeoDict morphologically with erosion and dilation of the pore space. First it is eroded with a sphere of a certain radius, then the part disconnected from the boundaries is removed and the remaining part dilated again. This gives the pore space that is reached by a sphere of radius R_{MIP} flowing in from the boundary (Wiegmann and Becker, 2007). This algorithm has also been used by Hilpert and Miller (2001) and Arns et al. (2005). We found the MIP pore size distribution with inflow from both boundary planes perpendicular to the flow direction.
The geometrical pore size distribution includes all pores and is based on spheres placed into the pores. If a point is inside any sphere with radius R_{test} which fits into the pore

then it is part of a pore with a radius R_{geo} larger than R_{test}.
In addition pore areas were measured in each horizontal section using Matlab's function *regionprops* in order to incorporate the entire pores rather than just the smallest dimention of the pores. Pores within a certain size interval were counted, such that pore area distributions give number fractions for each size.
Both the cumulative geometrical pore size distributions and the cumulative pore area distributions were fitted to different distributions with the maximum likelihood method (Emery and Thomson, 2004). To determine which distribution is most appropiate we used the negative log likelihood (*lognlike*, *gamlike*). The distributions that fitted best were the gamma and lognormal distribution and those were the ones used for all samples. The lognormal probability density functon is given by

$$f(x) = \frac{1}{x\sigma\sqrt{2\pi}} e^{-\frac{(lnx-\mu)^2}{2\sigma^2}} \text{ for } x > 0 \tag{4.4}$$

with the mean μ and standard deviation σ of the logarithm of x. The geometric mean of x is thus $\exp\mu$. This distribution has been found to fit sea ice pore size distributions well (Perovich and Gow, 1996). The gamma probability density function is given by

$$f(x) = \frac{x^{\alpha-1}e^{-x/\theta}}{\theta^{\alpha}\Gamma(\alpha)} \text{ for } \alpha, \theta > 0;\ 0 \leq x \leq \infty \text{ and } 0 \text{ elsewhere} \tag{4.5}$$

with the gamma function $\Gamma(\alpha) = \int_0^\infty x^{\alpha-1}e^{-x}dx$ and the scale parameter θ and the shape parameter α. The mean of x is $\alpha\theta$. Both the exponential and the Chi-square distribution are special cases of the gamma distribution ($\alpha = 1$ and $\theta = 2$ respectively). Gamma distributions have been used to describe rain drop sizes (Li et al., 1994), snow grain sizes (Nakamura et al., 2001), pore sizes in filter media (Johnston, 1998) and rain rates (Cho et al., 2004).

Characteristic pore scales

When predicting the permeability, characteristic pore scales play an important role (section 2). We focused on the following length scales and tried to quantify their relevance with respect to the permeability:

- the ratio of pore volume to pore surface area ϕ_{im}/s, with s the specific surface area from the software GeoDict (ITWM (2009)). The algorithm in GeoDict approximates the surface area by statistical methods. It gives correct results for spherical geometry, but is biased for highly anisotropic media.
- the median of the geometric pore radius distribution, med(R)
- the mean (number average) of major and minor axis lengths l_{maj} and l_{min} of ellipses that have the same second central moments as the pores in the slices perpendicular to the flow direction (*regionprops*)
- the critical length scale l_c
- a scale from the two-point correlation function l_{tp}

. The latter two deserve more explanation.

Critical pore size l_c The critical length scale l_c is given by the maximum diameter of a sphere that can pass through the medium. This is implemented in GeoDict in the function *Percolation path*. One would expect this to coincide with the maximum of the MIP pore size distribution i.e. the inflection point of the cumulative curve (as discussed in 2.5). In our samples it was found that this was the case for columnar, but not for granular structures (figure 4.15).

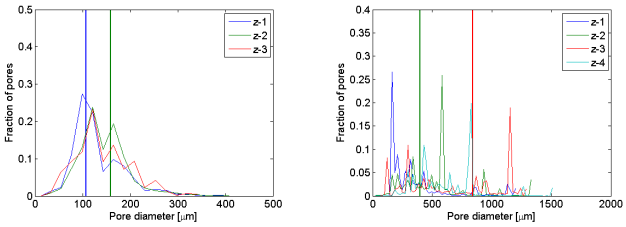

(a) 1a3l (b) 2c1

Figure 4.15: Pore size distributions from MIP simulation and l_c (vertical lines) for the 3 cells of the columnar samples 1a3l and 4 cells of the granular sample 2c1

Two-point correlation function The length scale l_{tp} is defined in Berryman and Blair (1987) as the crossing point of a linear approximation to the isotropic two-point correlation function $S_2(R)$ for small R with the $lim_{R\to\infty}S_2(R) = \phi^2$. It provides an estimate of the average pore diameter (Blair et al., 1996). The algorithm for finding $S_2(R)$ is described in Berryman (1985). Fast Fourier Transforms were used to produce 2D autocorrelation images, for one slice from each sample. This slice was chosen as the first one having the same porosity as the whole sample. Averaging the autocorrelation function over all directions gives the isotropic two-point correlation functions. From autocorrelation plots like 4.16(a) and (b) anisotropy can be seen. Since samples with a significant horizontal anisotropy were turned so that one axis was aligned with the preferred direction, one can estimate an anisotropy factor from the two-point correlation function for the two coordinate directions. Figures 4.16(c) and (d) shows the two-point correlation functions for these cells including both the isotropic one and the one for the x and y direction. One can see that the estimate of l_{tp} that is given from the crossing points of the linear approximations with the horizontal line at $S_2(R) = \phi^2$ varies significantly between the x and y direction for figure 4.16(c), but almost not at all for figure 4.16(d).

Tortuosities

Often porosities and length scales are not enough to characterize porous media with respect to flow processes. Many permeability models therefore include tortuosities. We calculated both an estimate of hydraulic and electrical tortuosity.

Hydraulic tortuosity τ_h The hydraulic tortuosity is estimated by the ratio of the length of the shortest path that the largest sphere can take to percolate through the pore

space (in GeoDict: *Percolation path*) and the length of the sample. This means instead of being an average value for all pores, our τ_h describes only the largest channel.

Electrical tortuosity τ_e The electrical tortuosity is calculated by the method described in Katz and Thompson (1987). It is based on the cumulative MIP pore size distributions and the critical length scale l_c from GeoDict and was computed with Matlab. The fraction of the pore space larger or equal to the critical length scale l_c was subtracted from the intrusion volumes V at all diameters l_d smaller than l_c. This volume V_c was then used in a trial solution for the electrical conductance $g_e \propto V_c l_d$ which was maximized. The diameter at which g_e was largest l_e^{max} was used to derive the formation factor $1/F = \frac{l_e^{max}}{l_c}\phi V_c(l_e^{max})$ which in turn is related to the electrical tortuosity by $\tau_e = \sqrt{F\phi}$.

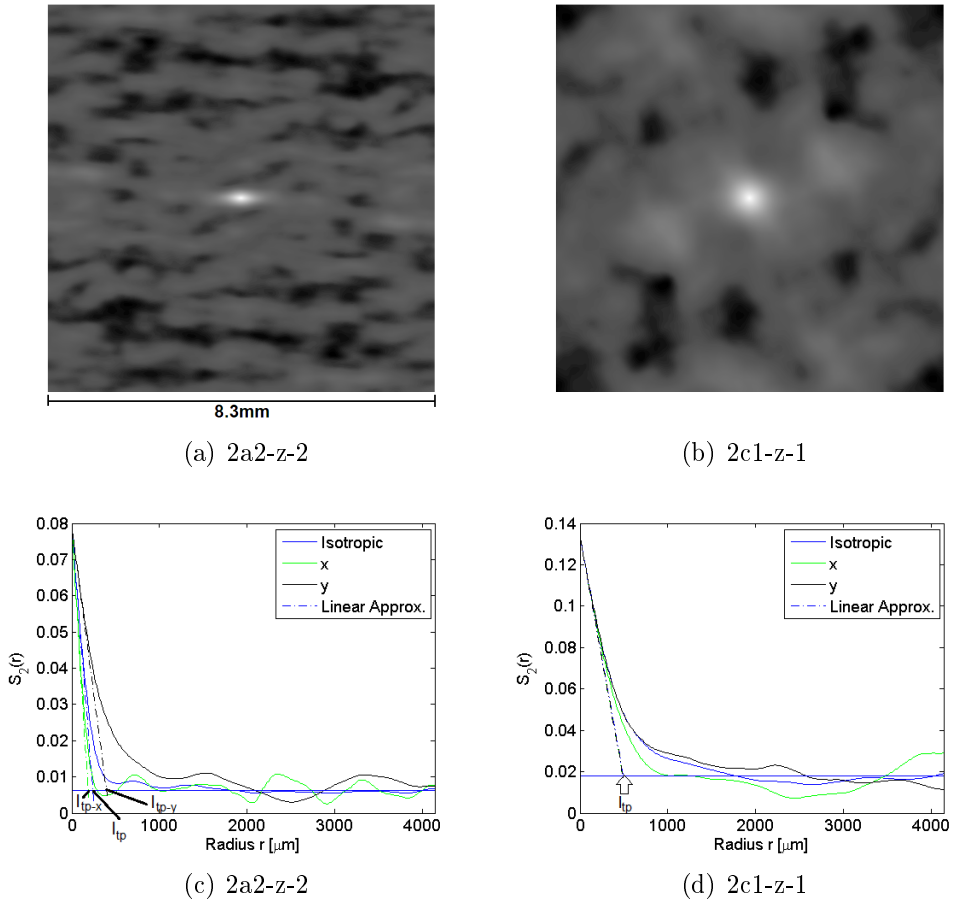

(a) 2a2-z-2 (b) 2c1-z-1

(c) 2a2-z-2 (d) 2c1-z-1

Figure 4.16: 2D autocorrelation plots (a and b) and isotropic two-point correlation function $S_2(r)$ as well as the two-point correlation functions in x and y direction for two cells with approximations that give l_{tp} and l_{tp-x} and l_{tp-y} (c and d). The horizontal line is at $S_2(r) = \phi^2$. In (a) and (b) white means high correlation and black low correlation. The colours have been changed a little to make the difference between small and no correlation visible in the print version. (a) and (c) show an anisotropic and (b) and (d) an isotropic cell.

4.3 Lattice Boltzmann modelling

To attain values for the permeability, numerical simulation of fluid flow through the pore space was performed using a lattice Boltzmann method (LBM). LBM is based on mesoscopical movement of single-point distribution functions that propagate and collide on a discrete lattice, resulting in a solution of the Navier-Stokes equations. A short description of the method follows, for detail refer to the literature (Sukop and Thorne, 2007; Wolf-Gladrow, 2005). We used the commercially available software GeoDict developed by the Fraunhofer Institut für Techno- und Wirtschaftsmathematik(ITWM, ITWM (2009)). The parallelized LBM solver called ParPac included in this software works on a D3Q15 lattice. This means it has 3 dimensions and 15 velocities and particle distributions - one for the center, 6 for the Cartesian axes and 8 to the voxels that share a corner (figure 4.17).

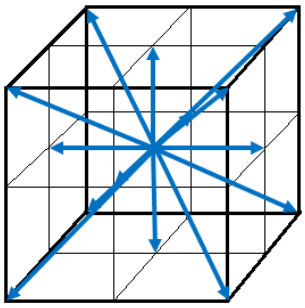

Figure 4.17: D3Q15 lattice

The equation to be solved for each velocity and particle distribution is the multiple-relaxation-time lattice Boltzmann equation:

$$f_i(\vec{x} + \Delta t\vec{e}_i, t + \Delta t) = f_i(\vec{x}, t) - \sum_j \Lambda_{ij}(f_j(\vec{x}, t) - f_j^{eq}(\vec{x}, t)) \tag{4.6}$$

where f_i refers to the particle distribution function, $\vec{e}_i$ are the lattice velocities and Λ is the collision or relaxation matrix. The kinematic viscosity is related to the relaxation matrix through a relaxation parameter τ which was set to 1. The equilibrium distributions f_j^{eq} are appropriate functions of the conserved moments such as density and momentum. Macroscopic density and velocity are: $\rho = \sum f_i$ and $\vec{v_f} = 1/\rho \sum f_i \vec{e}_i$. By linearizing the equilibrium distributions, the model solves the Stokes equation rather than the Navier-Stokes equations (Manwart et al., 2002). The permeability matrix is then calculated from the mean velocity in each direction and the corresponding pressure drop.
For more information on multiple relaxation time models refer to Premnath and Abraham (2007).
Two major advantages of LBM over direct solvers of the Navier-Stokes equations are the treatment of complex boundaries and the possibility of parallelization due to local data communication (Yu et al., 2003). LBM requires more memory than Navier-Stokes solvers because all distribution functions have to be stored, yet can converge faster in complicated geometries.
The model was run on two servers at the Johannes Gutenberg University in Mainz (table 4.3).

Table 4.3: Information about the servers

Server 1	Server 2
Dell PowerEdge Server	SunFire X4440
4 Intel Xeon processors	8 AMD Opteron processores
=8 cores	=16 cores
64 GB RAM	64 GB RAM
SMP server	SMP server
SuSE Enterprise Linux	SuSE Enterprise Linux
	HPC cluster connection with InfiniBand
	MPICH-1/-2 parallelization

Model Input

As input for the fluid values brine of -5°C with a salinity of 85.5 was used: kinematic viscosity $\nu = 2.2\ 10^{-6} \frac{m^2}{s}$ and density $1070 \frac{kg}{m^3}$ (from relationships from Maus (2007)). As discussed in section 2.1 the viscosity should not play a role for the permeability value if the process is in Darcy's regime, i.e. the Reynolds number $Re = \rho v_f d/\eta$ is smaller than 1. To relate this to brine channel sizes we started at the model of a circular pipe which gives a permeability of $k = R^2/8$ (see equation 2.6) for a tube of radius R_i. Plugging this into Darcy's law in one dimension gives $v_f \phi = -R^2/(8\eta) dp/dz$. Taking $d = 2R$ and rearranging results in

$$Re = \frac{\rho v_f 2R}{\eta} = \frac{\rho (2R)^3}{32\phi\eta^2} \frac{dp}{dz} \leq 1. \tag{4.7}$$

Assuming a pipe of a diameter $R = 0.5mm$ which was on the high end of our pore size distributions and a porosity of 25% this would allow for a pressure gradient of $43Pa/m$. For a pipe of diameter $R = 0.05mm$ the pressure gradient limit is $43\ 10^3 Pa/m$. Are these values you would expect to occur in our sea ice?
Pressure gradients in non-melting sea ice can be a result of several things:

(a) parts of the sea ice being lifted to above the water surface (freeboard)

(b) density gradients within the brine

(c) a snow load depressing the ice below the sea surface

For (a): The freeboard of floating ice (without snow) of thickness H due to buoyancy is $f = (\rho_w - \rho_i)/\rho_w H$ (Petrich and Eicken, 2010) with sea water density ρ_w and bulk ice density ρ_i. The brine of density ρ_b in the freeboard is not necessarily in a force balance and presses down on the draft $(H - f)$ with a pressure $p = fg\rho_b$. Approximating brine density with sea water density ρ_w and draft with total ice thickness gives $p \approx (\rho_w - \rho_i) gH$ and a gradient $\Delta p/\Delta z \approx (\rho_w - \rho_i) g$. With a water density of $1027 kg/m^3$ and an ice density of $930 kg/m^3$ this gives a pressure gradient of $950 Pa/m$. This pressure gradient will force the brine out of the freeboard if its permeability allows it to. Waves can push new sea water or brine up through the ice into the freeboard.
For (b): pressure gradients can be a result of density gradients within the brine. In our case measured brine salinities did not exceed 80psu and where mostly around 40psu. The

brine density depends on its salinity $\rho_b = 1000 + 0.8\ S_b$ (Petrich and Eicken, 2010). The sea water under the ice had salinities around 34.3 psu. A typical pressure gradient ($(\rho_b - \rho_w)g$) would then be on the order of $100 Pa/m$. Since this is an unstable stratification, convection would take place. Convection would probably start before a large pressure gradient is reached and reduce the density and therefore the pressure gradient.
For (c): flooding due to a snow load can only occur when the freeboard $f = (\rho_w - \rho_i)/\rho_w H - h_s\rho_s/\rho_w$ is negative. This means the snow of density ρ_s has to have a thickness $h_s \geq H(\rho_w - \rho_i)/\rho_s$ (Petrich and Eicken, 2010). This situation is similar to the bail test and gives a pressure gradient of $\Delta p/\Delta z = g\rho_w f/H$. In our case snow thicknesses were between 4 and 5cm and ice thicknesses between 13 and 14 cm. With an approximate snow density of $300 kg/m^3$ this gives a freeboard between +2 and -2mm. The slightly negative freeboard may result in a negative pressure gradient of $170 Pa/m$. The slightly positive freeboard which could be larger with lower snow densities possible for new snow leads us back to situation (a).
This means both situations (b) and (c) would yield maximum pressure gradients on the order of $100 Pa/m$ for our ice, while (a) could give values on the order of $1000 Pa/m$, but is not valid, because we had a snow cover and almost no positive freeboard. Consequently we used two pressure gradients of 10 and $100 Pa/m$ in our model and compared the permabilities to ensure that the flow is in the Darcy regime.

Modelled sample size and resolution

An important limitation for LBM applications is computer memory. Modelling of Stokes flow with LBM as done here can take up to 19 times more memory than with a finite differences scheme also implemented in GeoDict. Convergence is however reached much faster (personal correspondence F. Enzmann, 2010). Therefore sample size and resolution have to be chosen carefully. The sample size should be representative for the sea ice the sample is taken from, i.e. large compared to some characteristic length scale. For some of our samples, the columnar ones, this is possible while for the non-columnar ones, pore diameters can be large. Also the distance between larger pores is often larger and for the permeability calculations it will make a major difference if a channel is fully or partly in the sample or not. However, this is a problem inherent in this method, when taking such high resolution images and will be discussed in section 6. The resolution should be good enough to resolve all channels with a sufficient number of voxels. Good agreement with analytical solutions has been found for channels as small as 5 voxels wide (Sukop and Thorne, 2007). Typical pore sizes in sea ice are 0.2-0.3mm (Eicken et al., 2000; Perovich and Gow, 1996), which gives minimum resolutions of $40 \mu m$. Necks that are even smaller might exist which would make better resolution necessary.
Another limitation we became aware of was that even though the porosity was around 10% there was not necessarily a connection from top to bottom in a sample. Since the brine was centrifuged out of the pore space the sample must have been permeable in some direction (unless we are dealing with air bubbles). This will be discussed further in section 6.
As a consequence of these problems and limitations we made calculations for two domain sizes: the whole samples and cells within them (figure 4.18). Vertical flow through the samples was modelled at a resolution of $35 \mu m$ (resampled with the Lanczos resampling method

(Duchon, 1979) in Amira). To be able to use a higher resolution, obtain larger variabilities in porosity and permeability and have even boundaries in x and y direction to model flow in those directions as well, smaller cells within the samples were chosen for modelling. These were modelled at a resolution of $22\mu m$[1] . Because of the connectivity problems mentioned above they were chosen to be shorter in the flow direction than perpendicular to it and became 8.29x8.29x4.12mm^3 in size (377x377x189 voxels). Thus each sample was divided into two $(8.29mm)^3$ blocks vertically that were divided into two cells in each of the three directions as in figure 4.18. In two samples it was not possible to fit a $(8.29mm)^2$ square horizontally, then the largest possible square was used (2a3: $(7.34mm)^2$, 2a4: $(8.05mm)^2$). Modelled sample sizes in voxels and number of cells per sample are stated in table 4.1. In order to reduce computation time only the effective porosity was included in the LBM. Each of these cells used about 9GB of computer memory depending on the porosity.

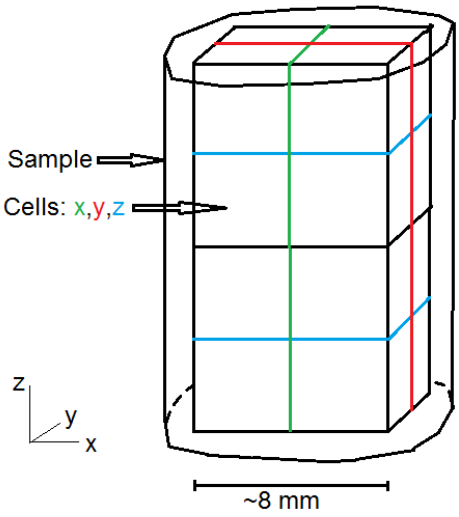

Figure 4.18: Sketch of how the cells for calculations of permeability in the three coordinate directions were chosen

Boundary conditions and convergence criteria

There is always uncertainty associated with modelling fluid flow. Boundary conditions (Zhang and Kwok, 2006) and criteria for numerical convergence are still under discussion. Within the scope of this work, we were not able to take into account all the newest developments, but used the ones that are implemented in the ParPac LBM solver of GeoDict. The boundary conditions were: bounceback at pore and domain walls perpendicular to the

[1] The cells of sample 2a4 were by mistake resampled to $23.68\mu m$ resolution and then modelled with LBM as if they were $22\mu m$. The effect of this was estimated by modelling two cells at the correct resolution of $23.68\mu m$. The permeabilities of the other cells were then scaled by the factor $(23.68/22)^2 = 1.16$ to correct for the effect of the wrong model resolution.

flow direction, pressure boundary conditions realized through a body force (Manwart et al., 2002) and periodicity in fluid flow direction. This last boundary condition is somewhat troublesome with low porosities as we have them. This will be investigated and discussed closer in section 5.3.
As a convergence criterion we used an accuracy of 10^{-4} for the relative change of the permeability in 100 iteration steps or a maximum iteration of 10000 iterations.

5 Results

5.1 Microstructure analysis

In this section results from microstructure analysis are described in the same order as in the methodological section, i.e. porosities, pore size distribution, length scales and tortuosities.

Porosities

Total porosities of the ice ranged from close to 0 to 36% and effective porosities from 0 to 20%. The relationship between effective and total porosity depended on ice type and direction. In figure 5.1(a) effective porosities are displayed with respect to total porosities for non-columnar ice and for columnar ice with flow into x and yz direction. Only for the yz-direction of columnar ice there was a good agreement with a linear relationship (see figure 5.1(b)). The 95% confidence interval (CI) for the intercept with the x-axis (ϕ_c) was 0-12%. Porosity profiles based on samples 2c1, 2a2, 2a3 and 2a4 are shown in figure 5.2. Field values are based on centrifuged brine mass and measured salinities (see section 4.2). Both imaged and total porosity have a C-shaped profile, while the effective porosity increases with depth.

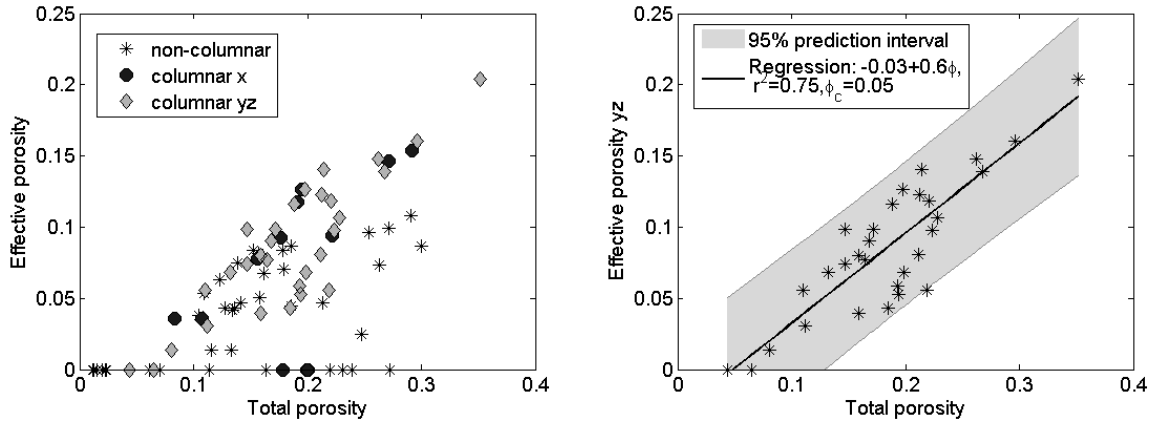

Figure 5.1: Relationship between effective and total porosities (a) for all ice types, (b) for columnar samples in yz direction, regression with explained variance r^2

Pore size distributions

All of the columnar samples had narrow pore radius distributions with the major part of radii below 0.25mm (see figure 5.3). Note that radius distributions describe the minor axis of the pores. The non-columnar samples all had broader distributions, but exhibited variable characteristics otherwise. 2c1 had a very broad spectrum with some large pores with ca. 0.75mm radius. 4c1 had a mixed structure - a part is columnar, but there is also a large pore (0.9mm). 1b1 had a distribution which is quite similar to the columnar samples, but its total porosity was smaller. The pore radii distributions were fitted about equally

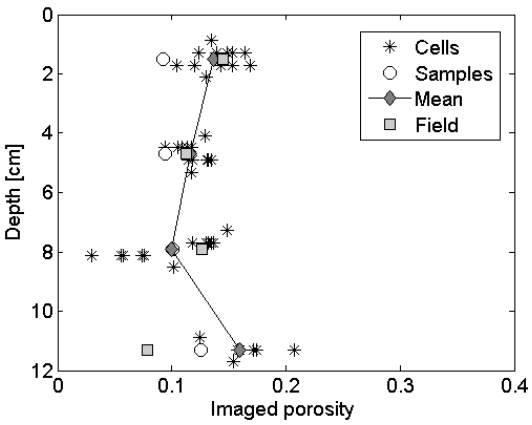

(a) imaged porosity

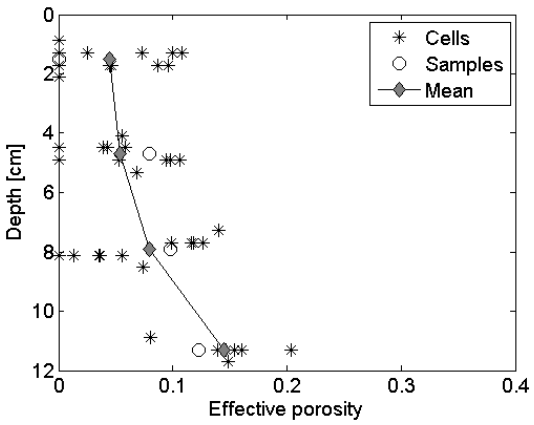

(b) effective porosity

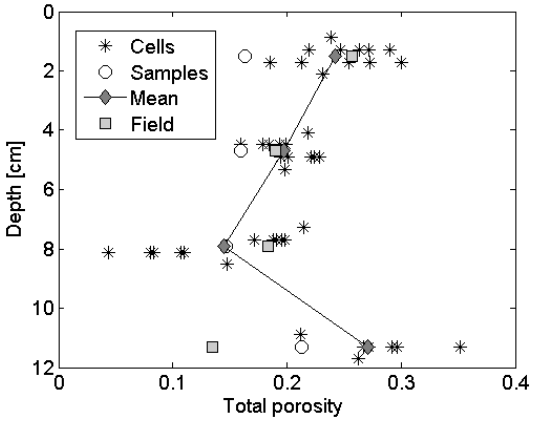

(c) total porosity

Figure 5.2: Vertical profiles of imaged, effective and total porosity from samples 2c1, 2a2, 2a3 and 2a4 - includes both values from the cells and the whole samples where applicable and their means as well as field values of imaged and total porosities

well by both lognormal and gamma distributions. The distribution peaks were generally underestimated.
All pore area distributions (see figure 5.4) had a local maximum at the smallest possible area resolved ($(11.84\mu m)^2$), which contains all pores smaller than 1 voxel. The columnar samples looked very much alike both in shape and width and had their maximum at ca. $0.1mm^2$. Both sample 4c1 and 1b1 looked similar to the columnar samples except for a smaller peak at the smallest area and some large pores for 4c1. 2c1 had a completely different pore size distribution, with two peaks, one at 0.001 and one at $0.3mm^2$. For all of the columnar samples the gamma distribution fitted the data better. However in the middle of the distribution the deviations were large because there was a minimum at $0.002 - 0.003mm^2$. The non-columnar samples 1b1 and 4c1 were fitted better by the lognormal distribution, while the two-peak granular sample 2c1 is described by neither lognormal nor gamma distribution.

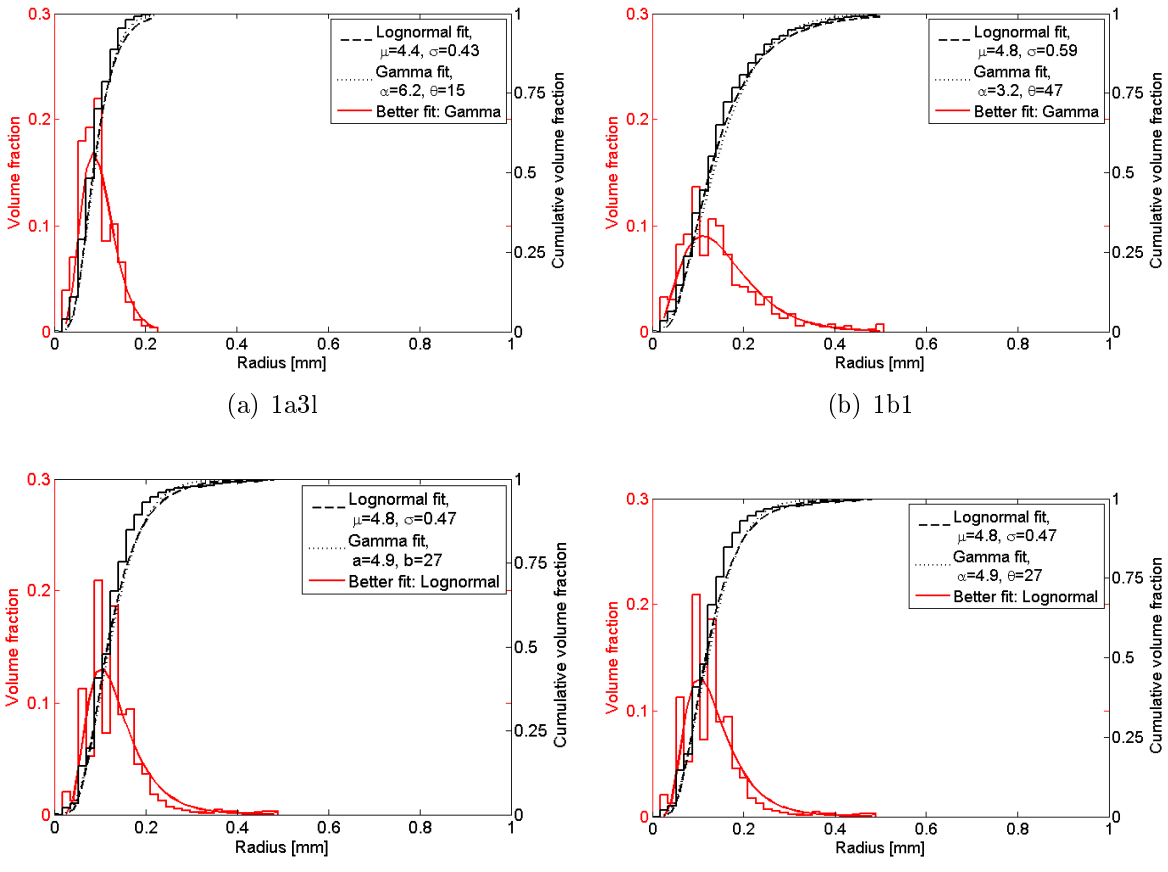

(a) 1a3l (b) 1b1

(c) 2a2 (d) 2a3

Figure 5.3: Volume fractions and cumulative volume fractions of radii [mm] with lognormal and gamma distribution fits for the 7 samples

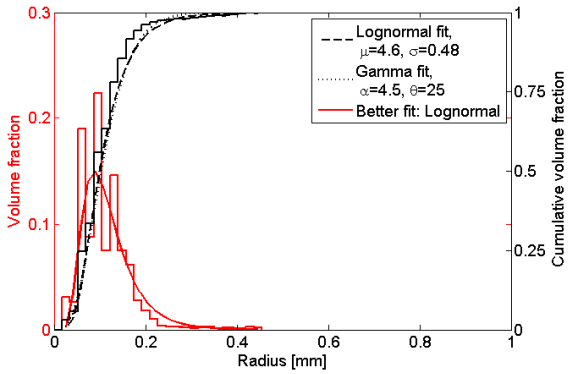

(e) 2a4

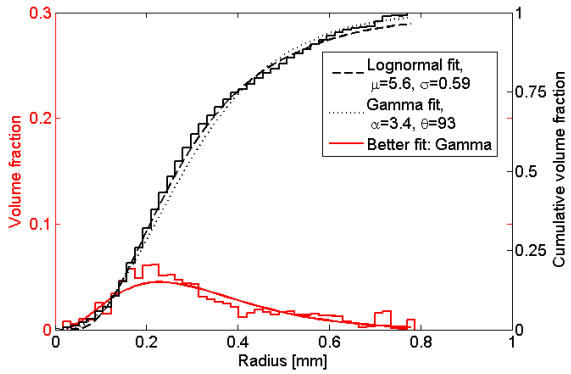

(f) 2c1

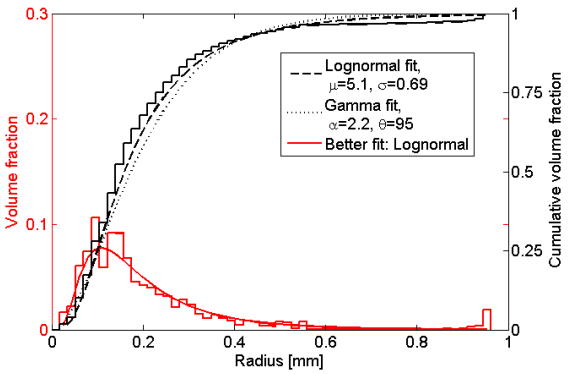

(g) 4c1

Figure 5.3: (continued)

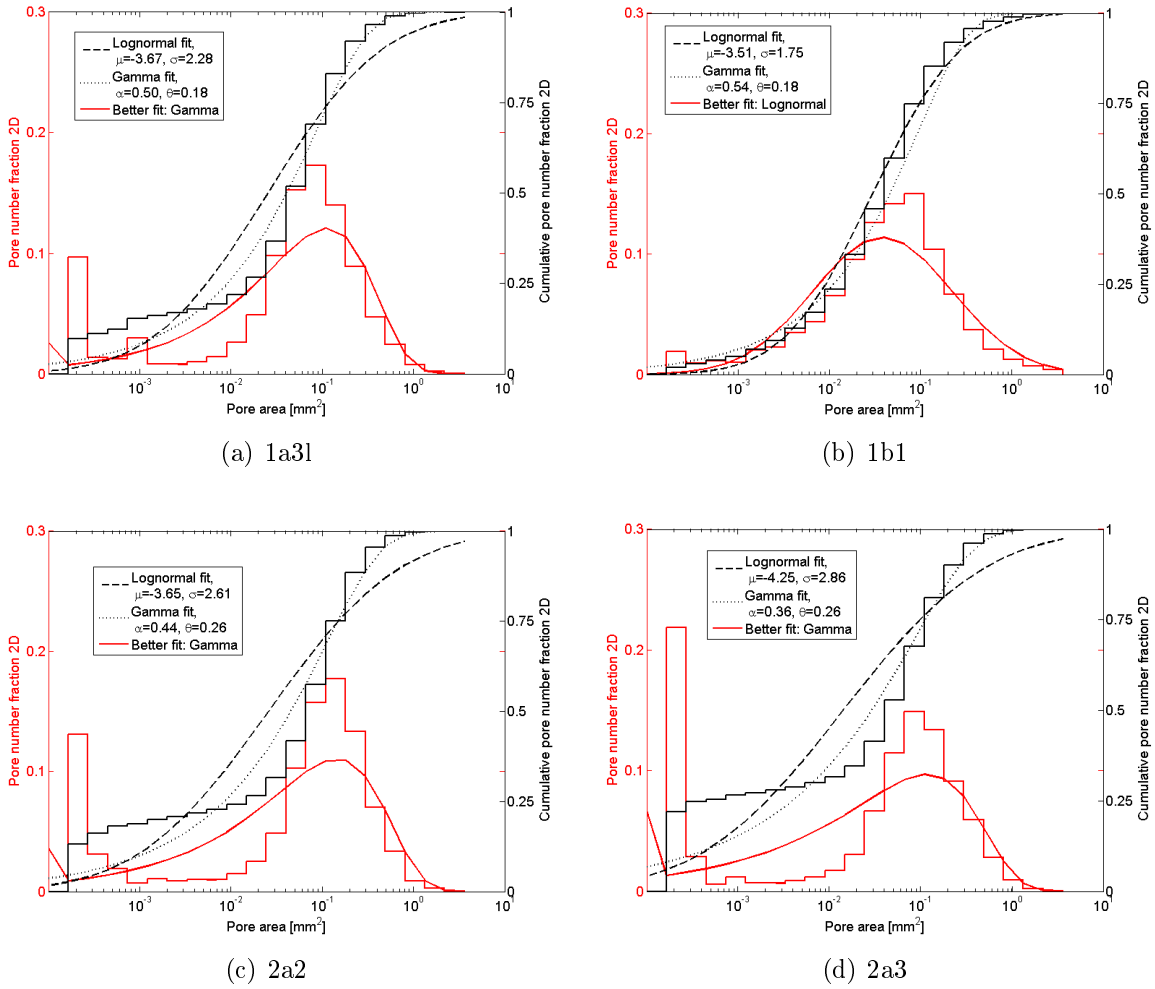

(a) 1a3l (b) 1b1

(c) 2a2 (d) 2a3

Figure 5.4: Pore number fractions and cumulative pore number fractions of pore area $[mm^2]$ with lognormal and gamma distribution fits for the 7 samples

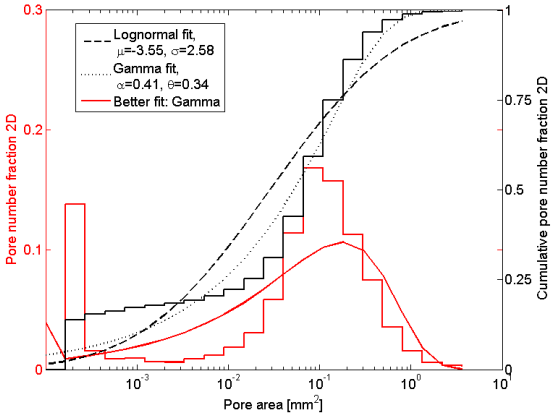

(e) 2a4

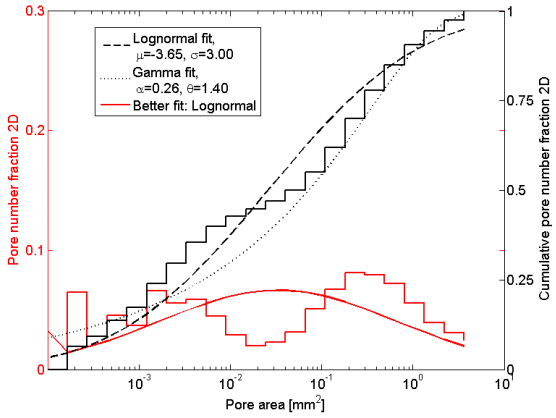

(f) 2c1

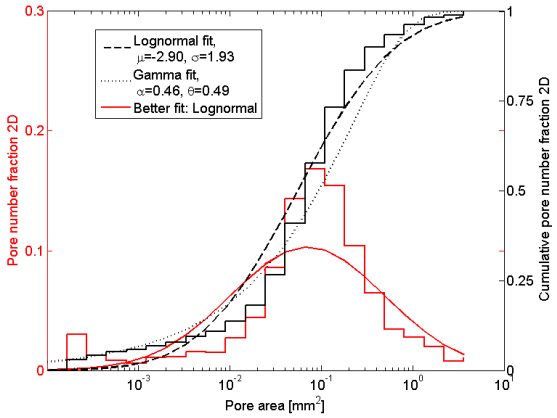

(g) 4c1

Figure 5.4: (continued)

Characteristic pore scales and anisotropy

Characteristic pore scales The different structure of columnar and non-columnar ice was also reflected in the characteristic pore scales. Contrary to the non-columnar ice the columar ice exhibited a strong direction dependence which is indicated by length scales like major and minor axis lengths of fitted ellipses, and the two-point correlation length scale with its extremes (figure 5.5). Except for l_{maj} and l_{tp_z} the pores of the columnar samples were smaller than 0.4mm, while pores of the non-columnar ice ranged up 1mm in size (figures 5.5 and 5.6). The length scale distributions of non-columnar ice had a larger range than those of columnar ice. The figures show twice the median and four times the pore volume to surface ratio to compare all length scales as typical diameters.
Correlations of length scales and porosities were calculated separately for non-columnar ice and for x and y-z direction of the columnar ice, because the y and z direction displayed very similar behaviour with respect to the direction dependent quantities (l_c, l_{tp}, permeabilities). The results are shown in tables 5.1 and 5.2. Since there were only 12 observations in x direction in the columnar ice, one cannot consider these results statistically reliable. There were only few significant correlations in x direction and none of the length scales correlated with all three porosities. For the y and z direction in columnar ice there were many more significant correlations. Both l_c, l_{maj} and l_{min} had a significant correlation with all three porosities and linear regressions were done of the non-zero l_c, l_{min} and l_{maj} in yz-direction on total porosity (figure 5.7). The estimates of the slopes were $0.25mm$, $0.37mm$ and $2.53mm$. The other three length scales in figure 5.7 were fairly constant throughout the porosity range. The non-columnar ice did in general show much stronger correlations of length scales with each other and porosities than the columnar ice. All six length scales had a strong dependency on porosity, which is displayed in figure 5.8. Estimates of the slopes of the linear regressions were $2.34mm$, $1.11mm$, $1.89mm$, $0.94mm$, $1.48mm$ and $0.51mm$ for l_c, l_{min}, l_{maj}, med(R), l_{tp} and ϕ_{im}/s respectively. Thus for non-columnar ice there were stronger dependencies of length scales on porosity than for columnar ice for all but l_{maj}. Both for columnar and non-columnar ice the median of the geometric pore size distributions and the pore volume to surface ratio were highly correlated.

Anisotropy and aspect ratios The columnar samples had a preferred orientation of elliptic pores in the horizontal. Therefore both the ratio of major to minor axis lengths (aspect ratio) and the ratio of the two two-point correlation length scales gave measures of the anisotropy (figure 5.9). The pores were largest in z direction and smallest in x direction. The average anisotropy between z and y direction was 1.6 and 2.5 for the two-point correlation and ellipse axis estimates respectively, between z and x direction it was 3.1 and 4.7 and between y and x direction 1.8 and 3.0. Anisotropy factors derived by ellipse axes were thus about 50% larger than by two-point correlation. Anisotropy factors and porosity were correlated (figure 5.10). Anisotropy between vertical and horizontal perpendicular to the layers (z-x) and horizontal parallel and perpendicular to the layers (y-x) increased with the total porosity. This increase was stronger for the vertical direction. No significant correlation was found for the z-y anisotropy.
The non-columnar samples did not show a preferred orientation of elliptic pore and did thus not have a macroscopic anisotropy. The aspect ratio of the mean pores (l_{maj}/l_{min})

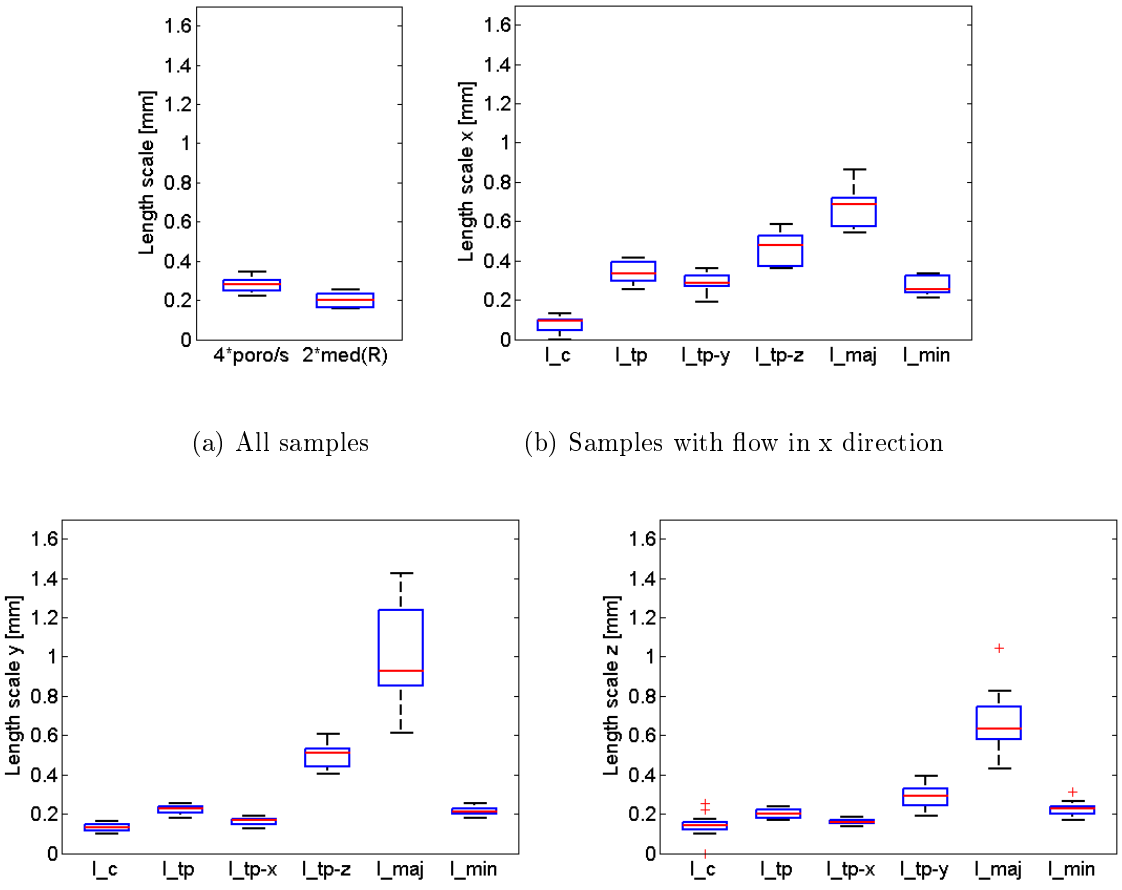

(a) All samples

(b) Samples with flow in x direction

(c) Samples with flow in y direction

(d) Samples with flow in z direction

Figure 5.5: Length scales of the columnar samples: (a) length scales non-dependant on direction - four times pore volume to surface ratio $4poro/s = 4\phi_{im}/s$, twice the median of the geometric pore size distributions 2med(R), (b)-(d) direction dependent length scales: critical length scale l_c, two-point correlation length l_{tp}, l_{tp} for the two extreme directions perpendicular to the flow direction, mean major l_{maj} and minor l_{min} axes of ellipses fitted in the plane perpendicular to the flow direction

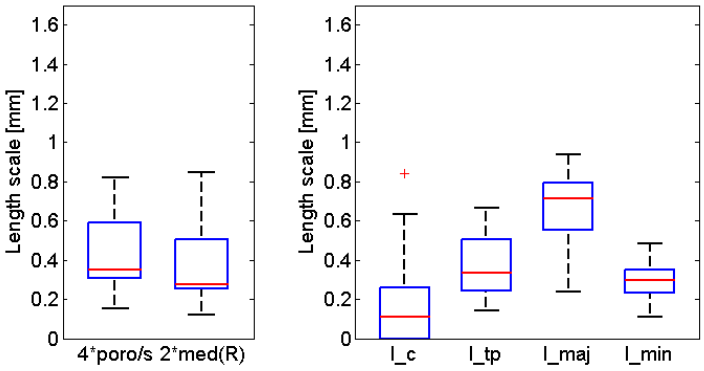

(a) (b)

Figure 5.6: Length scales of the non-columnar samples: (a) length scales non-dependant on direction - four times pore volume to surface ratio $4poro/s = 4\phi_{im}/s$, twice the median of the geometric pore size distributions 2med(R), (b)critical length scale l_c, two-point correlation length l_{tp}, mean major l_{maj} and minor l_{min} axes of ellipses fitted in the plane perpendicular to the flow direction

Table 5.1: Spearman correlation coefficient of porosities with length scales of columnar samples in direction x and yz, values significant at a 95% level are printed bold, at a 90% marked with a star, number of observations $n_x = 12$, $n_{yz} = 30$

x	ϕ_{im}	ϕ_{eff}	ϕ_t	l_c	ϕ_{im}/s	Med(R)	l_{maj}	l_{min}	l_{tp}
ϕ_{im}	1	**0.69**	**0.90**	0.47	0.15	-0.04	-0.06	-0.16	**0.66**
ϕ_{eff}		1	0.46	**0.90**	-0.36	-0.50*	-0.32	**-0.58**	0.19
ϕ_t			1	0.36	0.45	0.31	0.09	0.10	**0.77**
l_c				1	-0.34	-0.46	-0.23	-0.46	0.07
ϕ_{im}/s					1	**0.95**	0.15	**0.66**	**0.64**
Median(R)						1	0.12	**0.65**	0.56*
l_{maj}							1	**0.64**	-0.07
l_{min}								1	0.29
l_{tp}									1

yz	ϕ_{im}	ϕ_{eff}	ϕ_t	l_c	ϕ_{im}/s	Med(R)	l_{maj}	l_{min}	l_{tp}
ϕ_{im}	1	**0.86**	**0.95**	**0.63**	0.35*	0.12	**0.70**	**0.76**	-0.21
ϕ_{eff}		1	**0.78**	**0.52**	0.07	-0.21	**0.65**	**0.69**	-0.24
ϕ_t			1	**0.59**	**0.42**	0.22	**0.68**	**0.82**	-0.03
l_c				1	**0.52**	**0.37**	0.26	**0.75**	0.04
ϕ_{im}/s					1	**0.89**	0.11	**0.42**	**0.52**
Median(R)						1	0.01	0.28	**0.59**
l_{maj}							1	**0.43**	0.09
l_{min}								1	0.02
l_{tp}									1

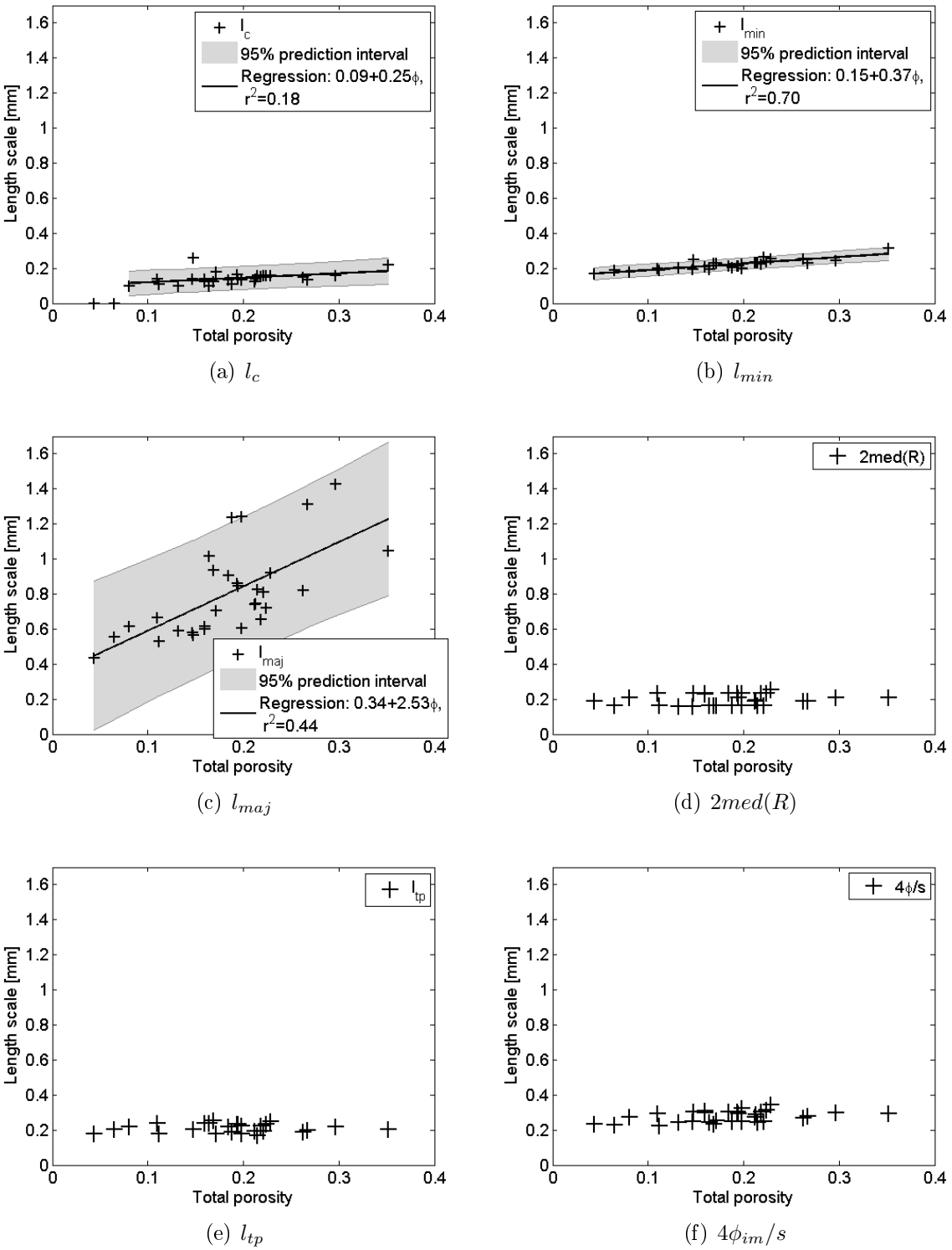

(a) l_c (b) l_{min}

(c) l_{maj} (d) $2med(R)$

(e) l_{tp} (f) $4\phi_{im}/s$

Figure 5.7: Relationship between the length scales (critical length scale l_c, minor ellipse axis l_{min}, major ellipse axis l_{maj}, twice the median of the pore radius distribution (2med(R)), two-point correlation length l_{tp} and four times the pore volume to surface ratio $4\phi_{im}/s$) and the total porosity for columnar samples with flow in yz direction, including linear regressions for the ones with significant correlation. Regression for critical length scale only for non-zero l_cs.

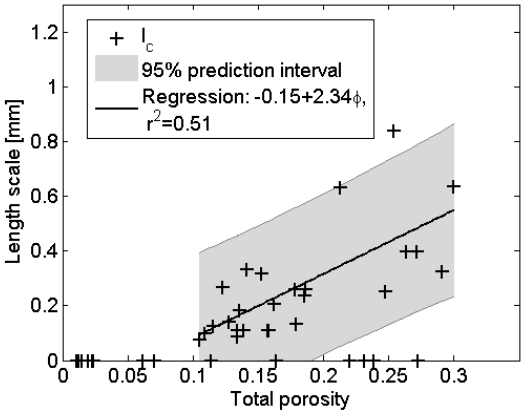

(a) l_c

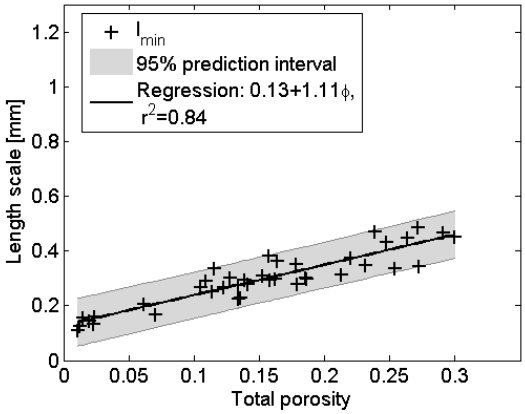

(b) l_{min}

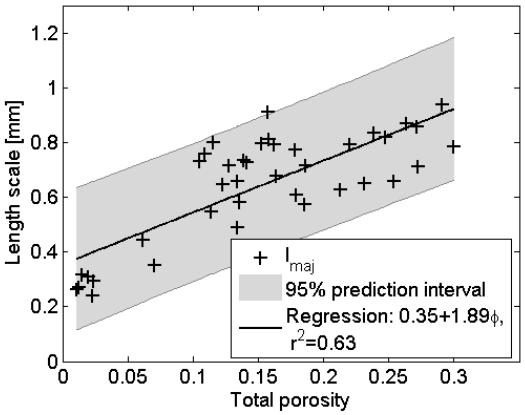

(c) l_{maj}

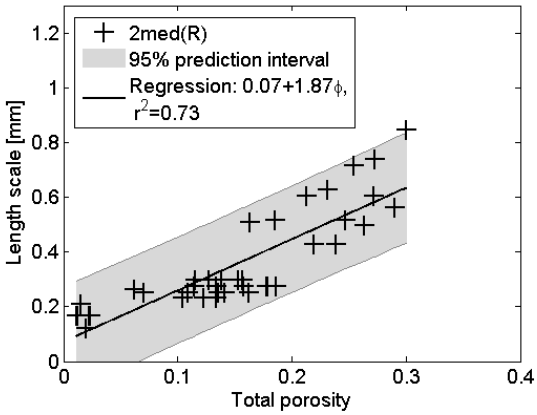

(d) $2med(R)$

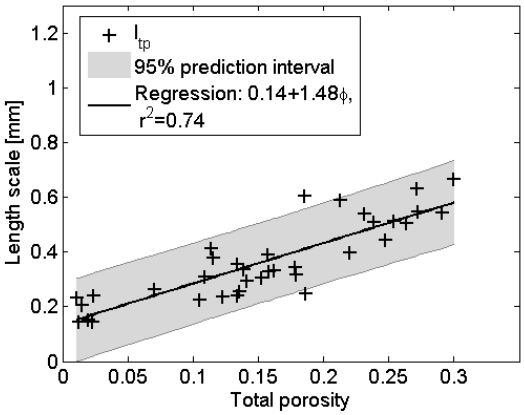

(e) l_{tp}

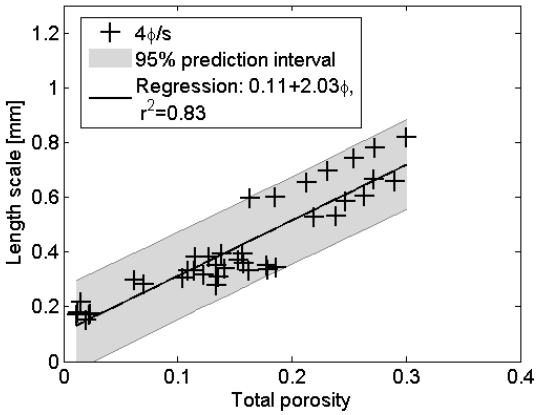

(f) $4\phi_{im}/s$

Figure 5.8: Relationship between the length scales (critical length scale l_c, minor ellipse axis l_{min}, major ellipse axis l_{maj}, twice the median of the pore radius distribution (2med(R)), two-point correlation length l_{tp} and four times the pore volume to surface ratio $4\phi_{im}/s$) and the total porosity for non-columnar samples, including linear regressions for the ones with significant correlation. Regression for critical length scale only for non-zero l_cs.

Table 5.2: Spearman correlation coefficient of porosities with length scales for non-columnar samples, values significant at a 95% level are printed bold, number of observations $n = 39$

yz	ϕ_{im}	ϕ_{eff}	ϕ_t	l_c	ϕ_{im}/s	Median(R)	l_{maj}	l_{min}	l_{tp}
ϕ_{im}	1	**0.57**	**0.98**	**0.59**	**0.90**	**0.86**	**0.72**	**0.89**	**0.83**
ϕ_{eff}		1	**0.52**	**0.88**	**0.44**	**0.37**	**0.58**	**0.48**	**0.34**
ϕ_t			1	**0.57**	**0.90**	**0.88**	**0.66**	**0.88**	**0.85**
l_c				1	**0.50**	**0.44**	**0.50**	**0.49**	**0.43**
ϕ_{im}/s					1	**0.98**	**0.66**	**0.90**	**0.93**
Median(R)						1	**0.58**	**0.87**	**0.94**
l_{maj}							1	**0.84**	**0.57**
l_{min}								1	**0.85**
l_{tp}									1

was 2.2 and it did not vary with porosity.

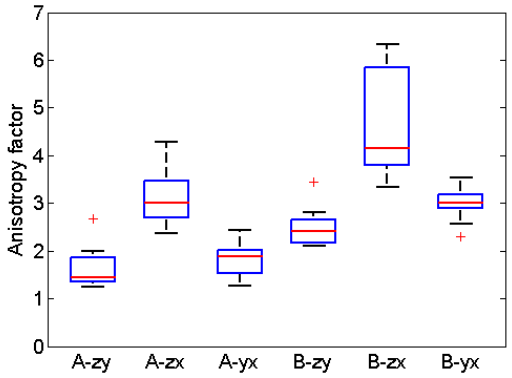

Figure 5.9: Anisotropy of the columnar samples for the different directions from A the two-point correlation functions and B the major and minor axes of the fitted ellipse

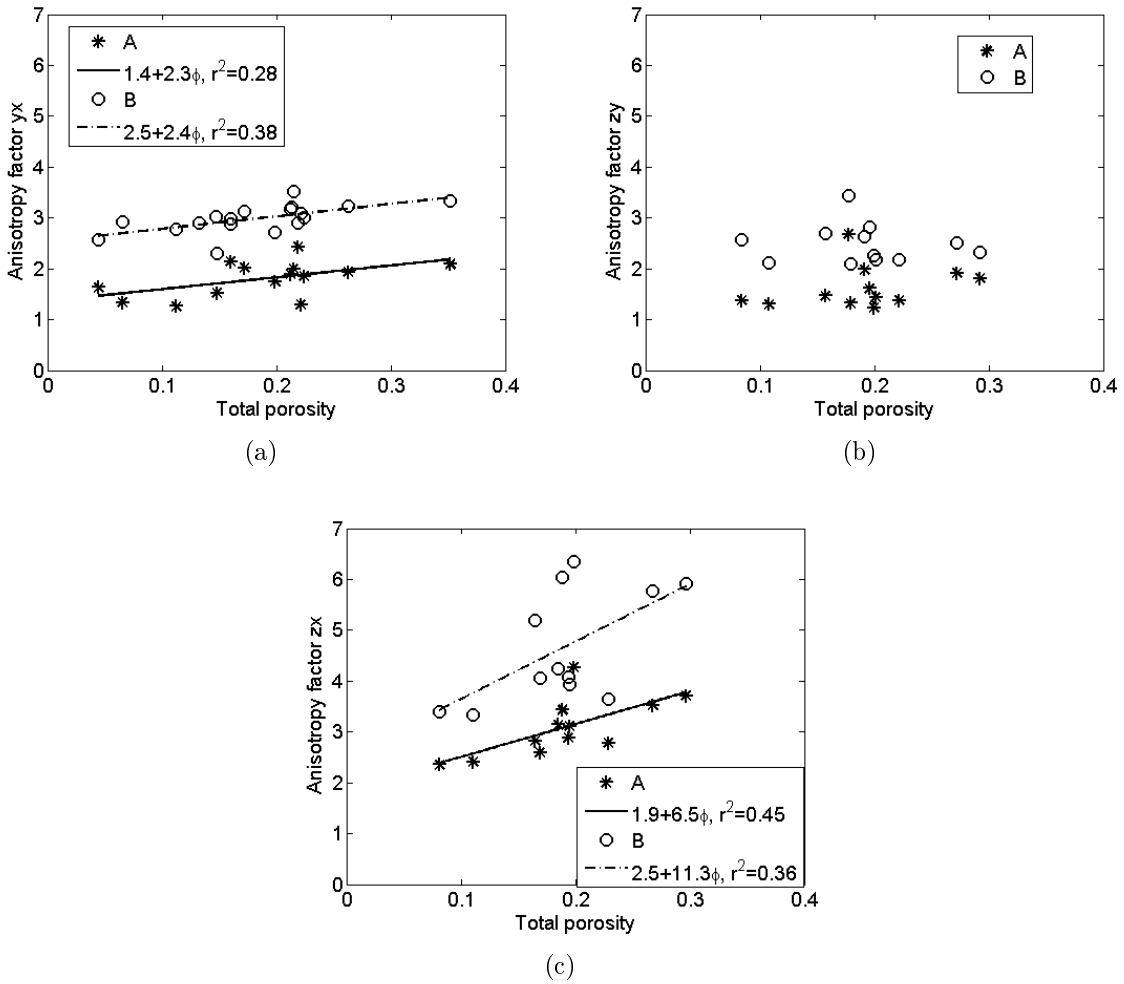

Figure 5.10: Anisotropy of the columnar samples for the different directions from A the two-point correlation functions and B the major and minor axes of the fitted ellipse with respect to the total porosity, r^2 statistic, (a)y-x, (b) z-y, (c) z-x

Tortuosities

Our estimates of hydraulic tortuosity τ_h and electrical tortuosity τ_e ranged from 1.0 to 3.2 and 1.6 to 15.3, respectively. They were not significantly correlated with each other (figure 5.11). The hydraulic tortuosities were not significantly correlated with the porosities while the electrical tortuosities were significantly negatively correlated at a 95% significance level ($r = -0.35$ for total porosity). There was a relationship between formation factor ($F = \tau_e^2/\phi$) and total porosity of the form $F = \phi_t^{-m}$ with $m = 2.6$.

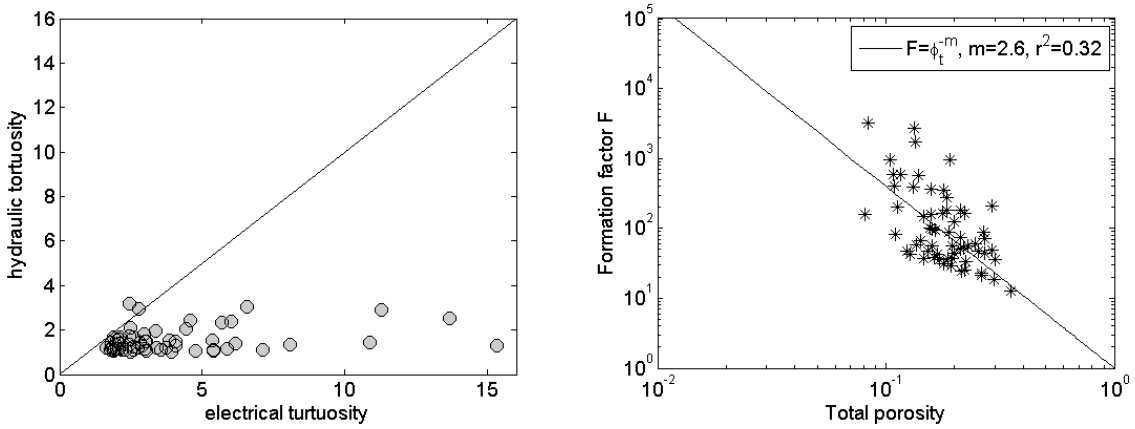

(a) (b)

Figure 5.11: Hydraulic and electrical tortuosity: (a) Scatterplot, (b) formation factor vs total porosity

5.2 Flow from LBM

In the following the 3D pore structures of the samples and the flow fields from LBM under a vertical pressure gradient are shown. Figure 5.12 includes both 3D images and a horizontal section for each sample. For all the columnar samples two perspectives are shown, of which one is looking parallel to the columnar structure. Samples 1a3l, 2a3 and 2a4 were clipped in the vertical to a homogeneous region, because there was a layer of almost no connectivity (see discussion). Samples 2a3 and 2a4 display a quite homogeneous flow with many small channels, while 1a3l is less homogeneous but still has multiple connecting channels and 2a2 only has a couple of tortuous channels meandring through the sample. The non-columnar samples 1b1 and 2c1 are not connected in the vertical and have more rounded pores, 2c1 much larger than 1b1. Sample 4c1 has a mixed structure, with some large pores with ice slices in them, some rounded pores and one large channel carrying almost all of the transport. As will be elaborated on in section 5.3 the implemented periodic boundary conditions caused closing of some channels in the model which has to be taken into account when interpreting the flow fields.

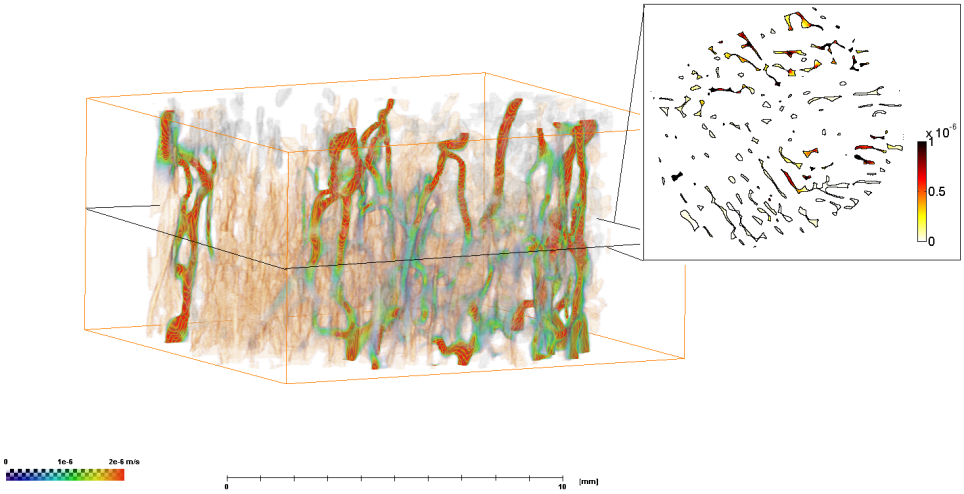

(a) 1a3l with horizontal section

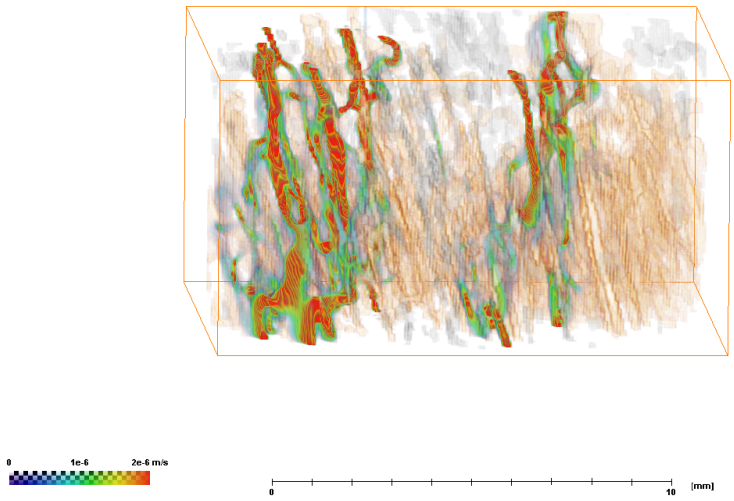

(b) 1a3l - parallel to columnar structure

Figure 5.12: Flow from LBM for the 7 samples, unconnected pore space in gray, connected pore space in orange, velocities on a scale from transparent blue to opaque red, horizontal sections include pore outlines in black and velocities in white-red-black scale, different velocity scales for the different samples: (a)+(b) 1a3l, (c) 1b1, (d)+(e) 2a2, (f)+(g) 2a3, (h)+(i) 2a4, (j) 2c1, (k) 4c1

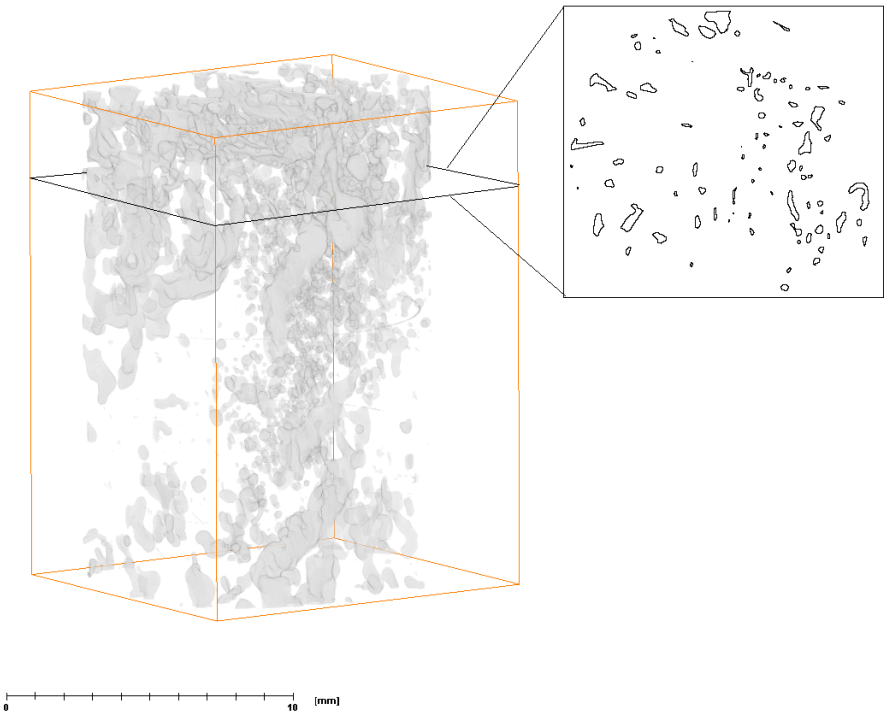

(c) 1b1

Figure 5.12: continued

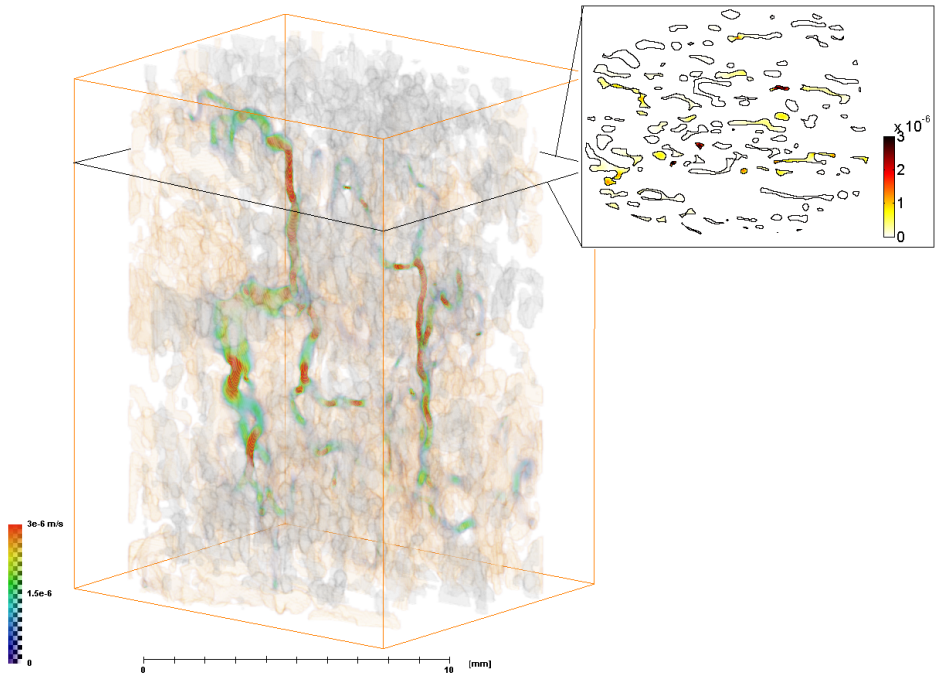

(d) 2a2

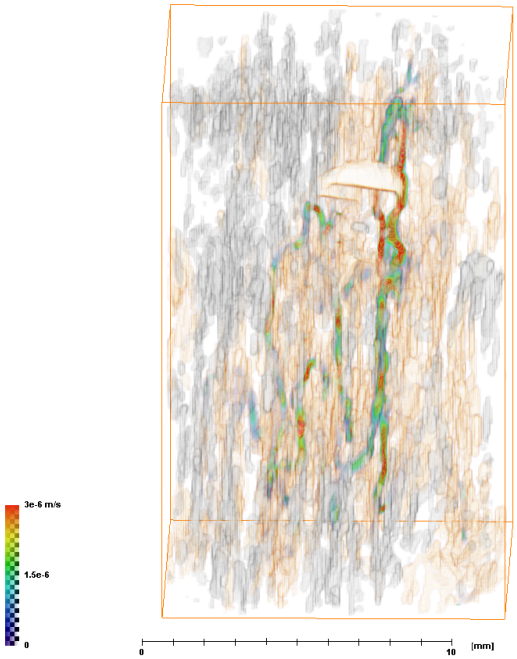

(e) 2a2

Figure 5.12: continued

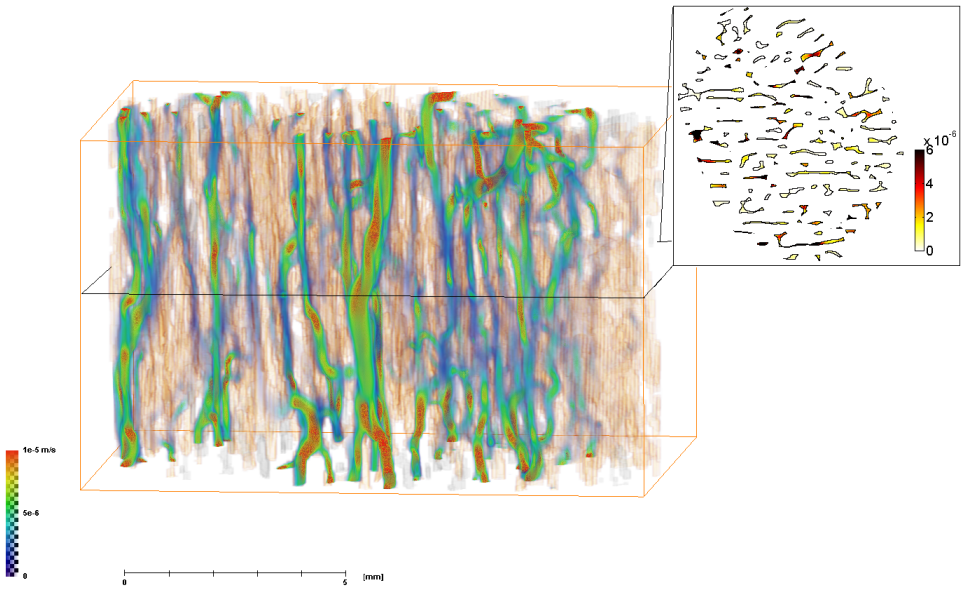

(f) 2a3

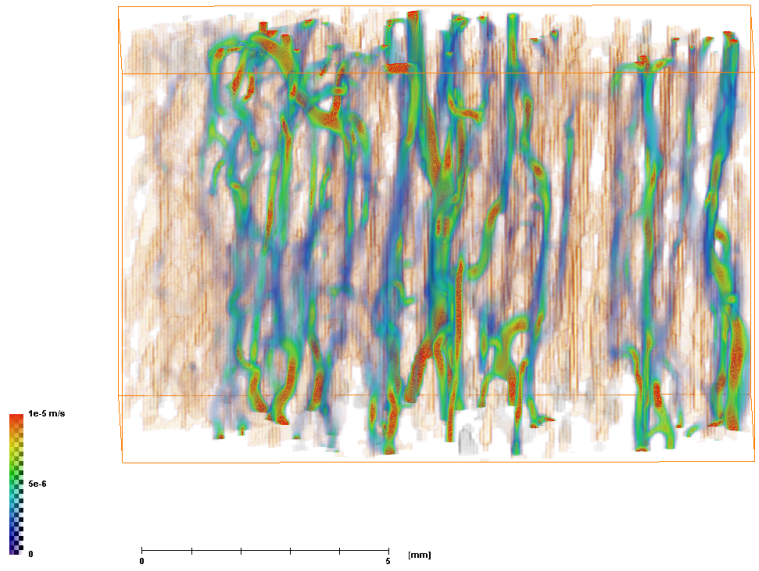

(g) 2a3

Figure 5.12: continued

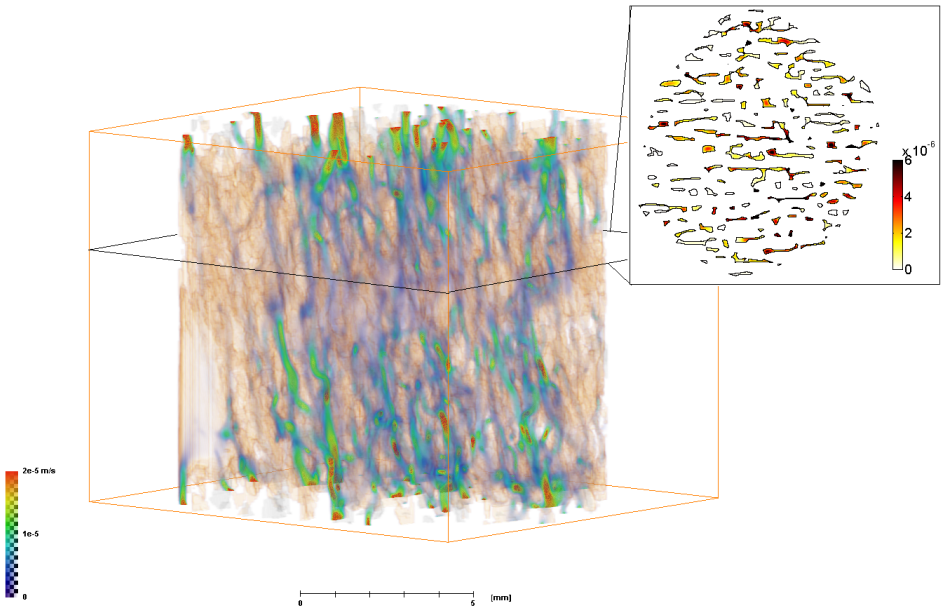

(h) 2a4

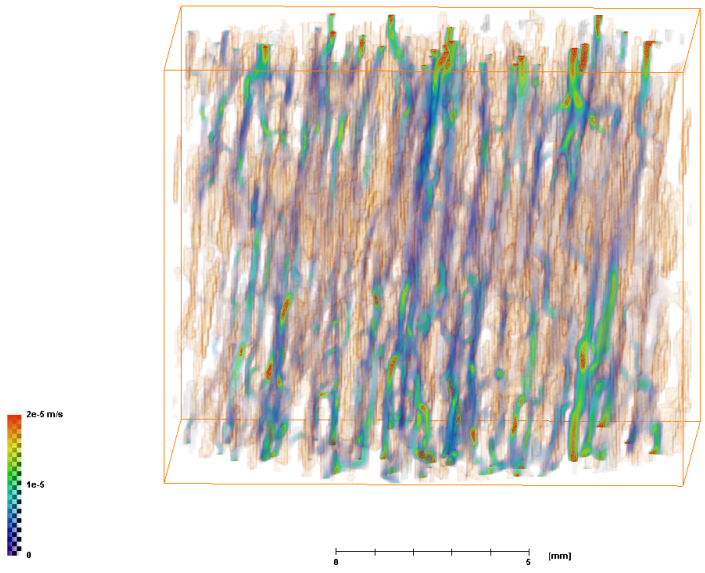

(i) 2a4

Figure 5.12: continued

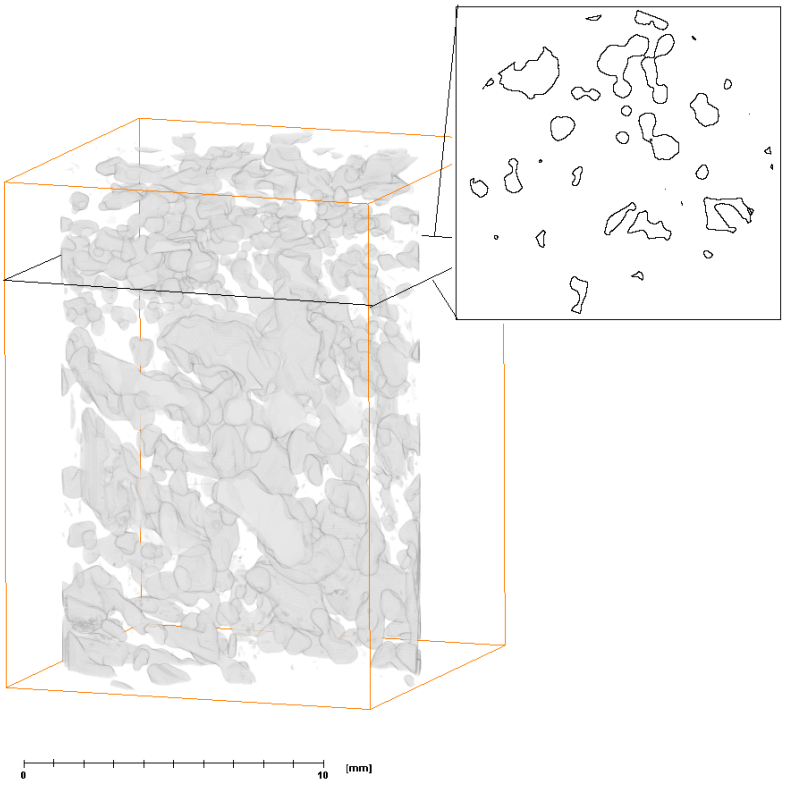

(j) 2c1

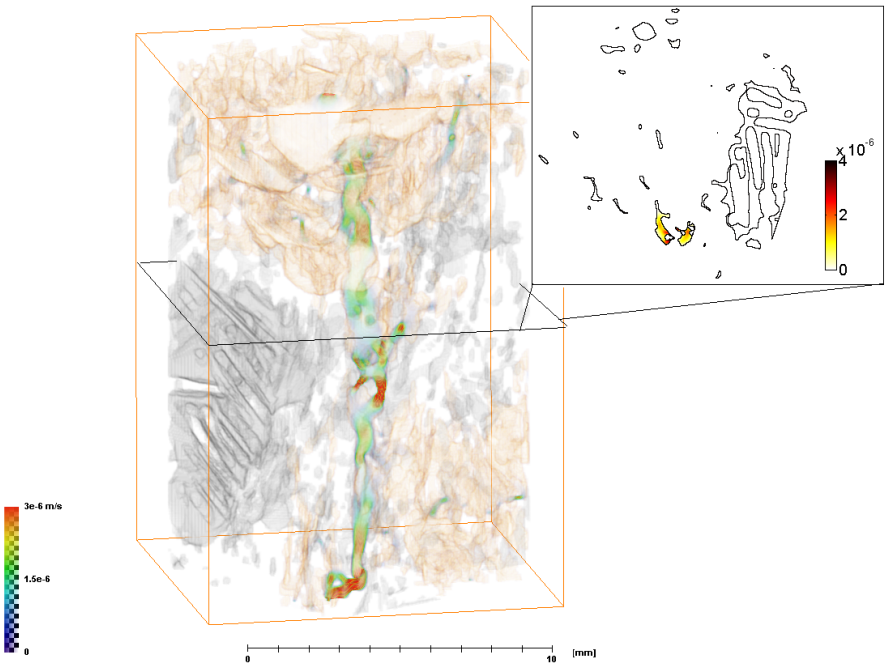

(k) 4c1

Figure 5.12: continued

5.3 Permeabilities from LBM

In the following the permeabilities resulting from the lattice Boltzmann modelling are presented. The permeabilities were related to the three different porosities, imaged, total and effective. Columnar and non-columnar ice was treated separately because its different structure (see length scales and pore size distributions) makes it likely that it behaves differently. Our hypothesis is that the columnar arrangement of pores increases connectivity and thus permeability along the columns and decreases it perpendicular to the columns compared to the isotropic arrangement of pore in granular ice. Figures 5.14 and 5.13 show the LBM permeabilities with respect to the total porosities for columnar and non-columnar samples. Only the columnar samples in y and z direction had a dependency on porosity with comparably little scatter - in the x direction there were impermeable samples at high porosities - which is why the main focus of further analysis is on them.

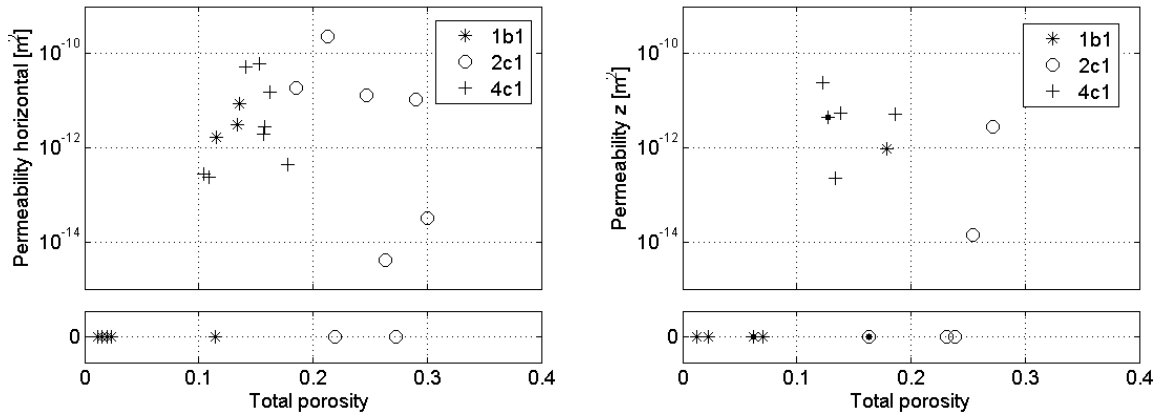

(a) Horizontal (b) Vertical

Figure 5.13: Original LBM permeability vs total porosity for the non-columnar samples on a semilog-scale, includes both cells and samples, samples are emphasized with dots; the lower part of the diagrams shows the zero-permeability samples that cannot be included in the top log-scale graph

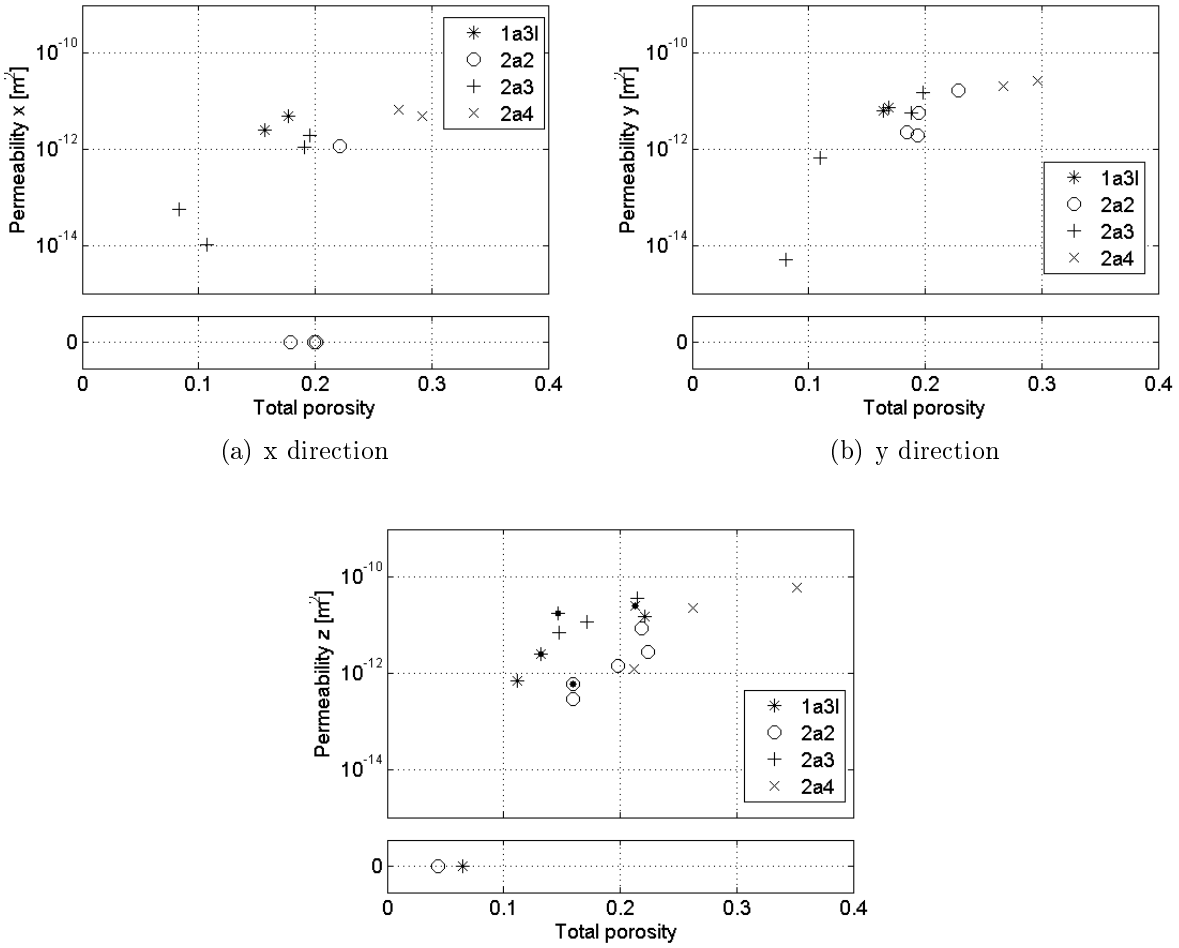

(a) x direction

(b) y direction

(c) z direction

Figure 5.14: Original LBM permeability vs total porosity for the columnar samples on a semilog-scale, x-direction perpendicular and y-direction parallel to the layers of the columnar structure; includes both cells and samples, samples are emphasized with dots; the lower part of the diagrams shows the zero-permeability samples that cannot be included in the top log-scale graph

The scope of this work did not include a complete test of the LBM model of GeoDict, but before studying the LBM permeabilities closer, we tried to estimate their uncertainty through modelling a simple channel geometry that has an analytical solution. Two model runs were done through straight channels of 0.2 and 0.4mm radius and ca.4mm length at a resolution of $22\mu m$ (9 and 18 voxels radius). The LBM permeabilities were 96 and 97% respectively of the analytically expected permeabilities (equation 2.9). As can be expected from the permeabilities, the velocities were slightly underestimated by LBM (see figure 5.15). Especially right beside the central velocity maximum there were two local minima. We conclude that for this geometry the agreement between LBM and the analytical solution was very good.

All original model runs were done with periodic boundary conditions. In order to understand the behaviour of the model with respect to this at relatively low porosities, three model runs were done with cylindrical channels tilted at 4, 8 and 15 degrees (figure 5.16). The permeabilities were 82, 27 and 0 % of the analytical solutions. This is because the pore in the top and bottom layer of the model domain overlap only for 4 and 8 degree slope and not for 15 degree slope, which leads to a negligible LBM permeability. This means that open pores appear as closed in the model whenever there is no pore on the opposite side.

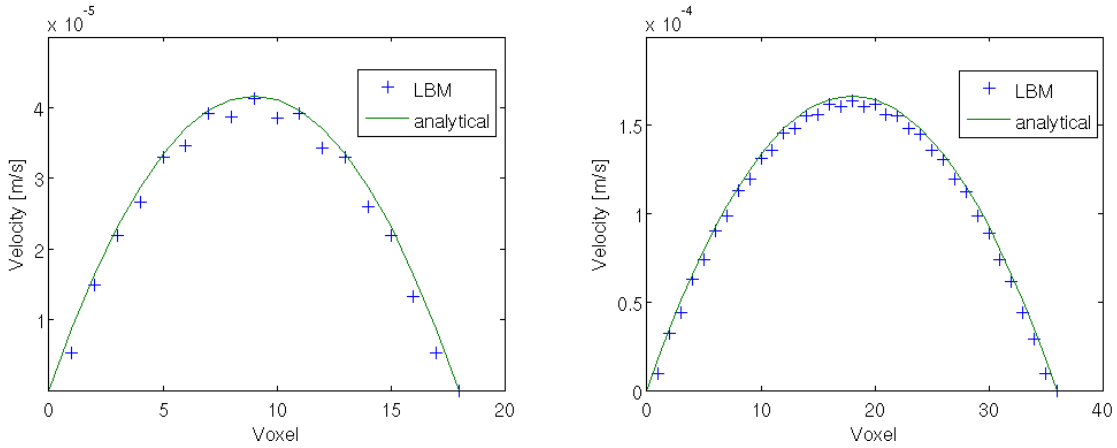

(a) r=0.2mm (b) r=0.4mm

Figure 5.15: LBM results vs analytical solution in straight channel of 9 and 18 voxels radius and 4 mm length, modelled at $22\mu m$

In order to get an estimate of the effect of partly or completely closed pores a scaling factor $1/n$ was introduced - with n being the ratio of overlap area of pores in top and bottom layer to the top pore area. This refers to the pores that belong to the effective porosity. Scaling the permeabilities by dividing by n ($k_{sc} = k_{lbm}/n$) assumes that the not overlapping pore area fraction is associated with a separate pore system that has the same permeability per area as the overlapping area fraction. In our data n ranged from 0 to 0.40. The samples to be studied further, columnar in y and z-direction, excluding the one with $n = 0$, had scaling factors of 0.002 to 0.24, with a mean of 0.10 (figure 5.17(a).
The scaling factors in the single channel tests were 0.55 and 0.14 for angles of 4 and 8

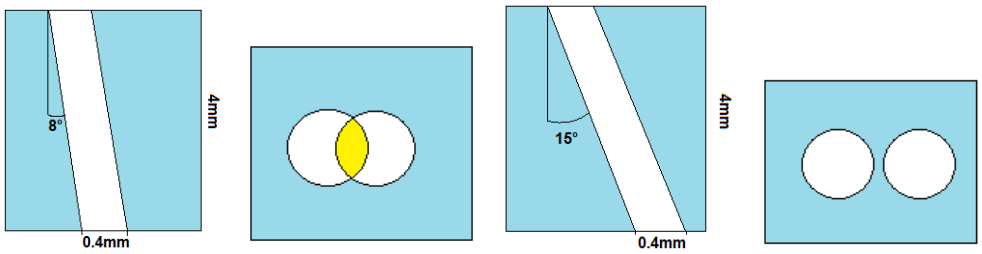

(a) 8 degree slope (b) Overlap at 8 degrees (c) 15 degree slope (d) No overlap at 15 degrees

Figure 5.16: Schematic of the simple channel geometry for (a) 8 degrees slope and (c) 15 degrees slope and how pore areas in top and bottom layer overlap for these two situations (b) and (d)

degrees respectively. The scaled LBM permeabilities of the channels were 149 and 190 % of the analytical solutions. Scaling in this manner thus overestimated the analytical permeability for single channels that are partly open. Our more complex samples had both partly open channels, completely open channels and closed channels. How much the LBM permeabilities underestimate and the scaled permeabilities overestimate the true permeabilities of the samples depends on the structure of the samples.
One way to avoid the problem of artificially closed channels is to use the LBM on a mirrored domain. Side effects of this will be discussed in section 6, but are assumed to be smaller than the errors arising from pure periodic boundary conditions. To evaluate a more appropriate scaling factor, four columnar cells with scaling factors covering the whole range were remodelled with a mirrored domain. There appeared to be a relationship between the ratio between mirrored and scaled permeabilities ($\frac{k_{mirr}}{k_{lbm}/n}$) and the reciprocal scaling factor n (figure 5.17). By linear regression of $\frac{k_{mirr}}{k_{lbm}/n}$ on n we determined that a better correction of the original permeabilities with less overestimation would be $k_{corr} = \frac{k_{lbm}}{n}(0.08 + 1.18n)$. Permeabilities mentioned in the following sections have been corrected in this manner unless otherwise mentioned.

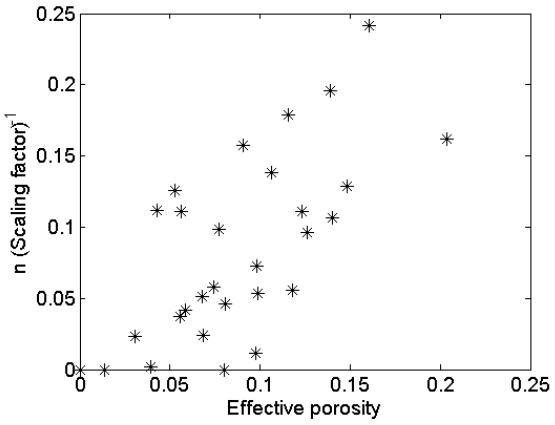

(a) Scaling factor

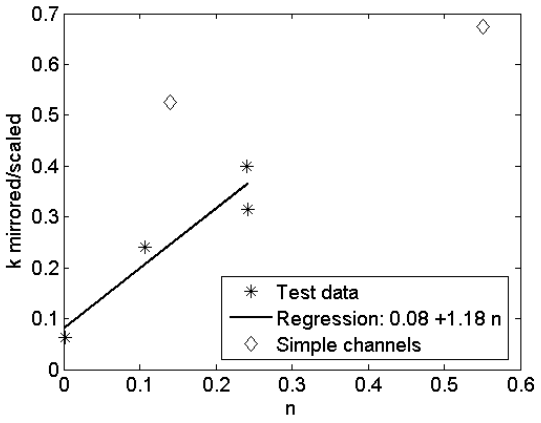

(b) Correction factor

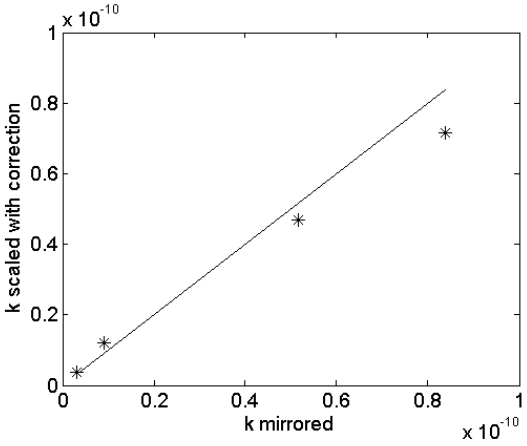

(c) Applied correction

Figure 5.17: Scaling and correction of LBM permeabilities: (a) reciprocal (n) of the scaling factors of the columnar samples and cells in yz-direction, (b) correction factor from regression of overestimation of permeabilities scaled with n for four cells that were remodelled with a mirrored domain, also showing the two simple channels for comparison, (c) applied correction factor for these four cells

Columnar ice

The permeability of the four columnar ice samples exhibited a dependency on both porosity and direction. Figures 5.18 to 5.20 show the permeabilities in relation to the imaged, effective and total porosities for the 3 directions. For y and z direction (vertical and parallel to the layers of the columnar structure) a trend of increasing permeabilities with increasing porosities was observable. For the x direction which is perpendicular to the layers of the columnar structure the scatter was much larger. The maximum imaged porosities (total porosities) rendering the samples impermeable were 12% (20%) for the x direction and 4% (6%) for the z direction.

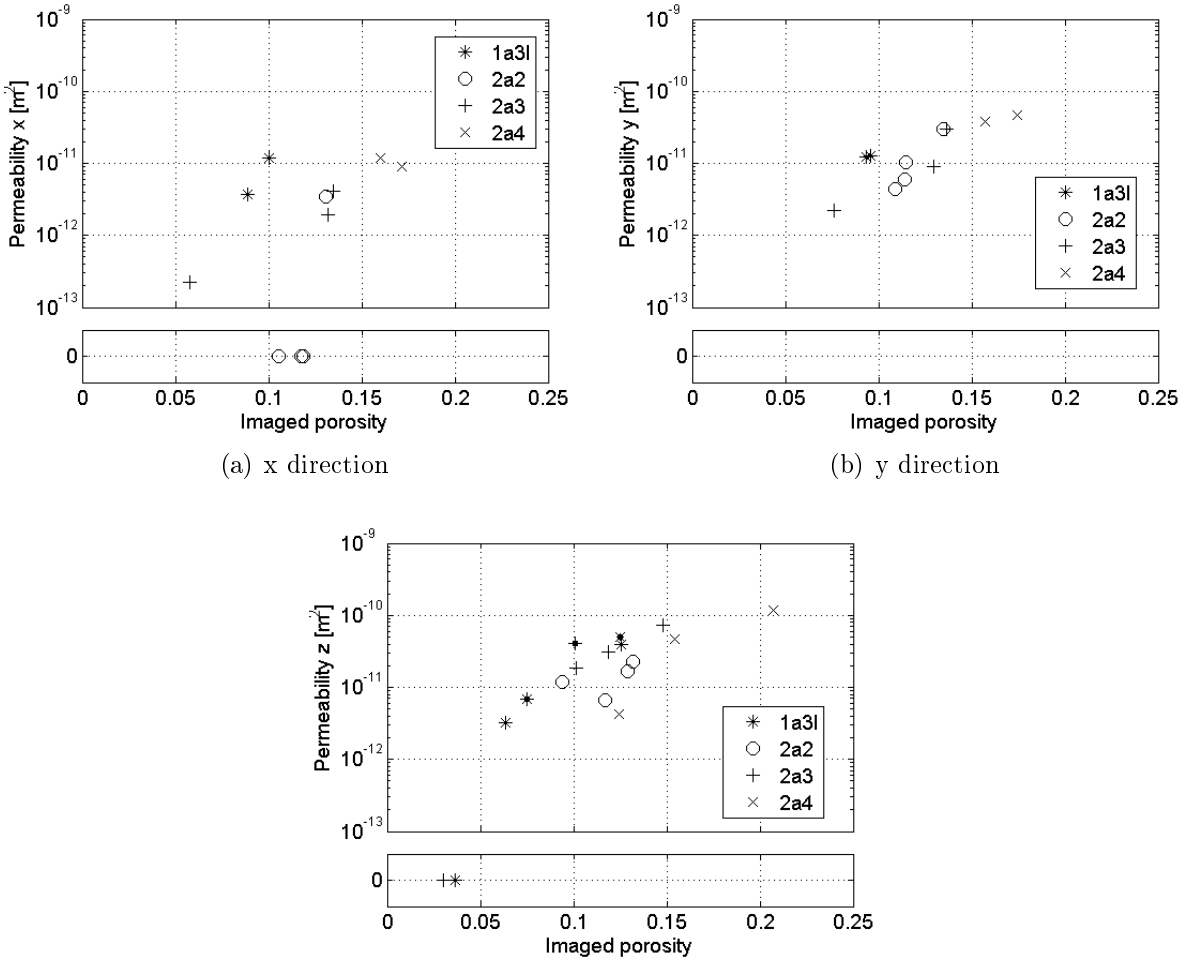

(a) x direction

(b) y direction

(c) z direction

Figure 5.18: Permeability vs imaged porosity for the columnar samples on a semilog-scale, x-direction perpendicular and y-direction parallel to the layers of the columnar structure, includes both cells and samples, samples are emphasized with dots; the lower part of the diagrams shows the zero-permeability samples that cannot be included in the top log-scale graph

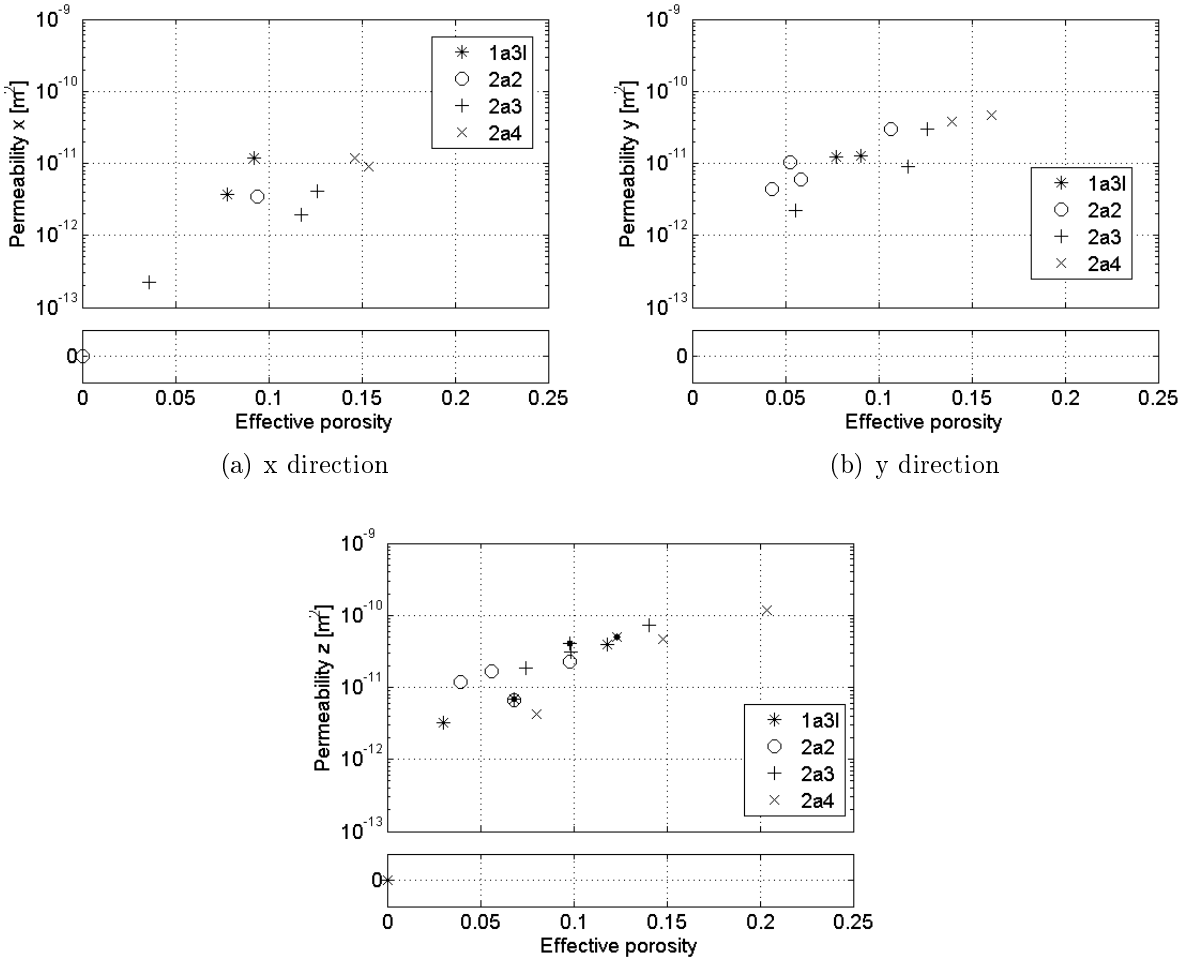

(a) x direction

(b) y direction

(c) z direction

Figure 5.19: Permeability vs effective porosity for the columnar samples on a semilog-scale, x-direction perpendicular and y-direction parallel to the layers of the columnar structure, includes both cells and samples, samples are emphasized with dots; the lower part of the diagrams shows the zero-permeability samples that cannot be included in the top log-scale graph

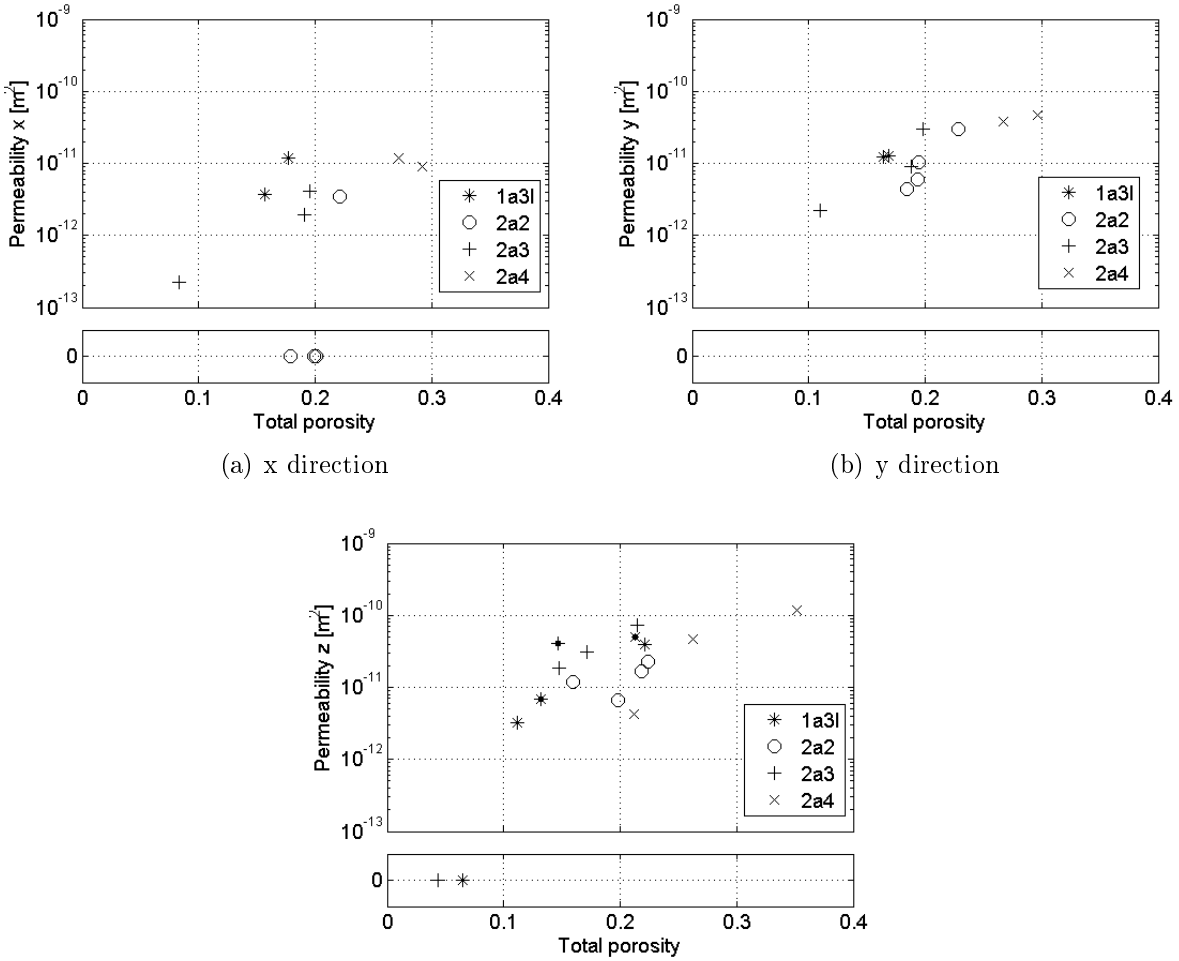

(a) x direction

(b) y direction

(c) z direction

Figure 5.20: Permeability vs total porosity for the columnar samples on a semilog-scale, x-direction perpendicular and y-direction parallel to the layers of the columnar structure, includes both cells and samples, samples are emphasized with dots; the lower part of the diagrams shows the zero-permeability samples that cannot be included in the top log-scale graph

The data was first checked for normality using the Lilliefors test (Lilliefors, 1967). Since the permeability distributions were skewed, they were normalized by a logarithmic transformation (excluding the zeros, $n_x = 8$, $n_y = 9$, $n_z = 15$). Next, one-way analysis of variance of the logarithm of k_x,k_y and k_z was performed. ANOVA assumes independence of the observations. This was violated as cells and whole samples were included and the cells for the different directions overlap. However, the high local variability of porosities and permeabilities make it likely that the assumption of independence is valid anyway. It was significant at a 95% level that k_x,k_y and k_z were drawn from different distributions ($p = 0.004$). A multiple comparison test showed that the mean of logarithm of k_x was smaller than that of k_y and k_z at a 95% significance level, while k_y and k_z did not have significantly different mean logarithms from each other (see figure 5.21). Thus in the following k_y and k_z were considered together and termed k_{yz}. The ratio of the geometric mean permeability in x direction to the one in yz direction was 0.21 (95% CI: 0.09 to 0.53, table 5.3).

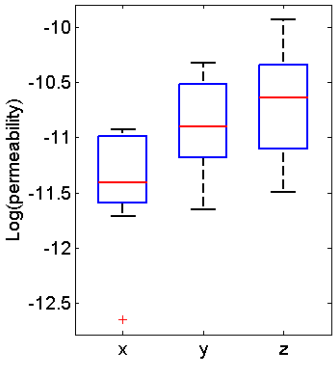

Figure 5.21: Boxplot of the logarithms of the (non-zero) permeabilities of the columnar samples in x, y and z direction showing median, 25th and 75th percentile as well as maximum and minimum not considered outliers and outliers

Table 5.3: Difference between (non-zero) permeabilities in the horizontal perpendicular to the columns and parallel and vertical

Direction	mean(log_{10}(k))	geometric mean(k)	median(k)	Difference in mean(log_{10}(k))	ratio between geometric means(k)
x	-11.4	$3.6e-12$	$3.9e-12$	-0.3 to -1.1	0.09 to 0.53
yz	-10.8	$1.7e-11$	$1.7e-11$		

Because of the large scatter and the low number of observations in the x-direction, no further analysis was performed for these values. The non-zero permeabilities in y and z direction were correlated with the three porosities, the two tortuosities and 5 length scales as in table 5.4. This was done with the spearman correlation to ensure a valid correlation coefficient even for those variables that were not normally or lognormally distributed. All

Table 5.4: Spearman correlation coefficient of porosities, tortuosities and length scales with the non-zero scaled permeabilities in direction yz, values significant on a 95% level are printed bold, number of observations 24

	ϕ_{im}	ϕ_{eff}	ϕ_t	τ_h	τ_e	
k_{yz}	**0.69**	**0.84**	**0.62**	-0.29	**-0.39**	
	l_c	ϕ_{im}/s	Median(PSD)	l_{tp}	l_{maj}	l_{min}
k_{yz}	**0.55**	-0.06	-0.20	-0.34	0.31	**0.58**

three porosities as well as τ_e, l_c and l_{min} were significantly correlated with k_{yz} at a 95% level. Neither median of the pore radius distributions, nor pore volume to surface ratio, major axis length or two-point length scale were correlated with the permeability on a 95% significance level.
As a consequence linear regression was performed of the yz permeability on each of the three porosities after a logarithmic transformation, thus fitting a power law of the form $k = a\phi^e$ to the data. Assumptions for linear regression are that the residuals are normally distributed with a mean of 0, that they are homoskedastic and uncorrelated. The first assumption was verified with a Lilliefors test. The second assumption was checked by looking at a plot of residuals against the model permeability and except for some outliers there was a fairly constant variance. The results in table 5.5 and figure 5.22 show exponents with 95% CI between 1.3 and 4.0, lowest values for the effective porosity, and explained variances (r^2) on the logarithmic scale of between 47 and 68%.
Another regression included also the length scales l_c and minor axis ($k = a\phi^e l^2$) with an exponent of 2, which is physically predetermined from the permeability's unit of m^2. Including the length scale term did not change the explained variance considerably, but resulted in factors a on the order of 0.01 and reduced the porosity exponents' 95% CI to 0.9 to 3.4 (see table 5.5 and figure 5.23).

Both the equivalent channel model (eq. 2.12), the Kozeny equation (eq. 2.10), the Kozeny-Carman equation (eq. 2.11) and the Katz and Thompson model (eq. 2.13) can be expressed in the form $k = a\phi^e\tau^b l^2$ with a tortuosity τ, a length scale l, a porosity ϕ and some parameters a,b and e. For the equivalent channel model $e = 1$, $b = -2$, $\tau = \tau_e$ and $l = \phi_{im}/s$; for the Kozeny equation $e = 1$, $b = 0$, $l = \phi_{im}/s$; for the Kozeny-Carman equation $e = 1$, $b = -2$, $\tau = \tau_h$ and $l = \phi_{im}/s$; and for the Katz and Thompson model $e = 1$, $b = -2$, $\tau = \tau_e$ and $l = l_c$. From their derivation it follows that the effective porosity should be the best predictor out of the three porosities and will be used in the following. For these models appropriate factors a were found (table 5.5, figure 5.24). The explained variances were lower than for the models with variable exponents and they overestimated permeabilities at low effective porosities. Of the four models the Kozeny and the Kozeny-Carman equation had the highest explained variances and least scatter.

Table 5.5: Parameters and their 95% CI for the power law fits $k = a\phi^e$ and $k = a\phi^e l^2$ for the three porosities and two length scales as well as $k = a\phi_{eff}^e \tau^b l^2$ below the line (representing: equivalent channel model (eq.2.12), Kozeny equation (eq.2.10), Kozeny-Carman equation (eq.2.11) and Katz and Thompson model (eq.2.13), including the r^2 statistic (logarithmic scale)

ϕ	length	τ	a	e	b	r^2
imaged	none	none	$8.6e-9\,[7.9e-10, 9.4e-8]$	2.9 ± 1.1	0	0.55
imaged	l_c	none	$0.080\,[0.0070, 0.91]$	2.1 ± 1.1	0	0.54
imaged	l_{min}	none	$0.046\,[0.0043, 0.49]$	2.3 ± 1.1	0	0.56
effective	none	none	$1.4e-9\,[3.8e-10, 5.2e-9]$	1.8 ± 0.5	0	0.68
effective	l_c	none	$0.034\,[0.0098, 0.12]$	1.5 ± 0.5	0	0.71
effective	l_{min}	none	$0.014\,[0.0038, 0.049]$	1.5 ± 0.5	0	0.69
total	none	none	$1.2e-9\,[1.7e-10, 8.4e-9]$	2.6 ± 1.2	0	0.47
total	l_c	none	$0.022\,[0.0034, 0.14]$	2.0 ± 1.1	0	0.52
total	l_{min}	none	$0.0085\,[0.0013, 0.057]$	2.0 ± 1.1	0	0.49
effective	ϕ_{im}/s	τ_e	$0.29\,[0.20, 0.40]$	1	-2	0.33
effective	ϕ_{im}/s	τ_h	$0.041\,[0.031, 0.055]$	1	0	0.50
effective	ϕ_{im}/s	τ_h	$0.072\,[0.054, 0.097]$	1	-2	0.50
effective	l_c	τ_e	$0.066\,[0.045, 0.097]$	1	-2	0.17

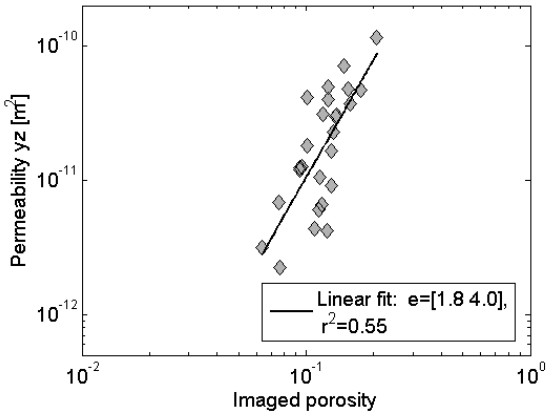

(a) Imaged porosity

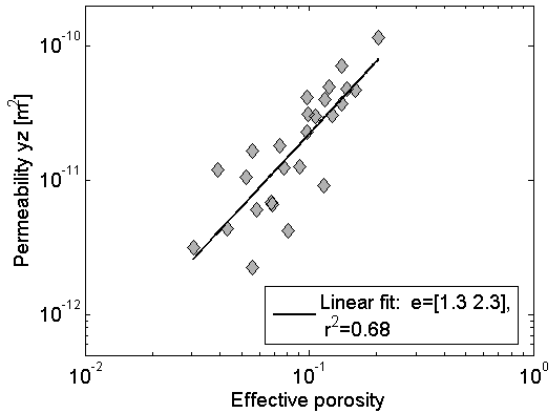

(b) Effective porosity

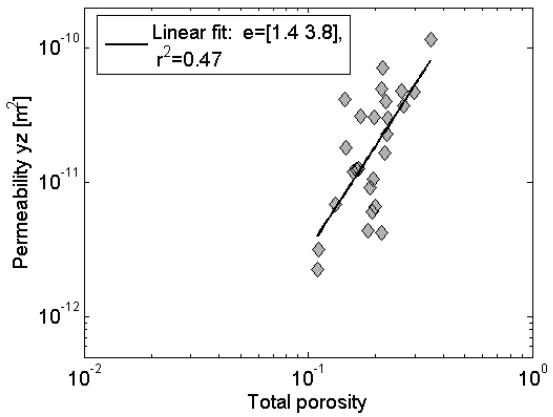

(c) Total porosity

Figure 5.22: Power law fits of the form $k = a\phi^e$ for the columnar samples for the three porosities - imaged, effective and total - to non-zero permeabilities in yz direction with the 95% CI of the respective exponents and the r^2 statistic

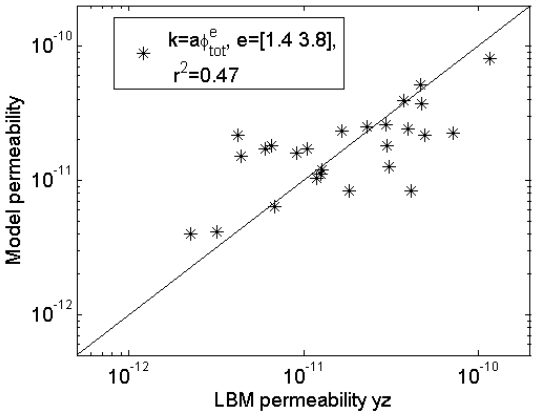

(a) yz direction - l_c

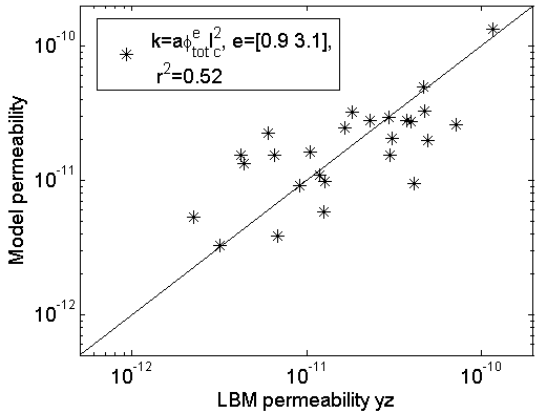

(b) yz direction - l_c

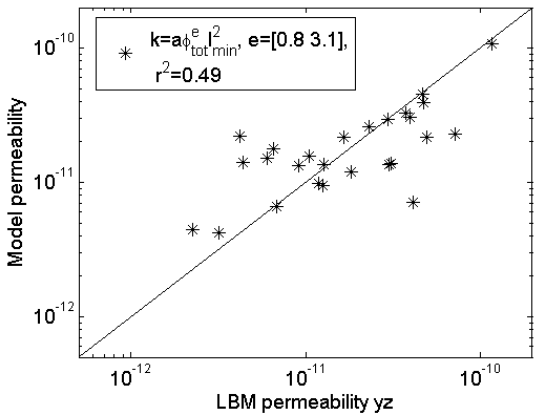

(c) yz direction - l_{min}

Figure 5.23: Power law fits of the form $k = a\phi^e l^2$ for the columnar samples for the length scales l_c,l_{min} and no length scale to non-zero permeabilities in yz direction with the 95% CI of the respective exponents and the r^2 statistic

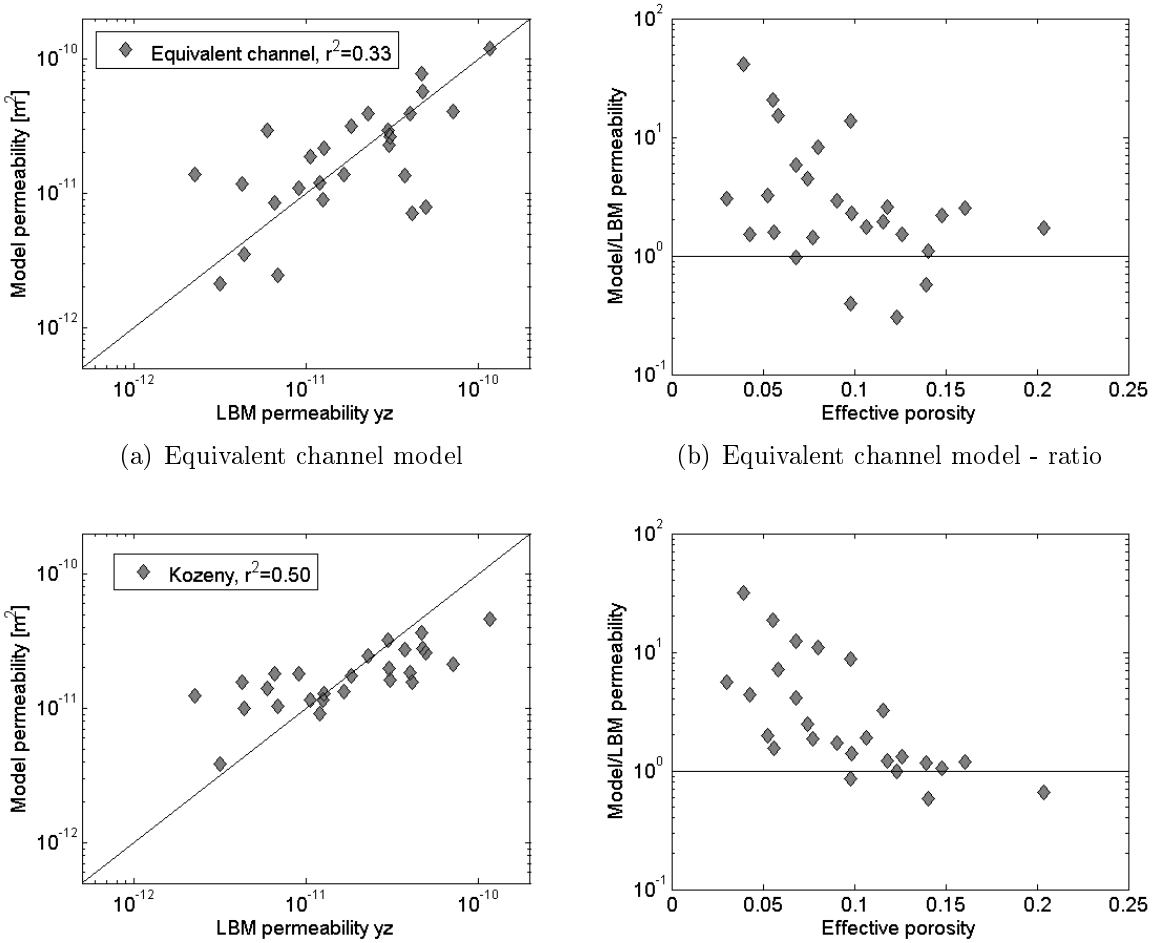

(a) Equivalent channel model

(b) Equivalent channel model - ratio

(c) Kozeny equation

(d) Kozeny equation - ratio

Figure 5.24: Permeabilities from models against LBM permeabilities in yz-direction and ratios of model and LBM permeabilities for (a)+(b) equivalent channel model, (c)+(d) Kozeny equation, (e)+(f) Kozeny-Carman equation and (g)+(h) Katz and Thompson model, including r^2 statistic

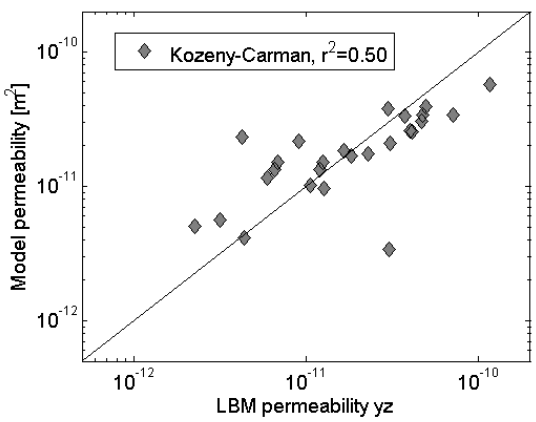

(e) Kozeny-Carman equation

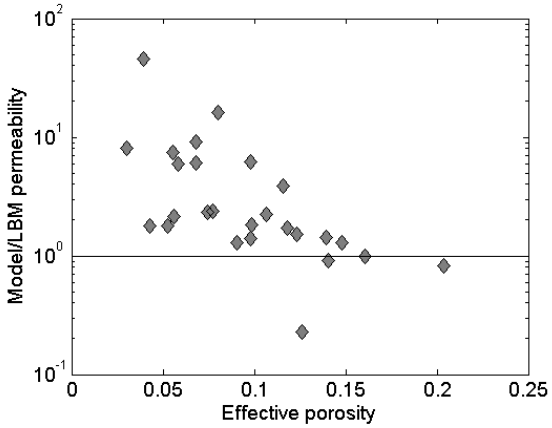

(f) Kozeny-Carman equation - ratio

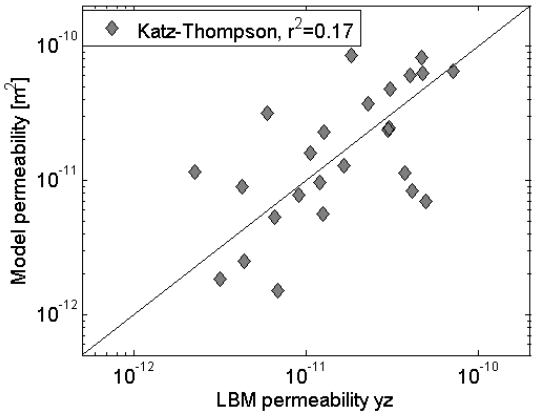

(g) Katz and Thompson model

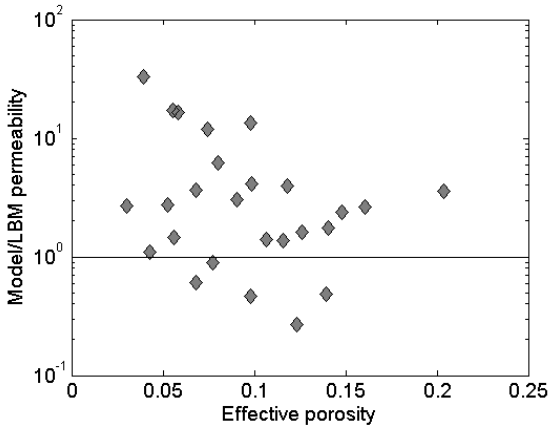

(h) Katz and Thompson model - ratio

Figure 5.24: (continued)

A percolation law of the form $k = a(\phi_t - \phi_c)^{e_c}$ where ϕ_c is a critical porosity below which the permeability becomes zero was brought into a linear form by taking the logarithm. Regressions were then done between the logarithm of the permeability and the difference between the total porosity and critical porosities between 0 and 15% with 1% increment. Both the model and the LBM permeabilities of zero were set to 10^{-15} to be able to include them. Varying this number between 10^{-15} and 10^{-19} did not change the fit results, only the r^2 which increases with decreasing replacement values for 0. Percolation fits are displayed in figure 5.25 where the fit with the highest r^2 statistic on the logarithmic scale is emphasized ($a = 4e-10m^2\,[1e-10, 2e-9]$, $\phi_c = 0.07$, $e_c = 1.5 \pm 0.8$). From figure 5.25(a) one can see that between critical porosities of 7 and 11 % the r^2 statistic was almost constant at a high level. Therefore we consider this as a measure of uncertainty for the critical porosity.

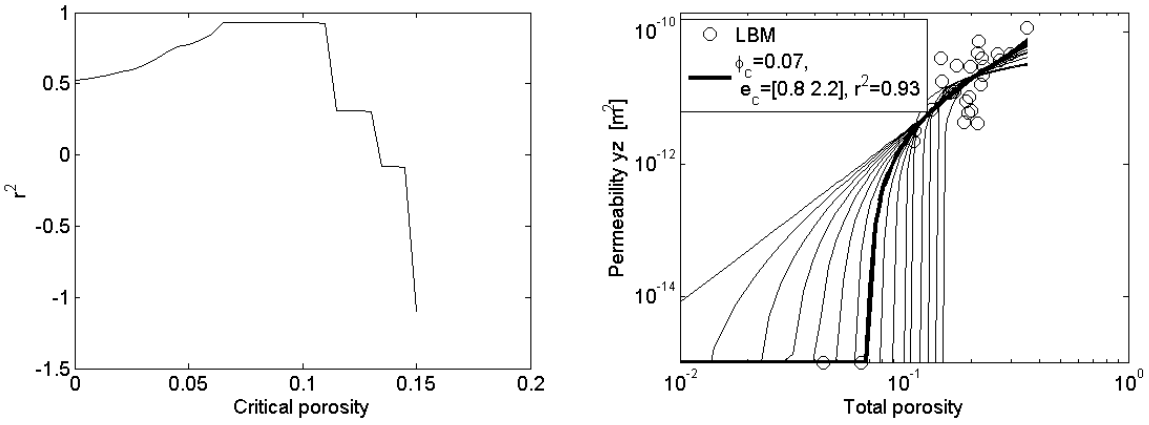

Figure 5.25: Percolation fits of the form $k = a(\phi_t - \phi_c)^{e_c}$ for the columnar samples in the yz direction: (a) logarithmic r^2-statistic against critical porosity, (b) percolation fits for $\phi_c = [0\ 0.15]$ with exponent of the best fit with permeabilities of 0 set to $10^{-15}m^2$

Non-columnar ice

The non-columnar samples did not show any obvious dependence of neither horizontal nor vertical permeability of porosity in the range 0 to 30 % (Figure 5.26). One should keep in mind that the correction factor that was applied to the LBM permeabilities was derived from columnar samples and could be different for non-columnar samples. There was no significant evidence that the horizontal and vertical permeability observations came from different distributions or similar distributions with different means (t-test of $log(k)$, $p = 0.77$), as can be seen in the boxplot in figure 5.26. The maximum imaged porosities (total porosities) not rendering the samples permeable were much higher than for the columnar ice (horizontal 16%(28%), vertical 14%(23%)). The non-columnar samples did not have non-zero permeabilities with a significantly different logarithmic mean from the columnar samples in yz direction (ANOVA, $p = 0.88$), but did have significantly different mean than the columnar sample in x direction ($p = 0.01$).

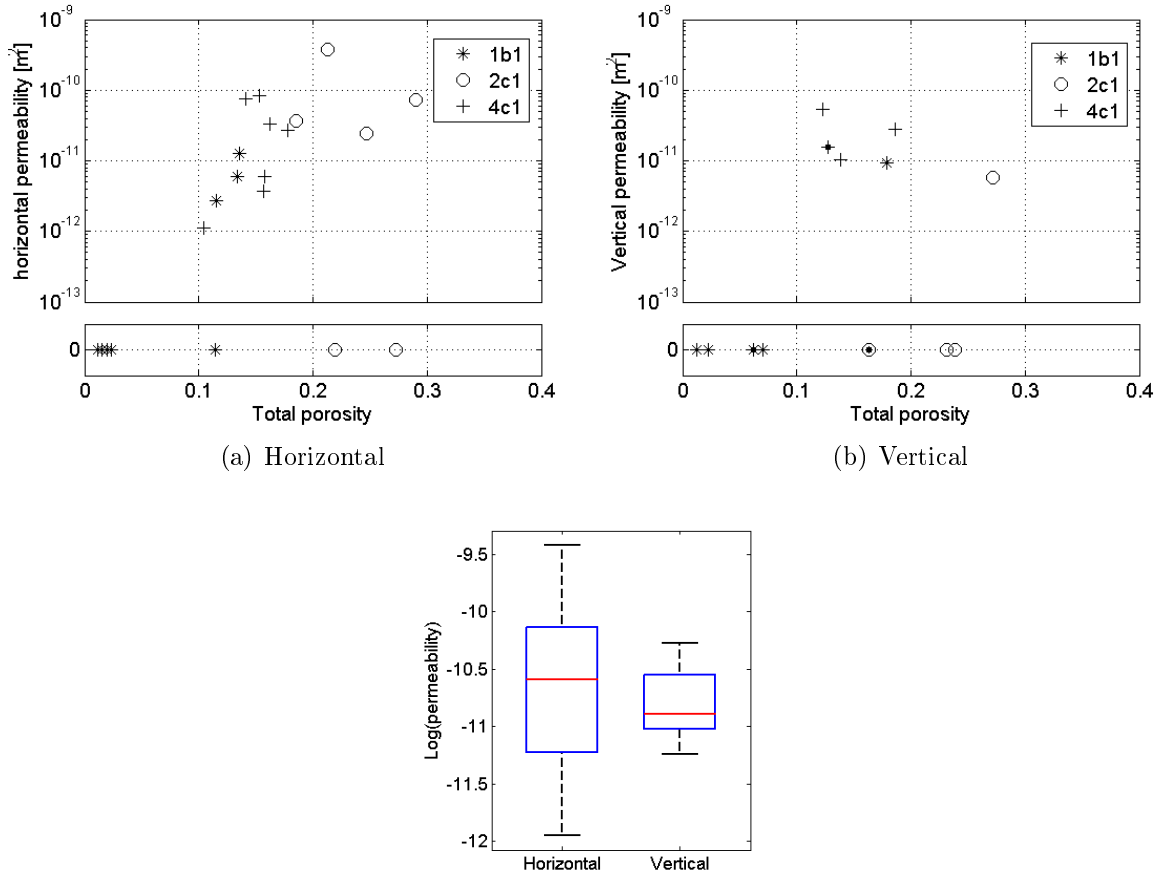

(a) Horizontal

(b) Vertical

(c) Boxplot

Figure 5.26: Horizontal and vertical permeabilities for the non-columnar samples (includes both cells and samples, samples are emphasized with dots, the lower part of the diagrams shows the zero-permeability samples that cannot be included in the top log-scale graph) and boxplots of their logarithms showing median, 25th and 75th percentile as well as maximum and minimum not considered outliers

Profile

Samples 2a2, 2a3, and 2a4 were taken from the same core, 2c1 from a neighbouring core. Together this presented a permeability profile of the ice (figure 5.27). The permeabilities from 2c1, the granular sample, had a large range. On average there was evidence for increasing permeabilities with depth in the columnar layers. Between 4 and 8cm horizontal permeabilities did not change much.

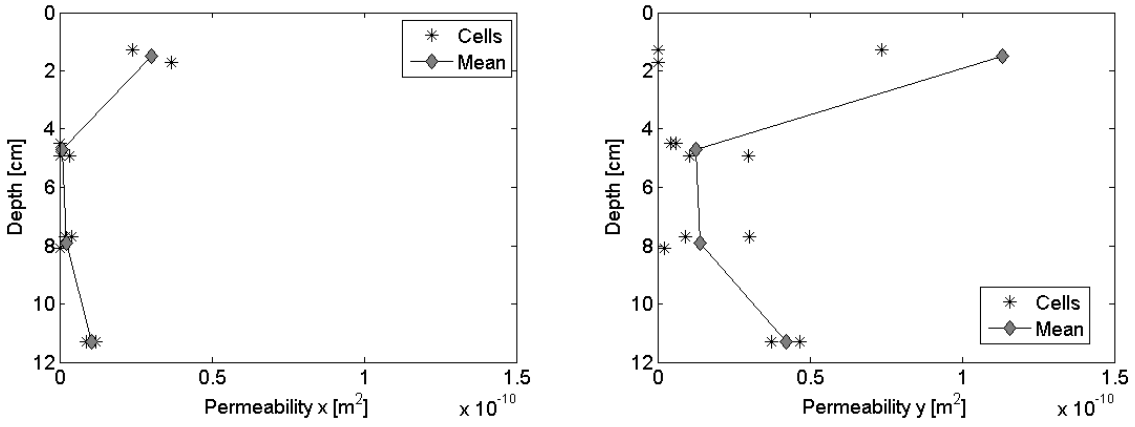

(a) x - permeability

(b) y - permeability

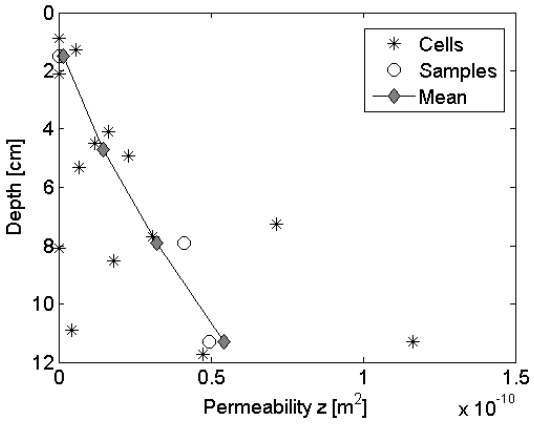

(c) z - permeability

Figure 5.27: Vertical profile of permeabilities from samples 2c1, 2a2, 2a3 and 2a4 - includes both values from the cells and the whole samples where applicable and their means, in y direction one outlier at 1.8cm outside of range at 3.8 $10^{-10}m^2$

6 Discussion

6.1 Error sources and limitations

The major error sources of our method are microstructure changes before and during centrifuging, incomplete centrifugation, segmentation and model uncertainties. These are discussed in this section.

Sample preparation

The temperatures were kept within $\pm 0.5K$ of the *in situ* temperatures for all samples but one (1b1) through transport in styrofoam boxes and storage in temperature-controlled freezers. This kept microstructure changes due to temperature fluctuations to a minimum. In previous studies of sea ice the temperature variations that samples experienced have often been much larger and it is a problem inherent to all the methods of permeability measurements discussed in section 2.3 except for tracer studies. However, all microstructure parameters but the total porosities that we related the permeabilities to, i.e. effective and imaged porosities and length scales, were retrieved from the same data as the permeabilities, so that they are all similarly affected by morphological changes. Therefore, the established relationships are most likely valid for sea ice even if microstructure change took place unless structural change during storage differs from changes under natural conditions.
Another uncertainty is introduced by possibly incomplete removal of the brine during centrifugation. The retained brine includes both brine in isolated inclusions and removable brine that has not been removed. Only the latter can block the channels affecting the permeability. Freitag (1999) calculated that 10% retained brine evenly distributed along the walls of a system of pipes of a constant size would reduce the permeability by 10%. However, refrozen brine can block the flow more efficiently by closing channels. Other quantities such as porosity, pore size distribution and length scales are more linearly affected by retained brine. Quantifying the uncertainty from incomplete centrifugation is not trivial. From salinity measurements of the residual ice we found that an average of 35% of the brine was retained in the cores (Maus et al., 2011), which is higher than the average of 20% that were retained when Weissenberger (1992) centrifuged older ice at $2700 ms^{-2}$ for 10 minutes. This is a considerably higher acceleration than we used. However, we had warm samples of young ice that are less strong and less resistant to brine removal and the samples turned white as expected for sufficient centrifugation. The brine velocity during centrifugation depends on permeability and porosity, such that for low permeabilities and porosities it takes more time to remove all brine.
One indicator of incomplete removal of brine is the existence of closed pores. These can be either air inclusions or pores from which the brine was centrifuged but that were closed off by refreezing of brine that was not removed. Air porosities in sea ice seldom exceed 5% (Nakawo, 1983; Light et al., 2003). Closed porosities in our data were below 1% in the columnar and below 3% in non-columnar ice. Closed pore fractions were smaller than 15% for the columnar ice, below 25% for the non-columnar ice except sample 1b1 (figure 6.1), which means that incomplete removal of brine was most likely not a major problem. Sample 1b1 had closed pore fractions up to 80%, but extremely low porosities in some

layers. Especially in a layer below the center in the vertical the porosity was very low (figures 5.12 and 6.2). One section of this low porosity layer is shown in figure 6.2 where one can see much salt arranged in a columnar structure. This was one of the first samples to be taken and centrifuged and two things happened: it was stored and centrifuged at a temperature $1.4K$ below the *insitu* temperature and centrifuged for 10 minutes instead of 15. It appears that the cold storage effectively closed bottlenecks and made centrifuging ineffective. Additionally the centrifugation was probably too short.

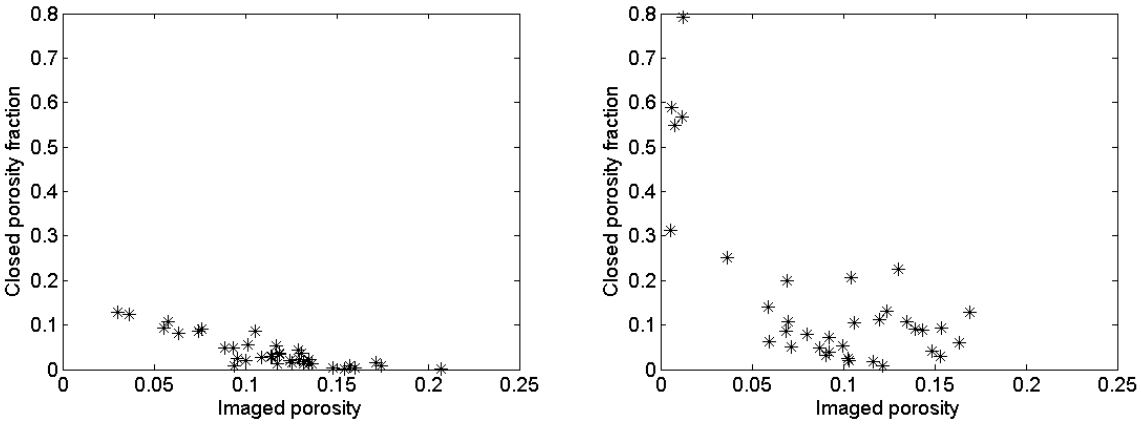

(a) Columnar ice (b) Non-columnar ice

Figure 6.1: Closed pore fraction in (a) columnar and (b) non-columnar ice

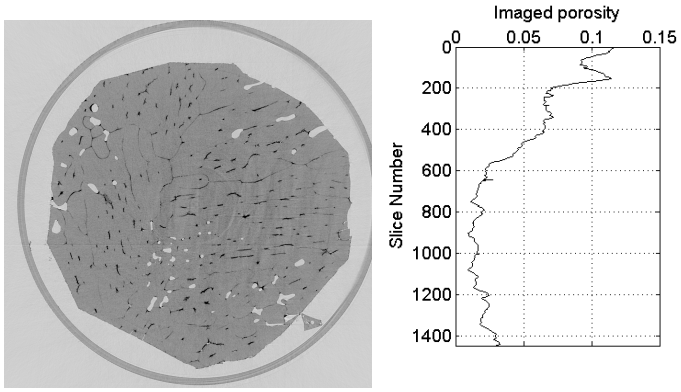

(a) A section from low porosity layer in sample 1b1 (b) Porosity profile of sample 1b1

Figure 6.2: Low porosity, high salt content in sample 1b1: (a) CT image of sample 1b1, low porosity layer: air light gray, ice gray, salt dark gray; the colours have been changed a little to make the difference between salt and ice visible in the print version, (b) imaged porosity profile of sample 1b1

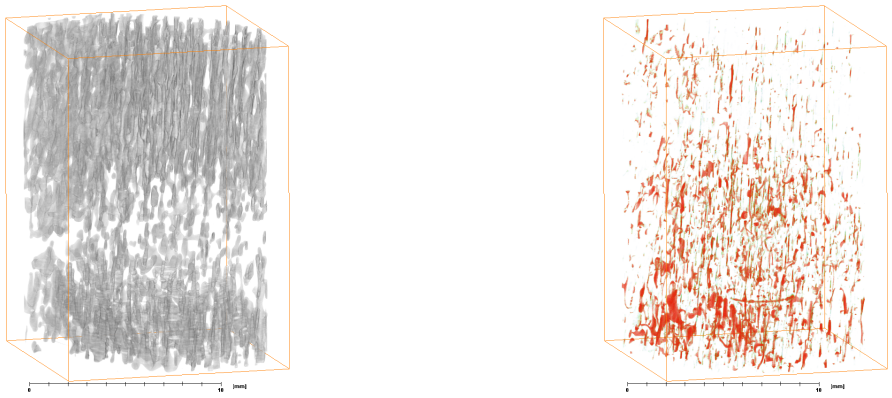

(a) Pores (b) Salt

Figure 6.3: Pores and salt in samples 2a3, (image produced in Amira to give an impression of the salt content, no real segmentation done)

This sample was not the only one which had a layer of low porosity. Both 1a3l and 2a3 (figure 4.11) also had low porosity layers below the center and in 2a4 on the top. Because such strong inhomogeneity within samples can give misleading permeabilities, the samples were cropped to a homogeneous zone for analysis. As an example, figure 6.3 shows the pore and salt of the whole sample 2a3. The low porosity layer does not show a larger salt content, though there is a tendency to increasing salt further down in the sample. That there was no excess of salt in the low porosity layer makes incomplete centrifugation an improbable explanation for sample 2a3. Maybe the low porosity layer was not an effect of sampling, but marks some change in microstructure during growth. Both low and high porosity bands have previously been identified in sea ice (Cole et al., 2004) and our porosity variability investigation in section 4.1 (figure 4.11 and 4.12) also large variations, especially in the vertical.
To sum up, it is difficult to determine the best centrifuge speed and our comparably low speed could have led to incomplete removal of the brine and thus a stronger reduction of permeability than porosity. However, only sample 1b1 has some indications of this.

Imaging

The SXRT images had a very good quality with only few ring artifacts. Ring artifacts usually do not affect the permeability. Due to the good quality the segmentation errors are expected to be low compared to model uncertainties. In section 4.1 we discussed different segmentation methods and concluded that the most appropriate for our data and purpose was Otsu's algorithm (Otsu, 1979) in 3D. The sensitivity to the threshold was also quantified in that section and it became clear that quantities such as porosity and pore surface to volume ratio depend linearly on the threshold within the relevant range, while the open porosity fraction (effective porosity) and thus the permeability depend non-linearly on the threshold. For porosity and pore surface to volume ratio we concluded an uncertainty of less than $\pm 5\%$.

LBM

As explained in the result section (5.3), real periodic boundary conditions introduce errors in low porosity media, since pores that are positioned where there is not a pore on the opposite site of the domain appear as closed and no flow passes through them. Approaches to avoiding this are either mirroring the whole domain or introducing an inflow and outflow region. This was tested with a circular channel of 0.4mm radius tilted 15 degrees (figure 6.4). For the mirrored domain the model permeability was 96% of the analytical. Two cases of inflow/outflow regions of thickness L were modelled, one with very thin layers at top and bottom ($L = 5 voxels$) and one with layer thickness of one half of the domain $L = L_z/2$. In the small inflow region case the permeability was 50% of the analytical, in the large inflow region case 89%. Thus mirroring produced the best solution for this geometry, but had the highest computational demand.

For more complex pore systems one could expect problems arising by mirroring because of additional discontinuities and pore constrictions. If the permeability is controlled by the constrictions this could affect the permeability. Nevertheless we used permeabilities found for mirrored domains for four samples as the „correct“ solution to scale the permeabilities to. Since the permeability underestimation by using real periodic boundary conditions depends on the exact structure of the sample, the corrected data should be considered with care. We consider it a better estimate than the original LBM data, especially for low porosities, yet propose that all samples be remodelled with either a mirrored domain or other types of boundary conditions that have been introduced to avoid having to mirror the domain (Fredrich et al., 2006). Figure 6.5 shows the difference between scaled and original data with respect to the total porosity. One can see that the correction reduces the slope considerably. This is because in low porosity samples it is more unlikely that there is overlap between pores in the bottom and top layer of the sample.

Another uncertainty related to the LBM is the length of iteration. We usually stopped after 10000 iterations or when an accuracy of 10^{-4} was reached. For some cases, where the model had not reached the accuracy of 10^{-4}, but terminated at 10000, we reran the model without stopping at 10000 steps until it reached the accuracy. The difference in permeabilities turned out to be on the order of 10%. This is much less than the uncertainty introduced by the periodic boundary conditions.

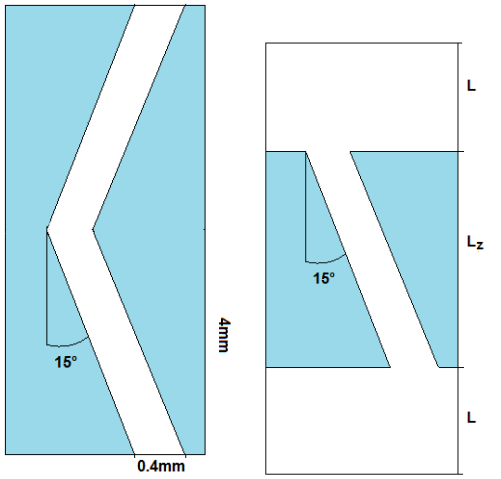

(a) mirrored (b) inflow and outflow region

Figure 6.4: Schematic of the simple channel geometry for 15 degrees slope with (a) mirrored domain and (b) inflow outflow regions of length L

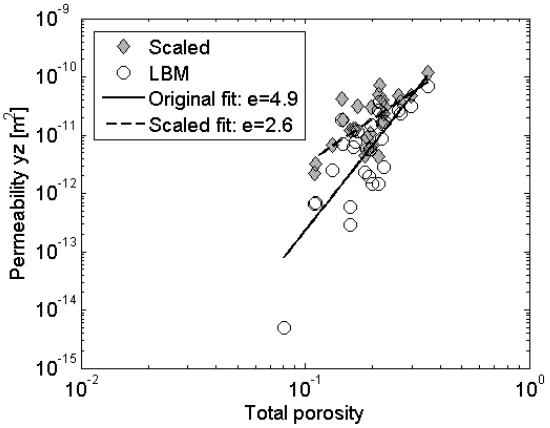

Figure 6.5: Scaled vs original data

The pressure gradients of 10 and $100 Pa/m$ used in the LBM model matched our ice (see section 4.3). Additional wave action or an extra snow load could lead to larger pressure gradients, consequently Reynold's numbers larger than 1 and semi-turbulent or turbulent flow and make our LBM model of Stokes flow and Darcy's law invalid. One would expect the permeability then to be smaller than the Darcian, as the turbulence will act as friction. We conclude that the largest uncertainty of our permeability measurements is due to the periodic boundary conditions in the model and our correction for it. One should consider the permeabilities order of magnitude estimates until more samples are modelled with a mirrored domain.

Size effects and limitations due to ice type

As discussed in section 4.3 computer memory limitations make it important to consider both sample size and resolution carefully.
We used resolutions of 35 μm and less. This means the 5 voxel diameter limit required for good results (Sukop and Thorne, 2007) corresponds to a $175 \mu m$ diameter. With the first major peak of pore radii being at around $175 \mu m$ for the columnar samples and even more for the non-columnar (figure 5.3), the major part of the pores is expected to be described well in the model. However, the critical length scale l_c that describes the diameter of pore throats had values down to $100 \mu m$ (figures 5.7 and 5.8). This is below the limit with a 35 μm resolution, but just around the limit for a $22 \mu m$ resolution. Since the throats are expected to control the permeability, the 35 μm resolution used for modelling the samples might not be sufficient, while the $22 \mu m$ resolution used for the cells is expected to give good results.
Our results include both samples of ca.1.2x1.2x0.9-1.7cm^3 size at $35 \mu m$ resolution and cells of 0.8x0.8x0.4cm^3 size at $22 \mu m$, as well as a few (2a4) at $23.68 \mu m$. For columnar ice the samples fitted well in with the cells (figure 5.14), indicating that a cell size of 0.8x0.8x0.4cm is representative. With characteristic length scales of less than 0.4mm this is plausible. Both non-columnar ice and columnar ice in the horizontal direction perpendicular to the layers show highly scattered permeabilities and zero permeabilities at high porosities, signalling that the cell size might not be representative. In these cases the pores have such large distances or sizes that the permeability is extremely dependent on the exact location of the cell. This could be compensated for by simulating a large number of cells. However, the four cells in each direction we modelled are too few to draw statistically significant conclusions.
That the granular sample 2c1 was not vertically permeable despite its 15% porosity might imply that the sample size of 1.2x1.2x1.7cm is not representative either. It is also possible that this sample has simply been only laterally permeable, that brine was not removed completely during centrifugation or that it had a high tortuosity or tilted channels. In the latter case, the horizontal extent of the sample is important to consider. If the sample is longer than wide, channels that contribute to the ice's real permeability can leave the sample at the sides. Also sample 4c1 is not representative since it contains only one large conducting channel.
Due to the applied periodic boundary conditions only a part of the pore space was modelled - the part where pore on top and bottom of the samples overlap. The overlap fractions (n)

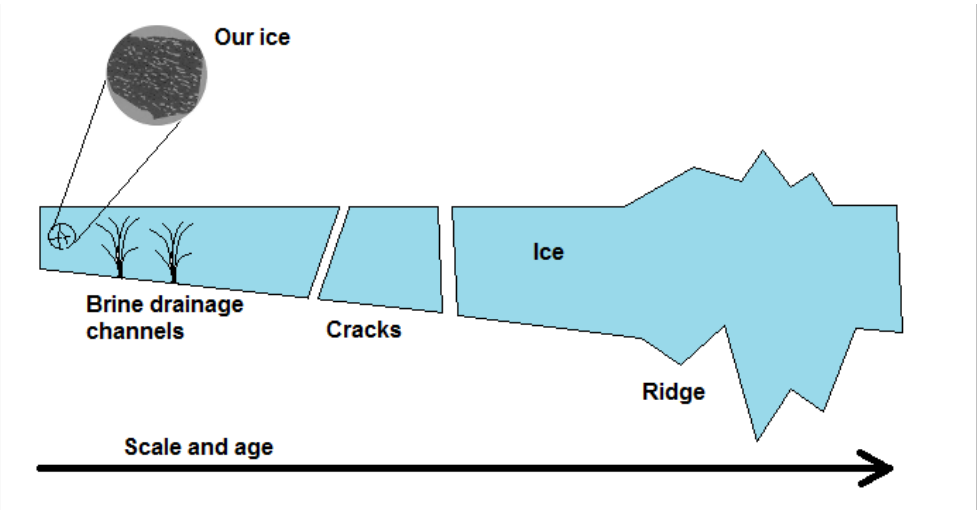

Figure 6.6: Schematic of the size effect

were on average 0.10. Depending on the exact structure, the pore space included correctly in the model might thus be on the order of 10%. The rest of the pore space was included in the model empirically through the correction factor (figure 5.17).

When comparing the LBM permeabilities to other existing data one should keep in mind the possible existence of a scale effect (Freitag, 1999). It is still under debate, but there is strong evidence that for fractured geological media the permeability increases with the scale on which it is measured (Illman, 2006) due to the heterogeneous nature of fractured rocks. On a 10cm scale in older sea ice one expects secondary brine channels, on a 1m scale cracks due to dynamics (figure 6.6). These will have a strong effect on the permeabilities at each of these scales. Cracks often refreeze with thin ice such as ours. Also ridging will create different permeability profiles.

Our measurements of young, fast-growing ice, that has not yet gone through pore size metamorphosis during aging and not developed drainage systems represent the primary microscale permeability in between the major drainage channels (figure 6.6). Most measurements (cells) reflect only single crystals while some (samples) contain parts of several crystal. In more mature ice major drainage channels with distances of up to 5 cm from each other develop (Petrich and Eicken, 2010; Cottier et al., 1999). For this type of ice it is not possible to apply our small scale method before both imaging method and computational power facilitate processing of larger samples at a sufficient resolution. One way our results could possibly be integrated into larger scale models is through the concept of dual porosity (Pringle et al., 2009). This has been used for fractured media, where the medium is described by two separate homogeneous systems - the microscale porosity and the fractures. Each of these systems has a permeability (Gerke and van Genuchten, 1993). Thus it might be possible to combine two imaging techniques at different resolutions to include both micro- and macroporosity. However, the assumption that the micro- and macroporosity are separate is violated in sea ice, where secondary channels evolve fom primary networks and they are coupled with each other. As secondary pores do not always penetrate the whole ice the permeability of the primary networks might be limiting the bulk permeability.

Even though we studied very young ice and much of the Arctic and Antarctic oceans is covered by older and thicker ice, our study is relevant for a very important feature - leads and polynyas. Leads are characterized by open water or thin ice which allows for heat fluxes 1 to 2 orders of magnitude larger than thicker ice (Maykut, 1978). Thus even with areal percentages of leads and polynyas on the order of 1-2% (Smith et al., 1990) their transport properties are of large importance for the heat exchange of the polar oceans.

6.2 Microstructure analysis

Independently of the permeabilities and their additional uncertainties, the porosities, pore size distributions, length scales and tortuosities can be discussed. Uncertainties of the length scales are related to segmentation and sample taking errors as discussed above and considered small. In addition one has to remember that the pores we studied were only centrifuged pore space and air bubbles. Closed pores in the ice appear as salt in the images. The pore sizes and length scales are thus biased.

Porosities

Total porosities are more uncertain than imaged and effective porosities, since they were derived from both images and field data. The field data was taken on a larger scale and the factor in calculating the total porosity from the imaged porosity thus constant for all cells within a sample. One should anticipate uncertainty on the order of $\pm 10\%$ for the total porosities. The total porosity had a C-shaped profile (figure 5.2), as was also found by Maksym and Jeffries (2000). This might be due to a combination of effects - the high porosity at the top is likely due to the high salinity which is either a result of higher growth velocities (Cox and Weeks, 1988) or an indication that the top granular layer is snow ice (Toyota et al., 2007). The high porosity layer at the bottom is due to the higher temperatures. There is a strong discrepancy between the porosities derived from field values for sample 2a4 and from the SXRT images. This is most likely due to brine lost from the bottom of the core during sampling before cutting the core into the samples. This results in a smaller centrifuged brine volume used to calculate the field porosity.
The relationship between effective and total porosity was dependent largely on ice type (figure 5.1). For the columnar samples in yz direction there was agreement with a linear regression. This regression also described the non-zero effective porosities of the columnar samples in x direction well. The effective porosities of non-columnar ice were scattered below this regression line. If the linear behaviour could be extrapolated from our porosity range, the effective porosity could never be equal to the total porosity and the difference would in fact increase with higher total porosities. This is unphysical, as the effective porosity should approach the total porosity at high porosities. Hence, this relationship should be taken as an estimate in our specific porosity range. In figure 6.7 our data is compared to the relationship proposed by Petrich et al. (2006) from a sandwich model. Their relationship overestimates the effective porosities.

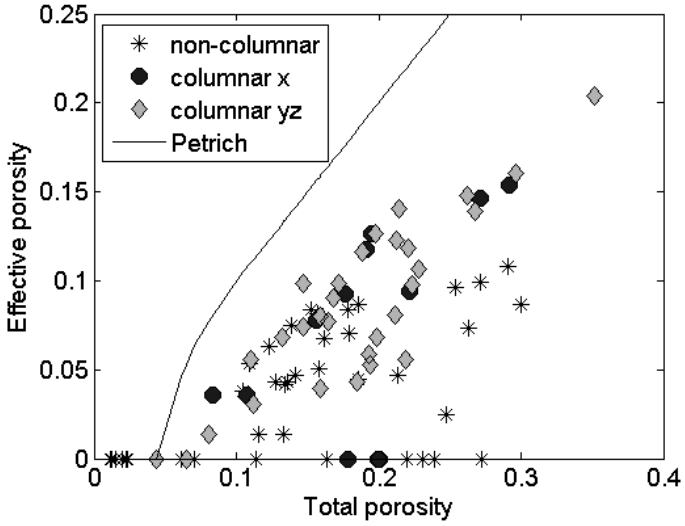

Figure 6.7: Effective and total porosities from our data compared to the relationship proposed by Petrich et al. (2006)

Pore size distributions

The pore radius distributions were generally best fitted by lognormal or gamma distributions (figure 5.3). The distribution statistics varied between the ice types - non-columnar ice had larger means of the logarithm μ and standard deviations of the logarithm σ, and smaller scale parameters α and larger shape parameters θ (table 6.1). Means of the distributions were on the order of 100 μm for columnar ice and 200 μm for non-columnar ice. Pore area distributions generally had a peak at the smallest resolvable area (figure 5.4). Since all pores with a volume of less than 5 voxels were removed prior to analysis and the pore areas were measured in horizontal sections, these pores have to be the ends or constrictions of larger pores. We found that lognormal distributions underestimate the number of small pores in the distribution for columnar samples. Gamma distributions can include this, but overestimate the fraction of medium pore sizes. In fact there was a minimum in the distribution of pore sizes of columnar samples at ca. $0.002 - 0.003 mm^2$. The distribution of pore areas larger than $0.003 mm^2$ was fitted well by a lognormal distribution (figure 6.8). This was also found by Perovich and Gow (1996), who could not resolve smaller pores. Consequently it seems like neither a purely lognormal or gamma distribution fits pore areas well, but a lognormal distribution for pores larger than $3 mm^2$ overlapping with another distribution for the smaller pores could be most suitable for describing columnar ice. The mixed structures of samples 1b1 and 4c1 were similar to the columnar ones in their area distributions while the granular ice of sample 2c1 had two peaks, one centered around $0.001 mm^3$ and one centered around $0.3 mm^2$ separated by a minimum at $0.02 mm^2$. This distribution could be described as two overlapping lognormal distributions.

Table 6.1: Pore radius distribution parameters for the different ice types and mean radii

Ice type	Lognormal μ	Lognormal σ	Lognormal geometric mean $[\mu m]$
columnar	4.6	0.46	99
non-columnar	5.2	0.62	181
Ice type	**Gamma α**	**Gamma θ**	**Gamma mean $[\mu m]$**
columnar	5.3	21	111
non-columnar	2.9	78	226

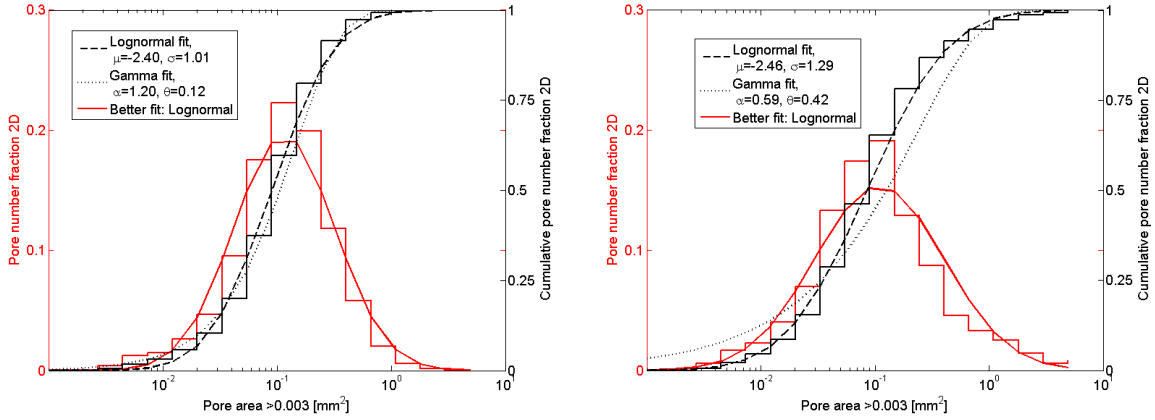

(a) 2a2, pores larger than $0.003mm^2$

(b) 4c1, pores larger than $0.003mm^2$

Figure 6.8: Pore number fractions and cumulative pore number fractions of pore area larger than $0.003mm^2$ with lognormal and gamma distribution fits for 2 examples

Characteristic pore scales

The results of our length scale analysis agree well with previous measurements of pore sizes in columnar and non-columnar young sea ice. Columnar ice had pore scales below $0.4mm$ perpendicular to the columns and up to $1mm$ parallel to the columns. It had a pronounced anisotropy (up to factor 7), while non-columnar ice had rounded pores with little anisotropy (< 2.6) and larger diameters (up to $1mm$).

Columnar ice The length scales that correlated significantly in yz-direction with the porosities were the critical length scale, the minor and the major axis length (table 5.1). Linear regression showed slopes of $0.3mm$, $0.4mm$ and $2.5mm$ for l_c, l_{min} and l_{maj} respectively (figure 5.7). As the ellipse axis lengths were measured in the planes perpendicular to the flow they include both values in x, y and z direction. This may explain the large scatter in the major axis lengths. The increase of major axis lengths with porosity was much stronger than for minor axis lengths, which explains the increase in anisotropy to be discussed below. The difference in growth velocity between major and minor axis lengths might be due to the growth process of columnar ice. Initially the structure is lamellar, i.e. l_{maj} is limited by the crystal size and l_{min} by the distance of the plates. As the ice cools, bridges form between the plates and l_{maj} decreases more than l_{min}.
Both pore radius distribution, the pore volume to surface ratio and the isotropic two-point correlation length were almost constant with little scatter over the whole porosity range with ranges of 0.03 and 0.05 and $0.08mm$. That they were constant while l_{min} and l_{maj} increased is most likely related to that l_{maj} increased much more than l_{min}.
As illustrated in figure 6.9, the same volume increase (i.e. porosity increase) at a higher aspect ratio correponds to less increase in pore volume to surface ratio. If this was the only effect there would still be some increase in ϕ_{im}/s. Either this is not resolved or the surface of the pores was growing more than it would with a perfect ellipse or rectangle. In figure 4.13 correlation between porosity and s/ϕ_{im} was presented for the horizontal section of three samples. For one of the columnar samples (2a3) there was a negative correlation. It seems that this correlation disappeared going from two to three dimensions or from a smaller to a larger scale.
To understand why the median of the pore radius distribution remained constant we need to go back to the algorithm by which it was calculated. The pore radius distribution assigns each point the radius of the largest sphere that fits into the pore and contains the point. Thus the minor axis length of an elliptic pore would be the maximum radius of its pore radius distribution. Its median depends on how much of the pore is smaller than this radius and therefore the major axis length of the pore. If the major axis grows faster than the minor axis, there will be more large R in the distribution, but also more small R such that the median can remain constant. Moreover one should keep in mind that the radius distribution is a threedimensional quantity, while ellipses are fitted in two dimensions. Also different averaging was done for axis lengths and pore radius distributions. In deriving the mean minor axis length we used number averaging, i.e. small pores and large pores were weighted equally. However, large pores tend to have a larger dimension in the vertical as well, and are thus counted in more slices. In deriving the median of the pore radius distribution the radii were weighted by their volume fraction which means by the

radius to the third. For example for two cylindrical channels of equal length with radii 0.1 and $0.3mm$ the mean minor axis length would be 0.2 while the median of the pore radius distribution would be $0.3mm$.
The isotropic two-point correlation length was highly correlated with both pore volume to surface ratio and the median of the pore radius distribution and similarly constant. We attribute this to the same effect as for the median of the pore radius distribution - the elliptic shape and the stronger increase in major axis length. It is remarkable that the isotropic two-point correlation length, which is a quantity measured in two dimensions on only one slice with the same porosity as the whole sample, agrees well with the median of the three-dimensional pore radius distribution and the pore volume to surface ratio.
Furthermore, one should note that the weak increase of l_{min} may be an effect of fitting ellipses to non-elliptic pores.

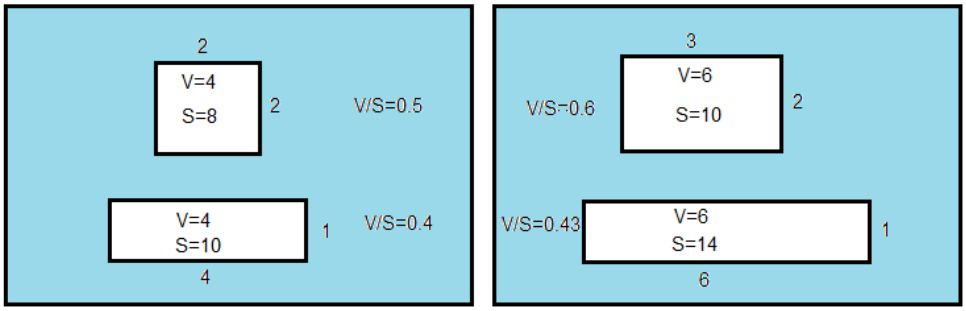

Figure 6.9: Illustration to explain the small change in pore volume to surface ratio (ϕ_{im}/s) in 2D, V referring to Volume (Area) and S to surface (circumference)

Non-columnar ice For non-columnar ice all length scales were significantly correlated with the porosities (table 5.2). For this ice also the median of the pore radius distribution, the isotropic two-point correlation length and pore volume to surface ratio were highly correlated with each other and the minor axis lengths. This is because the pores have smaller aspect ratios and grow in all dimensions more similarly (figure 5.8). The major axis length increased less and the minor axis length more with porosity than for columnar ice.
The critical length scale had a much stronger increase than for columnar ice, but also considerably more scatter. The regression was only done for non-zero l_c which is not meaningful for the non-columnar ice, since it had occurences of zero l_c over the whole porosity range. This means there were large channels in some cells and in others there were none, which is an indication that the cell size was not representative of this ice.
One could say that for non-columnar ice the length scales apart from the critical length scale are more interchangeable than for columnar ice.

Anisotropy and aspect ratios The larger dimension of the pores of columnar ice was captured in the major ellipse axes and the larger of the two-point correlation lengths. The columnar samples had a pronounced anisotropy with length scales in the vertical of 0.6-1.4mm, in the horizontal parallel to the columns 0.2-0.8mm and in the horizontal perpendicular to the columns 0.1-0.3mm. These values are on the same order as and higher than the values by Eicken et al. (2000), which is expected since his maximum temperature of -6°C is below our temperatures. Extrapolating the increase of ellipse axis lengths Eicken et al. (2000) found from -10°C to -6°C to our temperatures of -2°C gives $l_{maj} = 0.97mm$ and $l_{min} = 0.30mm$ in vertical sections and $l_{maj} = 0.42mm$ and $l_{min} = 0.27mm$ in horizontal sections, which is in agreement with our results.
Anisotropy factors of the columnar samples were largest between the vertical and the horizontal perpendicular to the columns and the two horizontal directions, i.e. on average 5 and 3 respectively for the ellipse estimate and 3 and 2 respectively for the two-point correlation estimate (figure 5.10). That the two-point correlation estimate produced smaller values may be because it measured the pore size in the mean direction of the ellipses, while the ellipse estimate measured the pore size for each individual ellipse. Thus if some ellipses were oriented at an angle to the mean direction they contributed less to the pore size estimate. Also the two-point correlation function was only measured in one slice, while the ellipses were found for all slices.
As Eicken et al. (2000) we found a significant increase of anisotropy both between the two horizontal directions and the vertical and the horizontal perpendicular to the layers, yet none within the layers (zy). Therefore we expect anisotropy in the horizontal permeabilities, yet none within the layers of columnar ice.
That the non-columnar ice did not have a macroscopic anisotropy is part of its definition. Aspect ratios were measured from the ellipse fits and were 2.2 on average. This did not vary significantly with porosity. Hence we conclude that the pores were slighly elliptic and grow similarly in all directions. Therefore we do not expect anisotropy in the permeabilities.

Tortuosities

The hydraulic tortuosity was estimated by the ratio of the length of the channel containing the neck l_c and the shortest distance through the sample. There are two cases when this tortuosity is representative of the whole sample - either this channel is the one carrying the major part of the flow, or all other channels have very similar characteristics. In the columnar ice there are usually many similar channels (figure 5.12, samples 2a3 and 2a4), so the latter could be the case. Sample 2a4 is an example of the case where one channel is carrying most of the flow. The hydraulic tortuosities had values below 4 and no significant correlation with the porosities while the electrical tortuosity had values up to 15 and significant correlation with the porosities. Possibly the scatter of the hydraulic tortuosities resulting from estimating the tortuosity from just one channel was too high to resolve any dependency on the porosities. From figure 5.11 it seems unlikely that electrical and hydraulic tortuosity are the same.
The electrical tortuosity was estimated by the method of Katz and Thompson (1987) and depends on l_c and the pore size distribution from the MIP simulation. The range of the values for the formation factor (<3300) agrees with values from Jones et al. (2011) and

Morey et al. (1984). As mentioned do the MIP pore size distribution and l_c only agree well for columnar samples which is why we expect the method to work best for these. Also the anisotropy of the sea ice is reflected in its conductivity and therefore its formation factor. Consequently Archie's law ($F = \phi_t^{-m}$) was fitted to only the columnar samples in yz direction (figure 6.10). The exponent m decreased from 2.6 (figure 5.11) to 2.4. Both values are in the range of reported values (see summary in Ingham et al. (2008)). Since we used l_c to find the formation factor we do not have values for the impermeable samples. Therefore we do not resolve the percolation threshold which has been associated with very large values of the formation factor at small porosities, but are rather in the range of porosities studied by Ingham et al. (2008). They however found a departure from Archie's law at porosities larger than 8-10% which they explained with increased connectivity. We cannot confirm this.

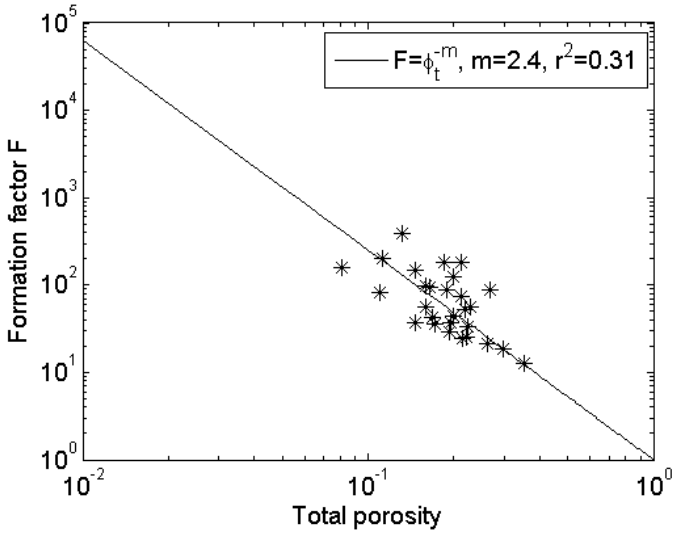

Figure 6.10: Formation factor for the columnar samples in yz direction

6.3 Flow fields

The flow fields in section 5.2 are from the LBM model without a mirrored domain. Thus only pores where the bottom layer is connected to a pore in the top layer show flow. Some of the strong heterogeneity of the flow in e.g. samples 1a3l and 2a2 (figure 5.12) might be attributed to this. Samples 2a3 and 2a4 have a relatively homogeneous flow field with many small pores, and one would not expect it to change considerably with a mirrored domain. The high velocities at the ends of the pores in sample 2a3 and 2a4 are due to pores that only partly overlap in top and bottom layer and thus present constrictions and produce high velocities.

6.4 Permeabilities

The permeabilities of our young sea ice were between 10^{-13} and $10^{-9}m^2$, which agrees well with the order of the values from literature (table 2.1) and corresponds to mostly medium permeable ice.

Columnar ice

The fact that the permeabilities in y and z direction, i.e. within the brine layers did not have significantly different means from each other, indicates that this ice had not yet developed secondary drainage structures. Otherwise the vertical permeabilities would have been larger than the horizontal ones. The permeabilities in y and z direction were best predicted by the effective porosity with $r^2 = 0.68$ for $k = 1.4\ 10^{-9}\phi_{eff}^{1.8}m^2$. Contrary to Freitag (1999)s findings there was a strong relationship with the total porosity as well $k = 1.2\ 10^{-9}\phi_t^{2.6}m^2$ with $r^2 = 0.47$. Even though there were significant correlations with the critical length scale l_c and the mean minor axis length l_{min}, including them into the model with the physically predetermined exponent of 2 did not improve the explained variance or reduce the scatter considerably (table 5.5, figure 5.23).
The fact that the permeabilities did not show any significant correlation with pore size characteristics such as the median of the pore radius distributions or the pore volume to surface ratio, but correlated with l_c and l_{min} reflects that the permeability is affected strongly by the size of the pore necks, the restrictions of the flow and the short dimension of the pores, controlling the friction. As discussed in section 6.2 the columnar cells and samples all had very similar pore size distributions and pore volume to surface area ratios. It is therefore possible to conclude no significant dependency on the major axis length, while no conclusion can be reached for the pore size distribution or pore volume to surface area. Since these two quantities differ strongly between non-columnar and columnar ice, there might be a dependency we cannot uncover when only analyzing columnar samples. As an example, figure 6.11 shows the pore size distributions of two cells that have equal effective porosities, yet their permeabilities differ by the factor 100 (table 6.2). For these two cells both ϕ_{im}/s and med(R) differ much more than they do within the group of columnar samples, but so do l_c and l_{min}. Lacking reliable data for the non-columnar samples we can not statistically prove that the existence of more large pores increases the permeability, which is what Freitag (1999) found. Our analysis shows that a well developed relatively high porosity columnar structure produces high permeability values without any large pores ($R > 0.5mm$) present.

The percolation fit in figure 5.25 should be considered with care, since the equation is only expected to be suitable in the range right above the critical porosity. We had little data around the expected percolation threshold (5-10%) and thus applied it on the whole porosity range. It is questionable whether our method is even applicable around this threshold, since centrifuging will become more ineffective the closer to the critical porosity one gets. The two estimates for the critical porosity of the columnar ice were between 7 and 11% from the percolation fit and 5% (95% CI 0 to 12%) from effective vs total porosities (figure 5.1). This is in agreement with the values of 4.6% and 9% Pringle et al. (2009) found in the vertical and parallel to the layers. The critical exponent of 1.5 ± 0.8 is not significantly different from a previous estimate by Golden et al. (2007) (≈ 2).

Table 6.2: Comparison of a columnar and a granular cell with the same effective porosity

Cell	2a2-y-12	2c1-y-22
Texture	columnar	granular
k $[m^2]$	$4e-12$	$4e-10$
ϕ_{eff}	0.05	0.05
l_c $[\mu m]$	132	632
l_{min} $[\mu m]$	213	310
$\phi_{im}/s[\mu m]$	76	163
Median(R) $[\mu m]$	116	303

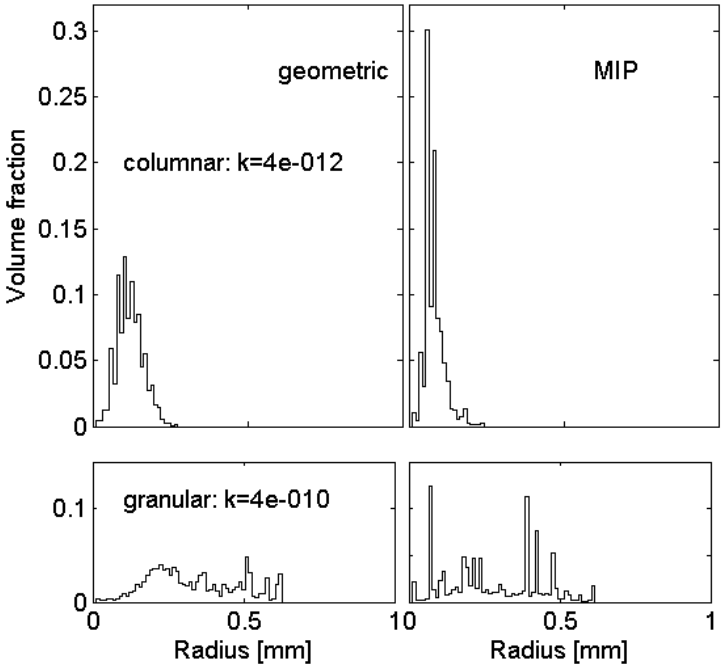

Figure 6.11: The two samples from table 6.2 with equal effective porosities (5%) yet different permeabilities and their pore size distributions, both geometric and MIP

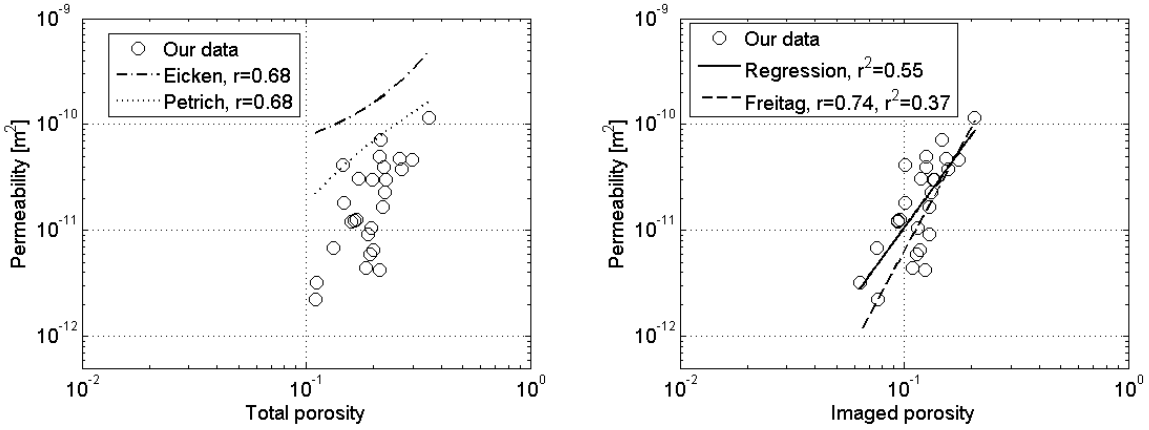

(a) Eicken+Petrich (b) Freitag

Figure 6.12: Permeabilities from the empirical models from (a) Eicken et al. (2004) (eq.2.4) and Petrich et al. (2006) (2.15), (b) Freitag (1999) (eq.2.3) against our permeabilities in yz-direction and a linear regression (figure 5.22); includes logarithmic correlation coefficient r and logarithmic explained variance r^2 for $r^2 > 0$

Of the four permeability models the Kozeny equation (eq. 2.10) and the Kozeny-Carman equation (eq. 2.11) gave the best fits with factors a of 0.04 and 0.07 below the often used empirical values of 0.2 in the Kozeny equation and 0.2 to 0.5 in the Kozeny-Carman relation (table 5.5). These fits still have explained variances much below the ones not including the tortuosities. This might be because of the shape of the pore size distributions, the anisotropy and the uncertainty of the tortuosities. All of these models overestimate the permeabilities at low porosities (figure 5.24). This might be interpreted either as a sign of a percolation effect which is not incorporated in these models or insufficient correction of the LBM permeabilities. Models with the length scale l_c include the percolation effect as l_c becomes zero at the percolation threshold, which may explain why the Katz and Thompson model overestimates small permeabilities slightly less. However the scatter for this model is so large that this is speculation.
The proposed empirical relationships by Eicken et al. (2004) (eq. 2.4) and Petrich et al. (2006) (eq. 2.15) overestimate the permeabilities while Freitag (1999)'s equation for young ice (eq. 2.3) fits well with our data (figure 6.12). His exponent of 3.9 is within the 95% CI interval of our linear regression (figure 5.22 and table 5.5). The former two empirical relationships overestimate especially the lower permeabilities considerably (factor 100). Both are based on data of considerably thicker and older ice, which has had more time to develop secondary drainage structures, while the ice from Freitags ice tank was maximum 19cm thick. It is plausible that the vertical permeability which these equations describe becomes higher when secondary drainage structures develop. Also note that Petrichs relation is not based on permeability measurements but on desalination rates and a simplified microstructure model.

Non-columnar ice

As discussed earlier the results for the non-columnar samples are not as reliable since the sample size was likely not representative of the ice. Also we modelled too few samples for statistical analysis and the three non-columnar samples were very different from each other. From our results we cannot draw conclusions about the dependency of the permeability of non-columnar ice on porosity and other microstructural quantities. We do not anticipate l_{min} to play a role as important as for columnar ice, since in non-columnar ice l_{min} was much more similar to all the other length scales. The critical length scale is expected to be as crucial for the permeability of non-columnar ice as for columnar ice.

Profiles

The permeability profiles in figure 5.27 revealed increasing permeability with depth below the top sample. The top sample 2c1 was granular and its permeability value thus to be considered uncertain because of size effects. The existing values for 2c1 that are very low in the vertical and higher in the two horizontal directions likely present us with the range that the real permeability falls in, because the values correspond to cells that do or do not contain large pores. Unfortunately, this range covers all other permeability values in the profile, such that we can conclude that determining the permeability of granular ice is critical to finding the permeability of the whole ice. The other three samples show a correlation of effective porosity (figure 5.2) with permeability, both increasing with depth. Most critical for the processes mentioned in the introduction is the vertical permeability minimum, and in our young ice it was located at the top of the ice. During spring time and melting from the top this may be different.

7 Conclusions

One of the objectives of this work was to evaluate the method used to find the permeability of sea ice, i.e. the combination of centrifuging, SXRT imaging and LBM modelling.
The advantages of this method over commonly applied methods (e.g., bail test, permeameter) are:

- exact, 3D representation of the pore space allowing for the derivation of many other quantities,
- 3D permeability tensor,
- flow field,
- high resolution.

Limitations of our method are related to:

- complex sample preparation,
- high computational requirements,
- limited sample size,
- problems close to the critical porosity.

Recommendations for the future application and refinement of this method are i) to compare results yielded by bail test measurements and by the method described in this study using the same samples, ii) to further investigate the optimal time of sample centrifugation and iii) to mirror the model domain before applying periodic boundary conditions in the LBM or use other boundary conditions established for low porosity media. Furthermore, we compared three different segmentation methods and suggest using global thresholding in three dimensions with Otsu's algorithm (Otsu, 1979) if the data quality allows for it.
We studied young growing ice of 14cm thickness, in which secondary brine drainage structures had not yet developed. The size of the samples (ca.1.2x1.2x0.9-1.7cm^3) and cells (ca.0.8x0.8x0.4cm^3) was not large enough to yield representative permeability values for non-columnar ice, but produced reliable results for columnar ice. Permeability values should be considered order of magnitude estimates, because of uncertainties connected to the applied periodic boundary conditions. In columnar ice, an anisotropy value of 0.21 (ratio between geometric means, 95% CI: 0.09 to 0.53) was found between horizontal flow perpendicular to the layers and vertical flow, yet none between horizontal flow parallel to the layers and vertical flow, i.e. within the brine layers. This data can be used to improve the correction factor for lateral permeabilities in the bail test (Freitag, 1999). Permeabilities in columnar ice were increasing with depth in the ice.
The following conclusions were drawn about the permeability within the brine layers of columnar ice:

- In the form $k = a\phi^e$ the effective porosity is the best predictor of permeability ($e = 1.8$, $r^2 \approx 0.7$), but total porosity also gives good estimates ($e = 2.6$, $r^2 \approx 0.5$).

- Our data agree well with the empirical relation for young ice by Freitag (1999). His exponent of 3.9 is within our 95% CI of 2.9 ± 1.1.
- The best length scales for predicting permeability are the critical length scale l_c and the minor axis length l_{min}, reflecting the dependence of permeability on pore neck sizes and the smallest dimension of the pores.
- The capillary models and the Katz-Thompson model do not describe adequately columnar sea ice permeability, possibly because of its anisotropy or our tortuosity uncertainties.
- Our estimates of the critical porosity and exponent for percolation are 7 to 11% and 1.5 ± 0.8, respectively.

Other conclusions related to porosities, pore size distributions, length scales and tortuosities are:

- The relationship between effective and total porosities described by Petrich et al. (2006) overestimates the effective porosities of both columnar and non-columnar ice.
- For non-columnar ice, all considered length scales increase with porosity, while for columnar ice only the critical length scale and minor and major axis lengths increase with porosity. In contrast, pore volume to surface ratio, median of the pore radius distribution and two-point correlation length of columnar ice remain constant. This is due to the large anisotropy in columnar ice.
- Columnar ice features a pore scale anisotropy of up to a factor of 7 between the vertical axis and the horizontal axis perpendicular to the layers, and it increases with porosity.
- Pore radius distributions are described well by both lognormal and gamma distributions, with the non-columnar samples having a higher mean radius and larger standard deviations.
- Pore area distributions of columnar ice are best described by a lognormal distribution above $0.003 mm^2$ overlapping with another distribution for smaller pores.
- The formation factor is described through Archie's law with an exponent of 2.6 for all samples, and 2.4 for within the brine layers of the columnar samples.

7.1 Future work

Our dataset allows for further analysis beyond the scope of this work. The velocity fields could be studied closer to determine the portion of the effective porosity that carries the major part of the flow (backbone). Diffusive tortuosity could be modelled as an improved measure of tortuosity. The percolation theory Pringle et al. (2009) used for artificial ice could be tested and, if required, adapted to natural ice. Moreover, the probability of convection could be studied through a Rayleigh number. Biogeochemical analysis of the ice

samples was done and could be related to our microstructure analysis.
Since sea ice is usually composed of both granular and columnar layers, granular ice should be studied in the same manner as columnar ice in order to retrieve complete permeability profiles. Although larger samples have to be imaged to achieve this, a coarser resolution may suffice. Increasing computational power will enable the study of larger samples at higher resolutions.
Other ice types, i.e. older ice and especially summer sea ice, need to be studied as well, as the effects of permeability on albedo and heat fluxes are expected to increase with ice temperature.
The integration of our study results into larger scale models requires a yet-to-be developed method of up-scaling, potentially using the appoach of a dual porosity model. In addition, imaging techniques relying on coarser resolution and applicable at larger scales may offer insight into the larger structural features of sea ice.

References

Arns, C. H., Knackstedt, M. A., and Martys, N. S. (2005). Cross-property correlations and permeability estimation in sandstone. *Phys. Rev. E*, 72(4):046304–.

Arns, C. H., Knackstedt, M. A., Pinczewski, W. V., and Martys, N. S. (2004). Virtual permeametry on microtomographic images. *Journal of Petroleum Science and Engineering*, 45(1-2):41–46.

Bear, J. (1988). *Dynamics of fluids in porous media*. Dover.

Berryman, J. and Blair, S. (1986). Use of digital image analysis to estimate fluid permeability of porous materials: Application of two-point correlation functions. *Journal of Applied Physics*, 60:1930–1938.

Berryman, J. and Blair, S. (1987). Kozeny-carman relations and image processing methods for estimating darcy's constant. *Journal of Applied Physics*.

Berryman, J. G. (1985). Measurement of spatial correlation functions using image processing techniques. *J. Appl. Phys.*, 57(7):2374–2384.

Blair, S. C., Berge, P. A., and Berryman, J. G. (1996). Using two-point correlation functions to characterize microgeometry and estimate permeabilities of sandstones and porous glass. *J. Geophys. Res.*, 101:–.

Carman, P. (1956). Flow of gases through porous media.

Carrier, W. D. (2003). Goodbye, hazen; hello, kozeny-carman. *Journal of Geotechnical and Geoenvironmental Engineering*, 129:11.

Cho, H.-K., Bowman, K. P., and North, G. R. (2004). A comparison of gamma and lognormal distributions for characterizing satellite rain rates from the tropical rainfall measuring mission. Anglais.

Clennell, M. B. (1997). Tortuosity: a guide through the maze. *Geological Society, London, Special Publications*, 122(1):299–344.

Cole, D. M., Eicken, H., Frey, K., and Shapiro, L. H. (2004). Observations of banding in first-year arctic sea ice. *J. Geophys. Res.*, 109(C8):C08012–.

Coleou, C., Xu, K., Lesaffre, B., and Brzoska, J.-B. (1999). Capillary rise in snow. *Hydrol. Process.*, 13(12-13):1721–1732.

Cornell, D. and Katz, D. L. (1953). Flow of gases through consolidated porous media. *Industrial & Engineering Chemistry*, 45(10):2145–2152.

Cota, G. F., Prinsenberg, S. J., Bennett, E. B., Loder, J. W., Lewis, M. R., Anning, J. L., Watson, N. H. F., and Harris, L. R. (1987). Nutrient fluxes during extended blooms of arctic ice algae. *J. Geophys. Res.*, 92:–.

Cottier, F., Eicken, H., and Wadhams, P. (1999). Linkages between salinity and brine channel distribution in young sea ice. *J. Geophys. Res.*, 104.

Courville, Z., Hörhold, M., Hopkins, M., and Albert, M. (2010). Lattice-boltzmann modeling of the air permeability of polar firn. *J. Geophys. Res.*, 115(F4):F04032–.

Covey, C., Taylor, K. E., and Dickinson, R. E. (1991). Upper limit for sea ice albedo feedback contribution to global warming. *J. Geophys. Res.*, 96:–.

Cox and Weeks (1975). Brine drainage and initial salt entrapment in sodium chloride ice. Technical report, Cold Regions Research and Engineering Lab Hanover, N.H.

Cox and Weeks (1983). Equations for determining the gas and brine volumes in sea-ice samples. *Journal of Glaciology*, 29:306–316.

Cox, G. F. N. and Weeks, W. F. (1988). Numerical simulations of the profile properties of undeformed first-year sea ice during the growth season. *J. Geophys. Res.*, 93(C10):12449–12460.

Darcy, H. (1856). *Les Fontaines Publiques de la Ville de Dijon.* Dalmont, Paris.

Duchon, C. E. (1979). Lanczos filtering in one and two dimensions. *Journal of Applied Meteorology*, 18(8):1016–1022.

Edelstein, W. and Schulson, E. (1991). Nmr imaging of salt-water ice. *Journal of Glaciology*, 37:177–180.

Eicken, H., Bock, C., Wittig, R., Miller, H., and Poertner, H. O. (2000). Magnetic resonance imaging of sea-ice pore fluids: methods and thermal evolution of pore microstructure. *Cold Regions Science and Technology*, 31(3):207–225.

Eicken, H., Grenfell, T. C., Perovich, D. K., Richter-Menge, J. A., and Frey, K. (2004). Hydraulic controls of summer arctic pack ice albedo. *J. Geophys. Res.*, 109:–.

Elliot, T. and Heck, R. (2007). A comparison of 2d vs. 3d thresholding of x-ray ct imagery. *Canadian Journal of Soil Science*, 87:405–412.

Emery, W. J. and Thomson, R. E. (2004). *Data Analysis Methods in Physical Oceanography.* Elsevier.

Fredrich, J. T., DiGiovanni, A. A., and Noble, D. R. (2006). Predicting macroscopic transport properties using microscopic image data. *J. Geophys. Res.*, 111:–.

Freitag and Eicken (2003). Melt water circulation and permeability of arctic summer sea ice derived from hydrological field experiments. *Journal of Glaciology*, 49(166):349–358.

Freitag, J. (1999). Untersuchungen zur hydrologie des arktischen meereises : Konsequenzen für den kleinskaligen stofftransport = the hydraulic properties of arctic sea-ice : implications for the small scale particle transport. *Berichte zur Polarforschung = Reports on polar research*, 325:150.

Freitag, J., Dobrindt, U., and Kipfstuhl, J. (2002). A new method for predicting transport properties of polar firn with respect to gases on the pore-space scale. *Annals of Glaciology*, 35.

Fritsen, C. H., Lytle, V. I., Ackley, S. F., and Sullivan, C. W. (1994). Autumn bloom of antarctic pack-ice algae. *Science*, 266(5186):782–784.

Geldsetzer, T., Langlois, A., and Yackel, J. (2009). Dielectric properties of brine-wetted snow on first-year sea ice. *Cold Regions Science and Technology*, 58(1-2):47–56.

Gerke, H. H. and van Genuchten, M. T. (1993). A dual-porosity model for simulating the preferential movement of water and solutes in structured porous media. *Water Resources Research*, 29.

Golden, K. M., Ackley, S. F., and Lytle, V. I. (1998). The percolation phase transition in sea ice. *Science*, 282(5397):2238–2241.

Golden, K. M., Eicken, H., Heaton, A. L., Miner, J., Pringle, D. J., and Zhu, J. (2007). Thermal evolution of permeability and microstructure in sea ice. *Geophys. Res. Lett.*, 34:–.

Hilpert, M. and Miller, C. T. (2001). Pore-morphology-based simulation of drainage in totally wetting porous media. *Advances in Water Resources*, 24(3-4):243–255.

Iassonov, P., Gebrenegus, T., and Tuller, M. (2009). Segmentation of x-ray computed tomography images of porous materials: A crucial step for characterization and quantitative analysis of pore structures. *Water Resour. Res.*, 45:–.

Iassonov, P. and Tuller, M. (2009). Application of segmentation for correction of intensity bias in x-ray ct images. *Vadose Zone J.*, 9:187–191.

Illman, W. A. (2006). Strong field evidence of directional permeability scale effect in fractured rock. *Journal of Hydrology*, 319(1-4):227–236.

Ingham, M., Pringle, D., and Eicken, H. (2008). Cross-borehole resistivity tomography of sea ice. *Cold Regions Science and Technology*, 52(3):263–277.

ITWM, F. (2009). Geodict2010. www.geodict.com.

Johnston, P. R. (1998). Revisiting the most probable pore-size distribution in filter media: The gamma distribution. *Filtration & Separation*, 35(3):287–292.

Jones, K., Ingham, M., Pringle, D., and Eicken, H. (2011). Cross-borehole resistivity tomography of arctic and antarctic sea ice:. *Annals of Glaciology*, 52.

Katz, A. J. and Thompson, A. H. (1986). Quantitative prediction of permeability in porous rock. *Phys. Rev. B*, 34(11):8179–.

Katz, A. J. and Thompson, A. H. (1987). Prediction of rock electrical conductivity from mercury injection measurements. *J. Geophys. Res.*, 92(B1):599–607.

Kawamura, Ishikawa, Takatsuka, Kojima, and Shirasawa (2006). Measurements of permeability of sea ice. *Proceedings oh the 18th IAHR International Symposium on Ice.*

Kawamura, T. (1988). Observations of the internal structure of sea ice by x ray computed tomography. *J. Geophys. Res.*, 93:–.

Kersten, M., Enzmann, F., Huthwelker, T., and Miedaner, M. (2006). Activity report 2006 - tomographic characterization of ice particles. Technical report, International Foundation High Altitude Research Stations Jungfraujoch + Gornergrat.

Lange, M., Schlosser, P., Ackley, S., Wadhams, P., and Dieckmann, G. (1990). 18o concentrations in sea ice of the weddell sea, antarctica. *Journal of Glaciology*, 36:315–323(9).

Le Doussal, P. (1989). Permeability versus conductivity for porous media with wide distribution of pore sizes. *Phys. Rev. B*, 39(7):4816–.

Li, L. W., Kooi, P. S., Leong, M. S., and Yeo, T. S. (1994). A gamma distribution of raindrop sizes and its application to singapore's tropical environment. *Microwave and Optical Technology Letters*, 7(5):253–257.

Light, B., Maykut, G. A., and Grenfell, T. C. (2003). Effects of temperature on the microstructure of first-year arctic sea ice. *J. Geophys. Res.*, 108(C2):3051–.

Lilliefors, H. W. (1967). On the kolmogorov-smirnov test for normality with mean and variance unknown. *Journal of the American Statistical Association*, 62(318):399–402.

Lytle, V. I. and Ackley, S. F. (1996). Heat flux through sea ice in the western weddell sea: Convective and conductive transfer processes. *J. Geophys. Res.*, 101:–.

Maksym, T. and Jeffries, M. O. (2000). A one-dimensional percolation model of flooding and snow ice formation on antarctic sea ice. *J. Geophys. Res.*, 105:–.

Manwart, C., Aaltosalmi, U., Koponen, A., Hilfer, R., and Timonen, J. (2002). Lattice-boltzmann and finite-difference simulations for the permeability for three-dimensional porous media. *Phys. Rev. E*, 66(1):016702–.

Maus, S. (2007). *On Brine Entrapment in Sea Ice: Morphological Stability, Microstructure and Convection.* Logos.

Maus, S., Müller, S., Büttner, J., Brütsch, S., Huthwelker, T., Schwikowski, M., Enzmann, F., and Vähätalo, A. (2011). Ion fractionationg in young sea ice from kongsfjorden, svalbard. *accepted for publication in Annals of Glaciology.*

Maykut, G. A. (1978). Energy exchange over young sea ice in the central arctic. *J. Geophys. Res.*, 83(C7):3646–3658.

Morey, R., Kovacs, A., and Cox, G. (1984). Electromagnetic properties of sea ice. *Cold Regions Science and Technology*, 9(1):53–75.

Moro, F. and Böhni, H. (2002). Ink-bottle effect in mercury intrusion porosimetry of cement-based materials. *Journal of Colloid and Interface Science*, 246(1):135–149.

Nakamura, T., Abe, O., Hasegawa, T., Tamura, R., and Ohta, T. (2001). Spectral reflectance of snow with a known grain-size distribution in successive metamorphism. *Cold Regions Science and Technology*, 32(1):13–26.

Nakawo, M. (1983). Measurements on air porosity of sea ice. *Annals of Glaciology*, 4:204–208.

Notz, D. and Worster, M. G. (2008). In situ measurements of the evolution of young sea ice. *J. Geophys. Res.*, 113(C3):C03001–.

Okada, Kang, and Okiyama (1999). Permeability of an aqueous solution in a state of partial solidification.

Okawa, Saito, Eiriksson, Maeda, Hozumi, and Kumano (2003). Study on permeability of ice/water mixtures. *Trans. of the JSRAE*, 20:287–296.

Ono, N. and Kasai, T. (1985). Surface layer salinity of young sea ice. *Annals of Glaciology*, 6.

Otsu, N. (1979). A threshold selection method from gray-level histograms. *IEEE Trans. Sys., Man., Cyber.*, 9:62–66.

Paterson, M. (1983). The equivalent channel model for permeability and resistivity in fluid-saturated rock - a re-appraisal. *Mechanics of Materials*, 2:345–352.

Perovich, D. K. and Gow, A. J. (1996). A quantitative description of sea ice inclusions. *J. Geophys. Res.*, 101:–.

Petrich, C. and Eicken, H. (2010). *Growth, Structure and Properties of Sea Ice, Chapter 2 in Sea Ice*. Wiley-Blackwell.

Petrich, C., Langhorne, P. J., and Sun, Z. F. (2006). Modelling the interrelationships between permeability, effective porosity and total porosity in sea ice. *Cold Regions Science and Technology*, 44(2):131 – 144.

Premnath, K. N. and Abraham, J. (2007). Three-dimensional multi-relaxation time (mrt) lattice-boltzmann models for multiphase flow. *Journal of Computational Physics*, 224(2):539–559.

Pringle, D. J., Eicken, H., Trodahl, H. J., and Backstrom, L. G. E. (2007). Thermal conductivity of landfast antarctic and arctic sea ice. *J. Geophys. Res.*, 112(C4):C04017–.

Pringle, D. J., Miner, J. E., Eicken, H., and Golden, K. M. (2009). Pore space percolation in sea ice single crystals. *J. Geophys. Res.*, 114(C12):C12017–.

Reynolds, O. (1883). An experimental investigation of the circumstances which determine whether the motion of water shall be direct or sinuous, and of the law of resistance in parallel channels. *Philosophical Transactions of the Royal Society of London*, 174:935–982.

Saeki, H., Takeuchi, T., Sakai, M., and Suenaga, E. (1986). Experimental study on permeability coefficient of sea ice. In *Ice Technology*.

Sahimi, M. (1993). Flow phenomena in rocks: from continuum models to fractals, percolation, cellular automata, and simulated annealing. *Rev. Mod. Phys.*, 65(4):1393–.

Saito, T. and Ono, N. (1978). Measurements of kerosene permeability of nacl ice. *Low Temperature Science*, A37.

Schwartz, L. M., Martys, N., Bentz, D. P., Garboczi, E. J., and Torquato, S. (1993). Cross-property relations and permeability estimation in model porous media. *Phys. Rev. E*, 48(6):4584–.

Semiletov, I., Makshtas, A., Akasofu, S.-I., and L Andreas, E. (2004). Atmospheric co2 balance: The role of arctic sea ice. *Geophys. Res. Lett.*, 31:–.

Sezgin, M. and Sankur, B. (2004). Survey over image thresholding techniques and quantitative performance evaluation. *J. Electron. Imaging*, 13(1):146–168.

Smith, S. D., Muench, R. D., and Pease, C. H. (1990). Polynyas and leads: An overview of physical processes and environment. *J. Geophys. Res.*, 95(C6):9461–9479.

Sukop, M. and Thorne, D. (2007). *Lattice Boltzmann Modeling. An introduction for Geoscientists and Engineers*. Springer.

Thomas and Dieckmann, editors (2010). *Sea Ice: An Introduction to its Physics, Chemistry, Biology and Geology*. Blackwell Publishing, 2 edition.

Torquato, S. (2002). *Random Heterogeneous Materials - Microstructure and Macroscopic Properties*. Springer.

Toyota, T., Takatsuji, S., Tateyama, K., Naoki, K., and Ohshima, K. (2007). Properties of sea ice and overlying snow in the southern sea of okhotsk. *Journal of Oceanography*, 63(3):393–411.

Weeks, W. F. and Ackley, S. F. (1986). Chapter 1, the growth, structure, and properties of sea ice. *The Geophysics of Sea Ice*, pages 9–153.

Weissenberger, Dieckmann, Gradinger, and Spindler (1992). Sea ice: A cast technique to examine and analyze brine pockets and channel structure. *Limnol. Oceanogr.*, 37:179–183.

Weissenberger, J. (1992). Die lebensbedingungen in den solekanälchen des antarktischen meereises. *Berichte zur Polarforschung*, 111.

Wiegmann, A. and Becker, J. (2007). Virtual characterization of the pore structure of nonwoven. *International Nonwoven Technical Conference, Atlanta*.

Wolf-Gladrow, D. (2005). *Lattice-Gas Cellular Automata and Lattice Boltzmann Models - An Introduction*. Springer.

Yu, D., Mei, R., Luo, L.-S., and Shyy, W. (2003). Viscous flow computations with the method of lattice boltzmann equation. *Progress in Aerospace Sciences*, 39(5):329–367.

Zhang, J. and Kwok, D. Y. (2006). Pressure boundary condition of the lattice boltzmann method for fully developed periodic flows. *Phys. Rev. E*, 73(4):047702–.